Lehrstuhl für Elektrische Antriebssysteme und Leistungselektronik
der Technischen Universität München

Current Distortion Optimization for Electrical Drives at Low Switching Frequencies

Reza Fotouhi

Vollständiger Abdruck der von der Fakultät für Elektrotechnik und Informationstechnik der Technischen Universität München zur Erlangung des akademischen Grades eines

Doktor-Ingenieurs

genehmigten Dissertation.

Vorsitzender:	Univ.-Prof. Dr.-Ing. Thomas Eibert
Prüfer der Dissertation:	1. Univ.-Prof. Dr.-Ing. Ralph Kennel
	2. Univ.-Prof. Dr. Daniel E. Quevedo

Die Dissertation wurde am 21.12.2015 bei der Technischen Universität München eingereicht und durch die Fakultät für Elektrotechnik und Informationstechnik am 29.05.2016 angenommen.

The important thing is not to stop questioning. Curiosity has its own reason for existing.

Albert Einstein

Preface

This dissertation would not have been possible without the help of many people in many ways. It is also the result of fortuitous encounters with people who shaped or, in some cases, changed the course of events in my career. I decided to choose this topic for my PhD thesis while working on another project. I had to calculate optimal pulse patterns for a 2-level converter as a basis for a comparative study with predictive control. A student of mine, Lukas Leitner, did the programming for offline optimization. Everything went smoothly; however, code execution time was about two days. Since then I started doubting the classical approaches as they are too slow.

Some weeks later, I met Dr. Heinle at Siemens Drive Technologies. We discussed the concept behind optimal pulse patterns and specifically the properties of an optimal flux trajectory. In the following weeks, I kept on generating 3D plots of current distortion and looking at stator flux trajectories while changing the switching instances of the pulse train. The observation of the geometry of flux trajectory at different optimal points made very soon clear that the simplifications that are often made to formulate the problem slow down the optimization procedure. This was the starting point; however, it took me about two more years to develop the algorithms, set up a test bench, get the results and write this dissertation.

I want to express my deep gratitude to my supervisor Prof. Dr. Ing. Ralph Kennel for his continued support, valuable advice and for the confidence he placed in me. I got the chance to work on the topic that I liked, had the opportunity to meet many people from academia and industry who are very active in the field of power electronics and electrical drives, had the possibility to present my work on conferences and had the chance to visit Stellenbosch University in South Africa for a few times. None of this would have been possible without your trust in me and I will always be grateful to that.

I would also like to thank Prof. Toit Mouton from Stellenbosch University in South Africa. I benefited from his comments and feedback on my work. Furthermore, I learned many interesting things during my visit to his institute and I truly enjoyed discussing optimal control theory and MPC with him - mainly due to his very unique way of looking at mathematical problems.

For this work, a 5-level flying capacitor converter was designed and built up from scratch. Besides, several simulations and experiments were carried out in order to develop the final control schemes. This would not have been possible in this time frame without the help of my very talented students. I especially want to thank Sören Schreiweis and Markus Sievers for helping to set up the test bench and Lukas Leitner and Alexey Sorokin for their help in

programming and simulation studies.

I am also very grateful to my colleagues at the Institute for Electrical Drive Systems and Power Electronics for their help and support, for all our productive scientific discussions and for all the funny and great moments we had. In particular, I would like to thank two of my colleagues, Darshan Manoharan and Ali El-Hafni, who generously spent time on proofreading this thesis in spite of being very busy with their own projects.

The last word goes out to my parents and to my sister. You have always inspired me to do my best and have supported me in every decision I made. I want to dedicate this work to you for your endless love. Thank you so much.

Munich, December 2015
Reza Fotouhi

Contents

CHAPTER 1

Introduction

People frequently express the view that Power Electronics is already a mature technology, that machines work more or less at their physical limits and hence, no more novelties can be expected. In order to evaluate the latter part of this statement, one has to define the properties of an advanced electrical drive first. Accurate reference tracking and fast dynamics are the main properties. However, robustness, efficiency, optimal performance, system constraints handling and operation in faulty conditions define the performance index of an advanced electrical drive.

Taking a close look at available drives on the market brings us to the conclusion that they have good reference tracking and fast dynamics (very close to their physical limits), that they are robust and that their energy efficiency is acceptable. Conversely, most electrical drives are not operated at their energy optimum operating point. They do not follow optimal time trajectories. Robustness is mainly achieved via observer adaptation and not via improved sensing of physical variables. There is no straightforward approach to dealing with constraints which causes limitations regarding faulty conditions.

These imperfections are neither physical limits nor the consequence of a lack of knowledge in control theory. In fact, these limitations exist mainly due to the insufficiency of calculation power at the time when electrical drives were designed back in the 80s and 90s, whereas today fast processors let us perform complicated tasks such as signal processing and optimal control in real-time.

Signal processing techniques mainly facilitate the observer design by extracting more information from sensed signals. Optimal control techniques enable system operation at an optimal point. Moreover, constraint optimization, which is an inherent feature of Model Predictive Control (MPC), is a classical approach to dealing with constraints without sacrificing on dynamics. The possibility of setting soft and hard constraints on system variables and of having a simultaneous fast dynamic performance eases handling a faulty condition.

There are many publications on the application of these tools to electrical drives; however, most of them only address reference tracking and system dynamics problems. In order to achieve the slightest improvement, one has to not only try out things in new ways, but at the

same time address new issues and strive for secondary goals as well. This approach is opposed to the one described in the beginning: instead of being content with achievements, we should try to improve things even further.

This work addresses an optimization problem for electrical drives. More specifically it confronts the current distortion optimization problem at low switching frequencies. Main requirements of converters - especially at high power levels - are a low harmonic distortion of current in order to decrease load losses and a low switching frequency in order to decrease converter losses and hence, to increase its utilization. These requirements are obviously in contrast, so a trade-off is necessary between minimal switching losses and minimal harmonic distortion of the current. This trade-off is usually made in two ways:

- Keeping the switching frequency constant and optimizing the current distortion,
- Keeping the current distortion or torque ripple below a certain value and minimizing the switching frequency.

The first option can be achieved via Synchronous Optimal Modulation (SOM) or in other words Optimal Pulse Patterns (OPP). In this approach, the concept of clocking the pulses is completely eliminated from the Space Vector Modulation (SVM) scheme and switching events are allowed to take place freely over the fundamental period with the single constraint of maintaining waveform symmetry. Thus the commutation angles can be calculated to achieve the desired modulation index for the output voltage while eliminating certain harmonics from the current or minimizing its distortion [1]. This optimization is a very slow procedure. Depending on the converter topology, switching frequency etc, calculation times range from a couple of days up to even several weeks. As a result, optimal switching instances are calculated offline and stored in memory with the modulation index and pulse number as parameters.

Optimization of the switching frequency by keeping the current distortion under a maximum value is achieved by hysteresis-based model predictive control in which the current is kept within hysteresis boundaries and switching events are minimized over the prediction horizon. Although at low switching frequencies this scheme can have comparable distortion with OPPs, it cannot profit from the benefits of fixed and synchronous modulation. A fixed switching frequency shapes the current spectrum in such a way that harmonics show up on multiples of the switching frequency and its sidebands, while synchronism eliminates the subharmonic components from the generated waveforms. Another issue with hysteresis based MPC is that in order to achieve comparable results with OPP, the current boundary has to be transformed from circular to rectangular in the $\alpha\beta$ plane at high modulation indexes [2].

Some questions might be raised here:

- Is it possible to speed up the offline optimization procedure for pulse pattern generation?
- Is it possible to generate OPPs online?
- Is it possible to design a predictive-based controller that has a comparable distortion with OPPs at low switching frequencies and at the same time has the benefits of fixed and synchronous modulation?

The objective of this thesis is to find answers to these questions. After this introduction, system modeling and basic concepts are explained in the second chapter. Chapter 3 provides a brief introduction and classification of MPC in electrical drives. In chapter 4, optimal pulse patterns are analyzed and a new optimization formulation is introduced, by the use of which calculation time is reduced considerably. OPP investigation results are taken into account to design a predictive-based online current distortion optimizer in chapter 5. Eventually, chapter 6 concludes the work by summarizing the contributions.

CHAPTER 2

System model

The term *model* in model predictive control emphasizes the fact that we deal with a model-based controller; however, it is very difficult to imagine the existence of any high performance controller that does not consider the available information about the behavior of a system. In principle, a system model is necessary to understand a plant, predict its behavior and design a controller for it. A drive system mainly consists of an electrical machine and a converter. Electrical machines are usually considered as continuous state machines. In contrast, the power converter is a Finite State Machine, which means that its output can vary among finite discrete states. As a result, two categories of controllers are plausible for a drive system. In the first category, which is known as direct method, the controller receives continuous feedback from the machine and directly chooses a state among finite converter states. Thus, the controller has a hybrid nature. In the second category, controller receives continuous feedback from the machine and sets the reference output voltage of the converter in continuous mode. In this case, a modulator is needed to translate continuous references into a pulse train that is understandable for the converter. As a result, a modulator is a part of an electrical drive alongside the machine, power converter and controller.

In this chapter and after a short description of the notation and symbols used, the modeling of the electrical drive system is provided.

2.1 Symbols and notations

A list of symbols and abbreviations is given in appendix A. Additionally, symbol fonts, dimensions as well as super- and subscripts that are used in this work as an indication of certain properties of a quantity need to be defined.

Table 2.1 shows how scalars and matrices are defined throughout the thesis. Table 2.2 shows different representations of a signal (eg.: voltage signal, $u\,(t)$).

Table 2.1: Dimensions

Symbol	Character	Definition
R	regular capital	scalar
$\mathbf{A}$	bold capital	matrix

Table 2.2: Representations of an examplar signal

symbol	Character	definition
u	regular small	instantaneous value
$\hat{u}$	small hatted	peak value
u_{rms}	small with rms subscript	effective or rms value
$\mathbf{u}$	small bold	vector
$\lvert\mathbf{u}\rvert$	small bold in vertical bars	absolute value

Subscripts are used to show the physical location, origin or coordinate frame of a quantity. Throughout the thesis, unique symbols are used to define each quantity. However, the subscript s is an exception. It is mainly used to refer to the stator, such as in R_{s}. In case of time, it stands for sampling, as in T_{s}, and in ω_{s}, it refers to synchronous. As these definitions are commonly used throughout the drive community, the notation has not been changed in order to avoid confusion.

The only superscript used is $*$, which denotes the reference value of a signal.

Table 2.3: Subscripts

symbol	definition
r,s	rotor and stator
s	in case of time, sampling, and in ω_{s}, synchronous
a, b, c	three phases
α, β	stator-fixed Cartesian axes
d, q	rotor-fixed Cartesian axes
opt	optimal value
est	estimated value
p	predicted value
ph	prediction horizon
m	mechanical or magnetizing
e	electrical
sw	switching
rec	recovery
FC	flying capacitor
dc	direct current
rms	root mean square

2.2 Induction motor model

In principle, an induction motor IM is an asynchronous motor in which electromagnetic induction from the magnetic field of the stator winding generates electric current in the rotor winding or rotor bars. Thus it does not need any mechanical commutation, separate-excitation or self-excitation for transferring energy from the stator to the rotor. Induction motors are reliable and cost effective due to their simple concept and are widely used in both fixed and variable frequency industrial drives.

2.2.1 Induction machine model

The basic equations of an IM can be written in a coordinate system that rotates with an arbitrary angular velocity ω_k

$$\boldsymbol{u}_\mathbf{s} = R_\mathrm{s}\boldsymbol{i}_\mathbf{s} + \frac{d\boldsymbol{\psi}_\mathbf{s}}{dt} + j\omega_k\boldsymbol{\psi}_\mathbf{s}, \tag{2.1a}$$

$$\boldsymbol{u}_\mathbf{r} = R_\mathrm{r}.\boldsymbol{i}_\mathbf{r} + \frac{d\boldsymbol{\psi}_\mathbf{r}}{dt} + j\left(\omega_k - \omega_\mathrm{e}\right)\boldsymbol{\psi}_\mathbf{s}, \tag{2.1b}$$

$$\boldsymbol{\psi}_\mathbf{s} = L_\mathrm{s}\boldsymbol{i}_\mathbf{s} + L_\mathrm{m}\boldsymbol{i}_\mathbf{r}, \tag{2.1c}$$

$$\boldsymbol{\psi}_\mathbf{r} = L_\mathrm{r}\boldsymbol{i}_\mathbf{r} + L_\mathrm{m}\boldsymbol{i}_\mathbf{s}, \tag{2.1d}$$

$$T = \frac{3}{2}P|\boldsymbol{\psi}_\mathbf{s} \times \boldsymbol{i}_\mathbf{s}| = \frac{3}{2}P\frac{L_\mathrm{m}}{\sigma L_\mathrm{s}L_\mathrm{r}}|\boldsymbol{\psi}_\mathbf{r} \times \boldsymbol{\psi}_\mathbf{s}|. \tag{2.1e}$$

Stator variables are marked in the form $(*)_\mathrm{s}$, while rotor variables are denoted in the way $(*)_\mathrm{r}$. $\boldsymbol{\psi}_\mathrm{s}$ and $\boldsymbol{\psi}_\mathrm{r}$ are the fluxes, $\boldsymbol{i}_\mathrm{s}$ and $\boldsymbol{i}_\mathrm{r}$ the currents, R_s and R_r the resistances, L_s and L_r the inductances and L_m corresponds the mutual inductance between stator and rotor. $\boldsymbol{v}_\mathrm{s}$ is the applied stator voltage and $\boldsymbol{u}_\mathrm{r}$ the rotor voltage ($\boldsymbol{u}_\mathrm{r} = (0\,\mathrm{V}, 0\,\mathrm{V})^T$ for a squirrel-cage induction motor). j is defined as $j = \sqrt{-1}$. ω_e is the electrical angular machine speed, which is given by

$$\omega_\mathrm{e} = P \cdot \omega_\mathrm{m}, \tag{2.2}$$

where P is the number of pole pairs and ω_m the mechanical machine speed.

For $\omega_\mathrm{k} = 0$, the coordinate system is fixed to the stator. So an IM model in the $\alpha\beta$ coordinate system is

$$\boldsymbol{u}_\mathbf{s} = R_\mathrm{s}\boldsymbol{i}_\mathbf{s} + \frac{d\boldsymbol{\psi}_\mathbf{s}}{dt}, \tag{2.3a}$$

$$0 = R_\mathrm{r}\boldsymbol{i}_\mathbf{r} + \frac{d\boldsymbol{\psi}_\mathbf{r}}{dt} + j\omega_\mathrm{e}\boldsymbol{\psi}_\mathbf{s}, \tag{2.3b}$$

$$\boldsymbol{\psi}_\mathbf{s} = L_\mathrm{s}\boldsymbol{i}_\mathbf{s} + L_\mathrm{m}\boldsymbol{i}_\mathbf{r}, \tag{2.3c}$$

$$\boldsymbol{\psi}_\mathbf{r} = L_\mathrm{r}\boldsymbol{i}_\mathbf{r} + L_\mathrm{m}\boldsymbol{i}_\mathbf{s}, \tag{2.3d}$$

$$T = \frac{3}{2}P|\boldsymbol{\psi}_\mathbf{s} \times \boldsymbol{i}_\mathbf{s}| = \frac{3}{2}P\frac{L_\mathrm{m}}{\sigma L_\mathrm{s}L_\mathrm{r}}|\boldsymbol{\psi}_\mathbf{r} \times \boldsymbol{\psi}_\mathbf{s}|. \tag{2.3e}$$

Equation (2.3e) can be written as

$$T = \frac{3}{2} P \frac{L_{\mathrm{m}}}{\sigma L_{\mathrm{s}} L_{\mathrm{r}}} |\boldsymbol{\psi_r}||\boldsymbol{\psi_s}| \sin\delta, \tag{2.4}$$

where δ is the angle between stator and rotor fluxes. Considering the fact that the magnitude of the stator flux is kept constant at its nominal value in the normal operation mode, the torque will mainly depend on the angle between stator and rotor fluxes. The difference between synchronous and mechanical speeds and therefore, the slip also depends on the angle δ. Based on (2.3b) and considering steady-states operation, the following equation is valid

$$\omega_{\mathrm{s}} - \omega_{\mathrm{e}} = \frac{3}{2} P \frac{R_{\mathrm{r}}}{|\boldsymbol{\psi_r}|^2} T = \frac{9}{4} P^2 \frac{L_{\mathrm{m}} R_{\mathrm{r}}}{\sigma L_{\mathrm{s}} L_{\mathrm{r}}} \frac{|\boldsymbol{\psi_s}|}{|\boldsymbol{\psi_r}|} \sin\delta. \tag{2.5}$$

It can be seen that an increase in torque at a constant mechanical speed corresponds to an increase in synchronous speed. Equation (2.5) is used to adjust the prediction horizon in chapter 5.

2.2.2 Induction machine power losses

If a purely sinusoidal voltage is applied to an induction motor, a small portion of the power will be dissipated from the stator terminals to the shaft. Typical losses of an induction motor are stator and rotor copper as well as core losses, friction and windage losses. These losses are shown in Figure 2.1. However, the machine is usually fed via a power converter, which means that the input voltage is a pulse train instead of sinusoidal voltage. As a consequence, there would be extra losses due to harmonic currents. High order harmonic currents are attenuated due to the inductive characteristics of the load. Therefore, increasing the switching frequency that pushes the voltage harmonics to higher orders has the biggest impact on these losses.

In this work, machine losses are chiefly understood as losses originating from a non-sinusoidal current waveform.

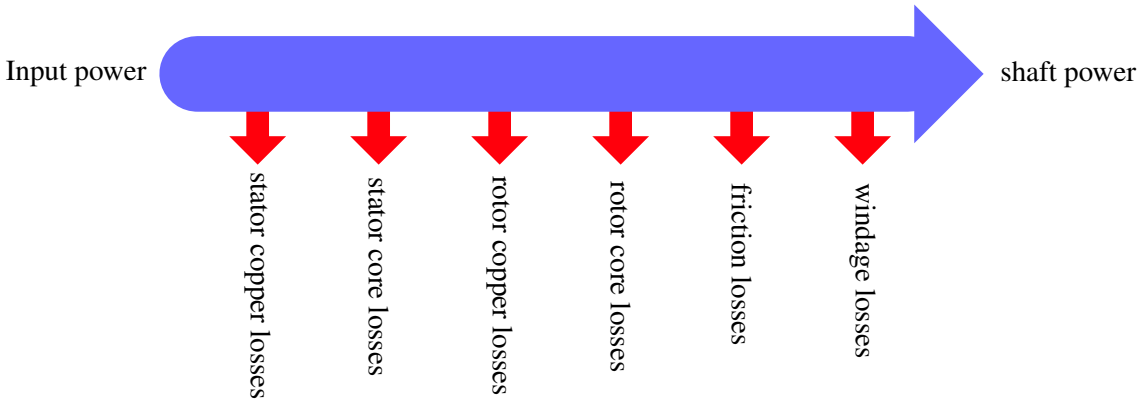

Figure 2.1: Typical power losses of an IM

2.3 Power converters

2.3.1 2-level converter

The primary function of a voltage source inverter (VSI) is to convert a fixed DC voltage to a three-phase ac voltage with variable magnitude and frequency. A simplified circuit diagram of a 2-level voltage source inverter is shown in Figure 2.2. This inverter is composed of 6 power switches (IGBT, IGCT or MOSFET depending on power rating and application) with free-wheeling diodes anti-parallel to each switch. Assuming s_x (with $x = a$, b or c) being 1 represents the on state of the upper switch on each leg and being 0 represents its off state, the phase and line voltages of the converter will be defined as

$$u_a = s_a u_{\mathrm{dc}}, \tag{2.6a}$$
$$u_b = s_b u_{\mathrm{dc}}, \tag{2.6b}$$
$$u_c = s_c u_{\mathrm{dc}}, \tag{2.6c}$$

$$u_{ab} = u_a - u_b = (s_a - s_b)\, u_{\mathrm{dc}}, \tag{2.7a}$$
$$u_{bc} = u_b - u_c = (s_b - s_c)\, u_{\mathrm{dc}}, \tag{2.7b}$$
$$u_{ca} = u_c - u_a = (s_c - s_a)\, u_{\mathrm{dc}}. \tag{2.7c}$$

Phase voltages can be transformed to stator-fixed coordinates via Clarke transformation

$$\begin{bmatrix} u_\alpha \\ u_\beta \end{bmatrix} = \mathbf{P} \begin{bmatrix} u_a \\ u_b \\ u_c \end{bmatrix}, \tag{2.8}$$

where **P** is the Clarke transformation matrix.

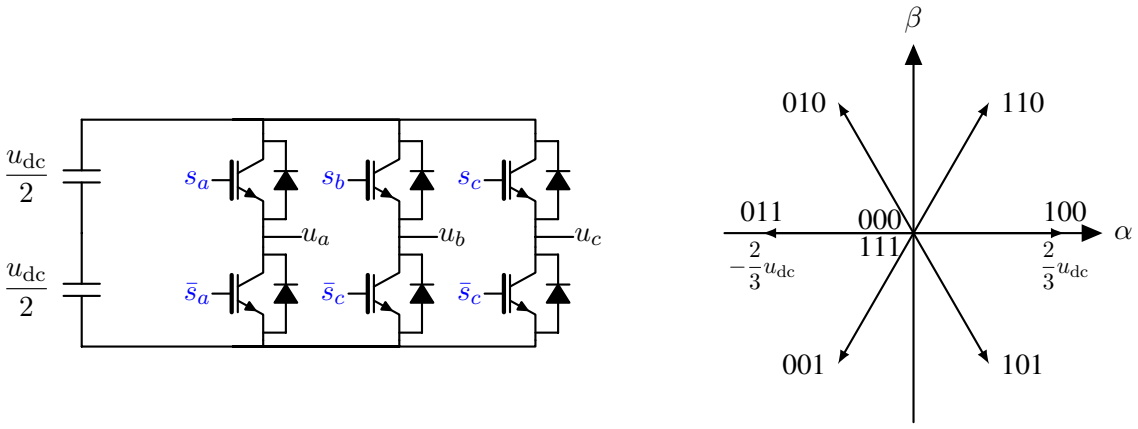

Figure 2.2: 2-Level voltage source converter. Left: circuit diagram, right: voltage vectors

$$\mathbf{P} = \frac{2}{3}\begin{bmatrix} 1 & -\frac{1}{2} & -\frac{1}{2} \\ 0 & \frac{\sqrt{3}}{2} & -\frac{\sqrt{3}}{2} \end{bmatrix} \tag{2.9}$$

The voltage vectors of a typical 2-level converter in the stator-stationary-frame are shown in Figure 2.2.

2.3.2 Multilevel converters

Multilevel Converters (MLCs) consist of an array of semiconductor devices and capacitive voltage sources, which generate output voltage waveforms with multiple steps by appropriate switching. By increasing in the number of voltage levels or steps, the staircase output waveform approaches a sinusoidal waveform [3].

MLCs were first used with the specific aim of overcoming the problems associated with the limited blocking voltage range of semiconductor devices. Nowadays, MLCs are used as an attractive solution for MV highpower applications due to numerous merits over classical 2-level converters such as higher operating voltage capability with low-voltage semiconductor devices, better output voltage waveform quality, lower harmonic distortion of the input and output currents, reduced filter size, less $\mathrm{du/dt}$ stress, lower common-mode voltages, reduced electromagnetic interference, reduced torque ripple, and feasible fault-tolerant operation [3], [4].

There are mainly three types of voltage source MLCs: Neutral Point Diode Clamped (NPC), Flying Capacitor (FC) and series or cascaded Connected H-Bridge (CHB) inverters. In addition to these classical topologies, several hybrid converters are introduced by combining elements of two or three classical multi-level converters. Although tens of different multi-level converters have been reported in literature, taking a look at the available converters on the market for MV drives narrows down the long list to a few: 3L-NPC, 5L-ANPC, 4L-FC and CHB. These converters are shown in Figures 2.3, 2.4, 2.5 and 2.6 respectively. Additionally, a summary of the available MLCs in the market is given in Table 2.4.

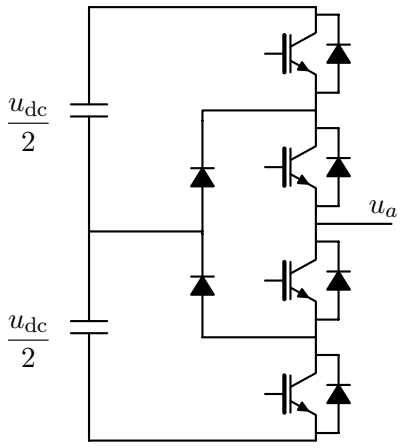

Figure 2.3: 3L-NPC Topology

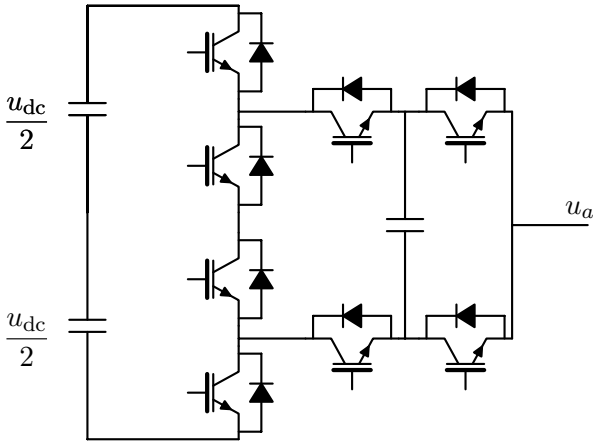

Figure 2.4: 5L-ANPC Topology

The NPC topology was developed in the late 1970s and early 1980s [5]. This converter, also known as Diode-Clamped Converter (DCC), was the first multilevel topology to be utilised in MV applications and is still widely used as an MV converter. Its features include a relatively small DC-link capacitor, a simple power circuit topology, a low component count and straightforward modulation and protection schemes [4].

Although this topology has a simple circuit, it usually needs a large inductive capacitive filter to operate standard MV motors. Besides, its application for voltage levels above three is not efficient mainly due to excessive losses of clamping diodes, uneven distribution of losses in inner and outer devices, and unachievable DC-link capacitor voltage balance [6]. The 5L-ANPC, a hybrid converter consisting of NPC and FC converters, was introduced to overcome the drawbacks of the 5L-NPC [7].

The CHB converter was developed in the late 1960s, making it the oldest multilevel converter topology [8]. As this topology consists of series and/or cascaded-connected power conversion cells, its voltage and power levels can easily be scaled, which makes it an attractive option for HVDC applications. A major drawback of this topology is the large number of required isolated power supplies. However, the cells can be supplied via a phase-shifted transformer in order to provide high power quality at the utility side.

The FC converter, also known as the capacitor-clamped converter, utilizes independent capacitors with distinct voltage levels in order to synthesize multilevel output voltages. The topology was proposed in the early 1970s for low-power applications [9] and has been developed for the use in MV applications only after the 1990s [10]. The main advantages of this converter are symmetrical switching loss distribution, easy capacitor voltage balancing due to more per-phase redundancies and a small inductive-capacitive filter. In a FC converter, the load current flows through the flying capacitors and charges or discharges them. The resulting changes in the capacitor voltages must remain in a permissible range. Thus, the required capacitance increases approximately in inverse proportion to the switching frequency. Therefore, the main disadvantage of an FC converter is either the bulky capacitors or the extra switchings that are being initiated from capacitor voltage balancing.

The focus of this work is current distortion optimization. Any of these multilevel converters could have been used to implement the final control algorithm. However, the 5L-FC is finally

Table 2.4: Availabe multi-level converters on the market

Supplier	**Model**	**Power (MW)**	**Voltage (KV)**	**Topology**	**Semiconductor**
Siemens	Sinamics GH150/180	6.7-14.2	1.3-11	SCHB	LV-IGBT
	Sinamics GM150	0.8-27	2.3-4.16	3L-NPC	HV-IGBT/IGCT
	Sinamics SM150	5-30	2.3-4.16	3L-NPC	IGCT
ABB	ACS1000	0.2-5	2.3-4.16	3L-NPC	IGCT
	ACS2000	0.25-36	4-6.9	5L-ANPC	IGBT
	ACS5000	3-36	6-13.8	NPC-HB Hybrid	IGCT
	ACS6000	3-36	2.3-3.3	3L-NPC	IGCT
GE	MV4	0.25-4	2.4-4.16	SCHB	IGCT
	MV6	0.5-6	6-6.9	SCHB	IGBT
	MV7000	3-81	3.3-10	3L-NPC	IGBT

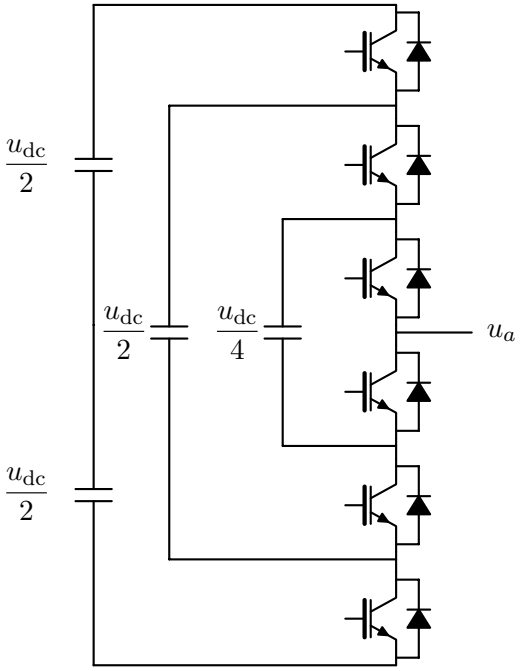

Figure 2.5: 4-level flying capacitor converter

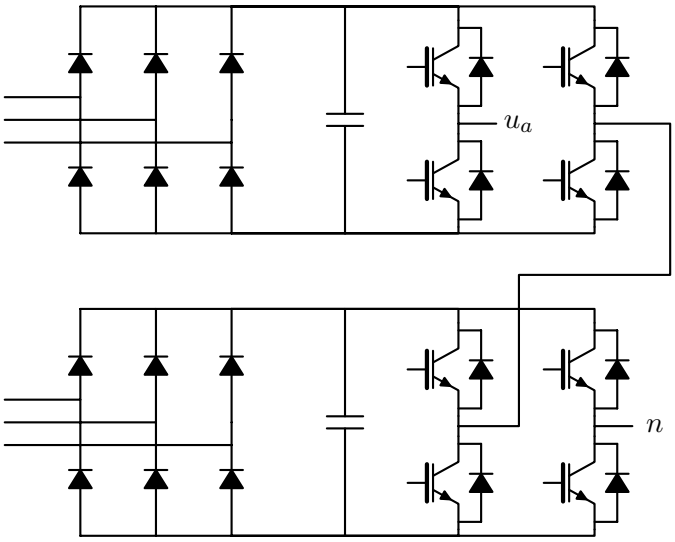

Figure 2.6: Two series connected H-bridges

chosen to be constructed and used. Thus, this converter is explained more extensively in the following.

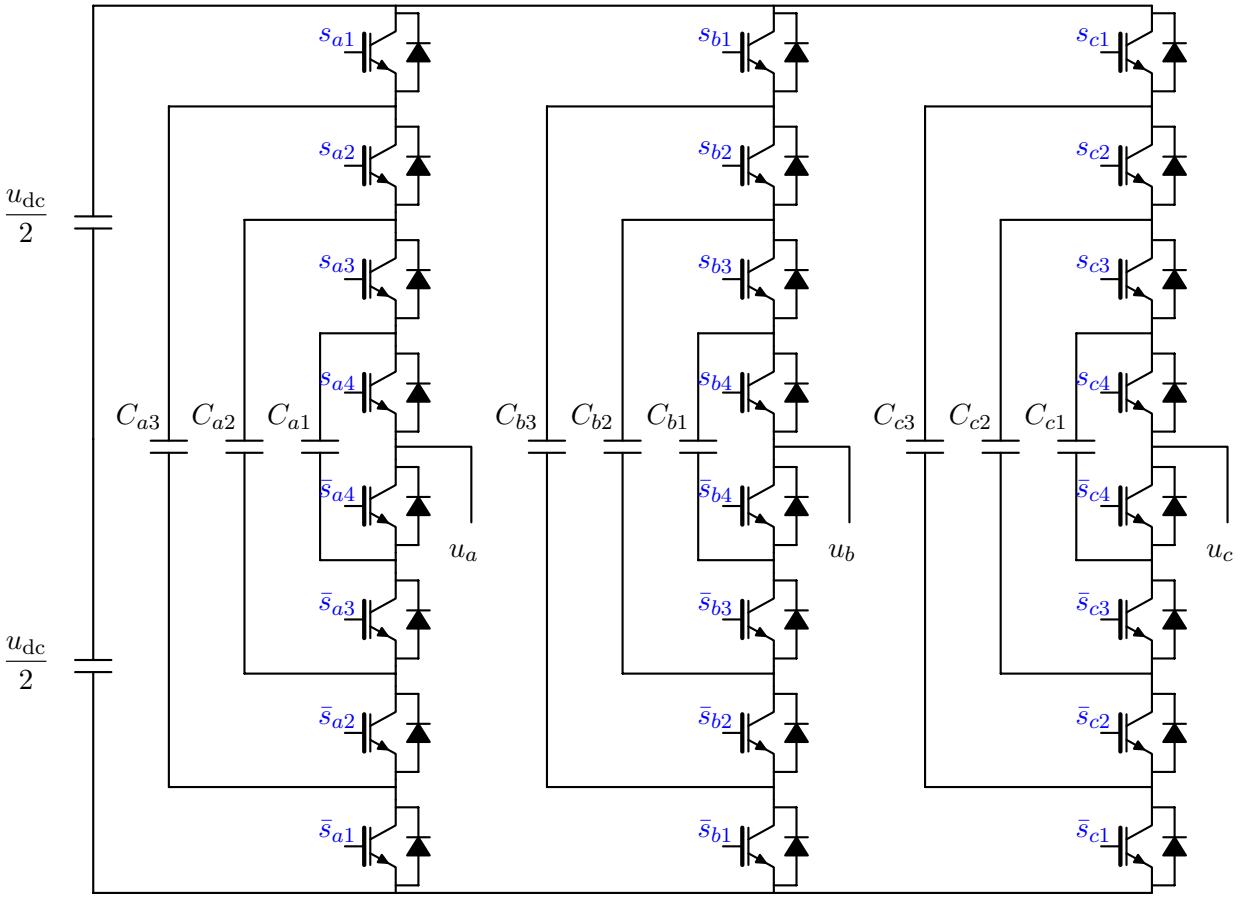

(a) Circuit diagram

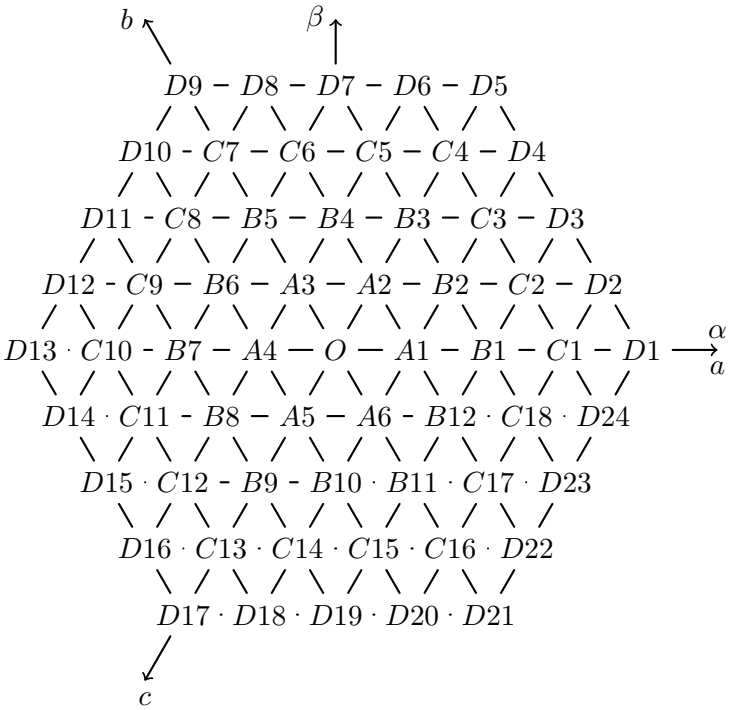

(b) Voltage vectors in the stator-stationary-frame

Figure 2.7: 5-level flying capacitor converter

2.3.3 5-level flying capacitor converter

The circuit diagram of a three-phase 5-level flying capacitor converter is shown in Figure 2.7(a). It consists of eight IGBT switches with free-wheeling anti-parallel diodes and three flying capacitors per phase. In this topology, the phase voltage of the converter is a function of the capacitor voltages and IGBT states

$$u_a = s_{a1}u_{\mathrm{dc}} + (s_{a2} - s_{a1})\, u_{C_{a3}} + (s_{a3} - s_{a2})\, u_{C_{a2}} + (s_{a4} - s_{a3})\, u_{C_{a1}}, \tag{2.10a}$$
$$u_b = s_{b1}u_{\mathrm{dc}} + (s_{b2} - s_{b1})\, u_{C_{b3}} + (s_{b3} - s_{b2})\, u_{C_{b2}} + (s_{b4} - s_{b3})\, u_{C_{b1}}, \tag{2.10b}$$
$$u_c = s_{c1}u_{\mathrm{dc}} + (s_{c2} - s_{c1})\, u_{C_{c3}} + (s_{c3} - s_{c2})\, u_{C_{c2}} + (s_{c4} - s_{c3})\, u_{C_{c1}}. \tag{2.10c}$$

If the voltages across the innermost to the outermost flying capacitors are set to 25%, 50% and 75% of the DC-link voltage, this topology operates as a 5-level converter. Table 2.5 displays the phase voltage levels of the converter at each switching state. It can be seen that there are 16 switching states and only 5 voltage levels. This high degree of per-phase redundancy is a unique feature of flying capacitor converters that facilitates flying capacitor voltage balancing.

It is worthy to mention that it is possible to increase the voltage levels of this flying capacitor converter to up to 16 levels by changing the flying capacitors' voltage ratio [11]. Apparently, increasing the voltage levels decreases the redundancy of switching states, and as a result makes the voltage balancing difficult and in some cases impossible. It is reported in [12] that voltage levels can be extended to 8 without a major effect on capacitor voltage balancing at medium and high switching frequencies. However, throughout this work, the 5-level flying capacitor converter is considered to work in the normal and not the extended operation mode.

In the same way as the 2-level converter, voltages can be transformed to stator-fixed coordinates via Clarke transformation. These voltage vectors are shown in the $\alpha\beta$ plain in Figure 2.7(b). Each voltage vector corresponds to a set of phase voltage levels. It is noteworthy that the sets of voltage levels which form a voltage vector are not unique. For example, voltage vector O represents five redundant states ($\{000\}$, $\{111\}$, $\{-1-1-1\}$, $\{222\}$, $\{-2-2-2\}$).

The voltage across each flying capacitor can be written as a function of the respective phase current and switching states

$$\frac{du_{Cx1}}{dt} = \frac{i_{C_{x1}}}{C_{\mathrm{FC}}} = (s_{x3} - s_{x4})\, \frac{i_x}{C_{\mathrm{FC}}}, \tag{2.11a}$$
$$\frac{du_{Cx2}}{dt} = \frac{i_{C_{x2}}}{C_{\mathrm{FC}}} = (s_{x2} - s_{x3})\, \frac{i_x}{C_{\mathrm{FC}}}, \tag{2.11b}$$
$$\frac{du_{Cx3}}{dt} = \frac{i_{C_{x3}}}{C_{\mathrm{FC}}} = (s_{x1} - s_{x2})\, \frac{i_x}{C_{\mathrm{FC}}}. \tag{2.11c}$$

Equations (2.11) represent the system model of the 5-level flying capacitor converter and are used to predict its behavior.

Table 2.5: Phase voltage levels of the 5L-FC converter

Voltage level	s_{x1}	s_{x2}	s_{x3}	s_{x4}	u_x	$i_{C_{x1}}$	$i_{C_{x1}}$	$i_{C_{x1}}$
-2	0	0	0	0	0	0	0	0
-1	0	0	0	1	$\frac{u_{\mathrm{dc}}}{4}$	$-i_x$	0	0
-1	0	0	1	0	$\frac{u_{\mathrm{dc}}}{4}$	i_x	$-i_x$	0
0	0	0	1	1	$\frac{u_{\mathrm{dc}}}{2}$	0	$-i_x$	0
-1	0	1	0	0	$\frac{u_{\mathrm{dc}}}{4}$	0	i_x	$-i_x$
0	0	1	0	1	$\frac{u_{\mathrm{dc}}}{2}$	$-i_x$	i_x	$-i_x$
0	0	1	1	0	$\frac{u_{\mathrm{dc}}}{2}$	i_x	0	$-i_x$
1	0	1	1	1	$\frac{3u_{\mathrm{dc}}}{4}$	0	0	$-i_x$
-1	1	0	0	0	$\frac{u_{\mathrm{dc}}}{4}$	0	0	i_x
0	1	0	0	1	$\frac{u_{\mathrm{dc}}}{2}$	$-i_x$	0	i_x
0	1	0	1	0	$\frac{u_{\mathrm{dc}}}{2}$	i_x	$-i_x$	i_x
1	1	0	1	1	$\frac{3u_{\mathrm{dc}}}{4}$	0	$-i_x$	i_x
0	1	1	0	0	$\frac{u_{\mathrm{dc}}}{2}$	0	i_x	0
1	1	1	0	1	$\frac{3u_{\mathrm{dc}}}{4}$	$-i_x$	i_x	0
1	1	1	1	0	$\frac{3u_{\mathrm{dc}}}{4}$	i_x	0	0
2	1	1	1	1	u_{dc}	0	0	0

2.3.4 Converter power losses

Total power losses of a power converter can be divided into blocking losses, control losses, conduction losses and switching losses. According to the reverse conduction characteristic of switching devices, a reverse voltage in the blocking state results in a very small reverse current that causes the blocking losses. Besides, a control current is necessary to turn a device on or off, which leads to control losses of the device. Both blocking and control losses are relatively small and negligible [13].

Based on the conduction characteristic, there is a voltage drop across the device while it is conducting. This leads to conduction losses. The forward characteristics of the IGBT and the diode that are used in the test set-up are shown in Figures 2.8 and 2.9. It can be seen that the conduction losses depend mainly on the load current.

During the transient from the blocking to the conducting state and vice versa, high values of current and voltage appear simultaneously for a very short time. This is the source of the switching losses. Turn-on and turn-off energy losses of the IGBT that is used in the test set-up are shown in Figure 2.10 and the reverse recovery energy of the diode used is shown in Figure 2.11.

Switching losses of the converter can be written as a function of energy losses and switching frequency. So for the IGBT

$$P_{\mathrm{sw}} = f_{\mathrm{sw}} \left(E_{\mathrm{on}} + E_{\mathrm{off}} \right), \tag{2.12}$$

where E_{on} and E_{off} are turn-on and turn-off energy losses and f_{sw} is the switching frequency of the device.

And for the diode

$$P_{\mathrm{sw}} = f_{\mathrm{sw}} E_{\mathrm{rec}}, \tag{2.13}$$

where E_{rec} is the reverse recovery energy of the diode. Even though E_{on}, E_{off} and E_{rec} depend on the collector current, it can be argued that the dominant term that defines the switching losses is the switching frequency, because energy losses are in the range of 2 to 15 mJ, while switching frequency is in the range of several hundreds to several thousand Hz.

Blocking, control and conduction losses of a converter mainly depend on the characteristics of semiconductor devices, the converter design and the load current. Hence, they are hardly affected by the modulation or control scheme. On the contrary, switching losses are linearly proportional to the switching frequency which can be adjusted by a modulator.

Due to the fact that switching losses are the only part of converter losses which are influenced by the modulator design, converter losses are chiefly understood as switching losses throughout this work.

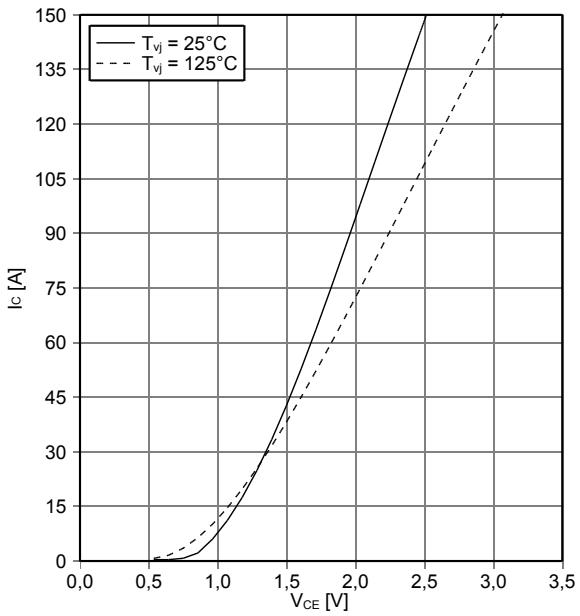

Figure 2.8: Forward characteristic of the IGBT that is used in the test set-up [14]

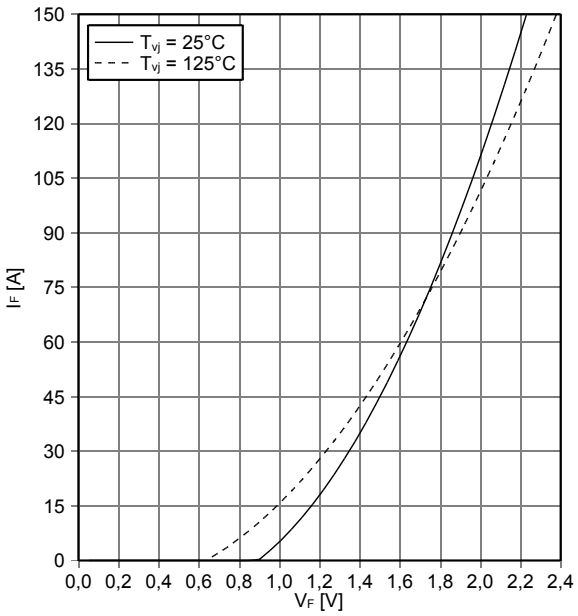

Figure 2.9: Forward characteristic of the diode that is used in the test set-up [14]

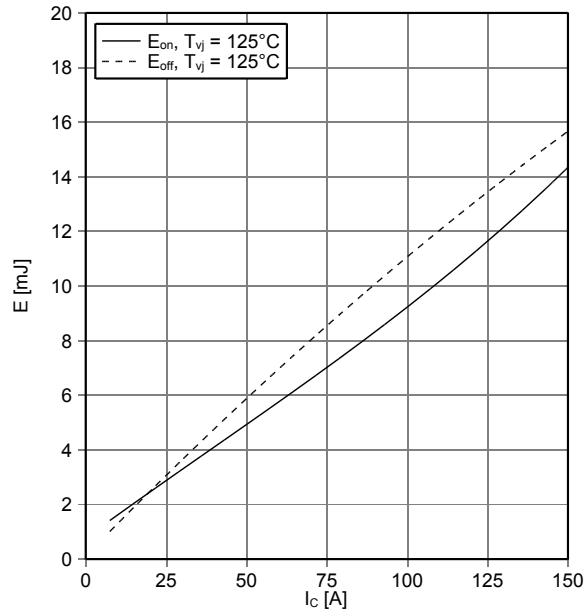

Figure 2.10: Turn-on and turn-off energy losses of the IGBT that is used in the test set-up [14]

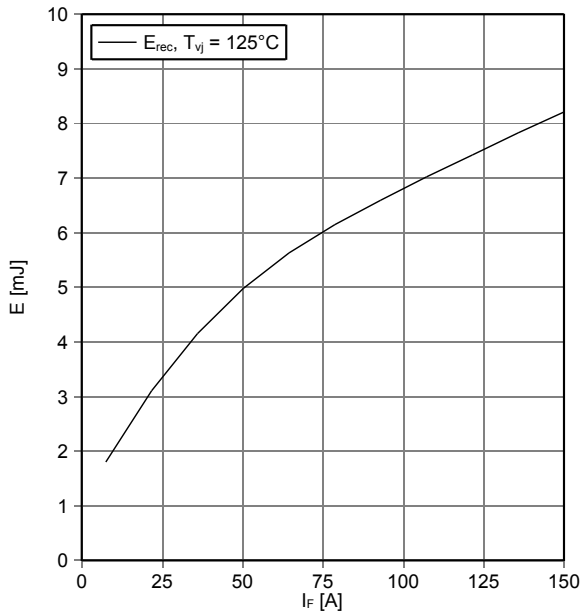

Figure 2.11: Reverse recovery energy of the diode that is used in the test set-up [14]

2.4 Modulation schemes

In principle, modulation is the process of varying one or more properties of a periodic waveform, called the carrier signal, with a modulating signal that typically contains information to be transmitted. Pulse Width Modulation (PWM) is a technique to encode a signal to a pulse train. In controlling power converters, the aim is to create trains of switched pulses that have the same fundamental volt-second average as a target reference waveform at any instant. The basic principle of Sinusoidal Pulse Width Modulation (SPWM) is shown in Figure 2.12, where a sinusoidal reference is compared with a triangular signal to generate a pulse train.

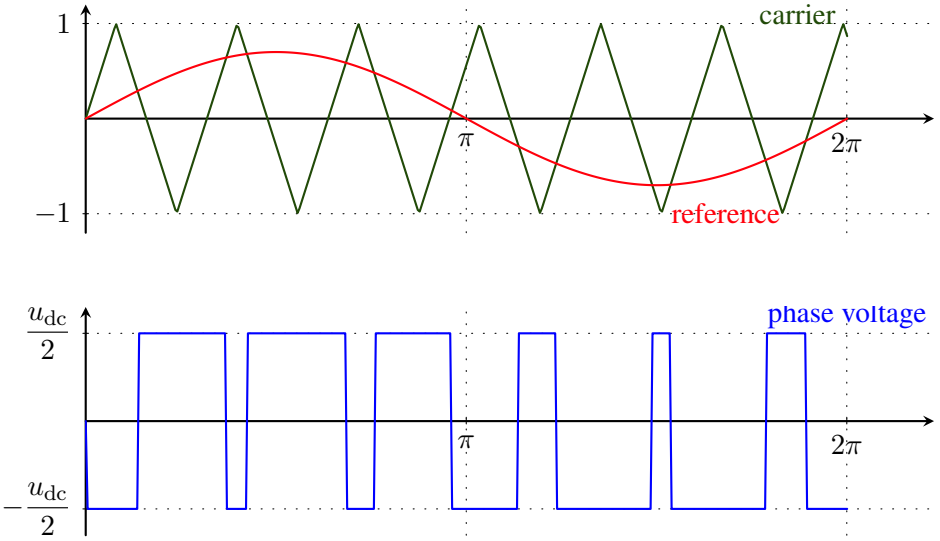

Figure 2.12: Principle of Sinusoidal Pulse Width Modulation (SPWM)

It is interesting to note that the rms value of the pulse train is independent of its switching frequency and its fundamental component amplitude.

$$u_{\text{rms}} = \sqrt{\frac{1}{T}\int_0^T \left(\frac{u_{\text{dc}}}{2}\right)^2} = \frac{u_{\text{dc}}}{2} \tag{2.14}$$

The RMS value of the signal squared or, in other words, the energy of the signal is the sum of the RMS value of its first harmonic squared, triplen harmonics squared and non-triplen harmonics squared.

$$u_{\text{rms}}^2 = u_{1,\text{rms}}^2 + \left(u_{3,\text{rms}}^2 + u_{9,\text{rms}}^2 + \ldots\right) + \left(u_{5,\text{rms}}^2 + u_{7,\text{rms}}^2 + \ldots\right) \tag{2.15}$$

The aim of any modulation technique is to control the first harmonic of the spectrum; however, a good modulation scheme will distribute the rest of the pulse train's energy in a way that the Weighted Total Harmonic Distortion (WTHD) is low. In power electronics, we usually use three-phase star connected loads with a floating neutral point. This cancels out all triplen harmonics from the load current. Moreover, taking into account that the load is typically

highly inductive, the nth harmonic squared, $i^2_{n,\mathrm{rms}}$, can be considered proportional to $\left(\frac{u_{n,\mathrm{rms}}}{n}\right)^2$. Therefore, equation (2.15) can be rewritten for the load current as

$$i^2_{\mathrm{rms}} \propto u^2_{1,\mathrm{rms}} + \left(\frac{u^2_{5,\mathrm{rms}}}{25} + \frac{u^2_{7,\mathrm{rms}}}{49} + \frac{u^2_{11,\mathrm{rms}}}{121} + \dots\right). \tag{2.16}$$

It can be seen in (2.16) that higher harmonics of the voltage are attenuated in the current spectrum due to the inductive characteristics of the load that behaves more or less like a low pass filter. This is why, a good modulator for electrical drives should be able to set the first harmonic of the pulse train based on the reference value and push the remaining portion of the signal's energy as much as possible to triplen harmonics and the rest to higher order harmonics. Pushing harmonics to high orders is mainly possible by increasing the carrier wave frequency, which results in an increase in the switching frequency and hence, the switching losses. So a trade-off shall be made between switching losses of the converter and the harmonic distortion of the current.

2.4.1 Programmable modulation schemes

As the switching frequency in low voltage drives is usually as high as several kHz, the main portion of the pulse train's energy is distributed among higher order harmonics. Thus, standard PWM or SVM techniques commonly result in relatively low current distortion. In contrast, the switching frequency of the converter in MV drives is limited to a few hundred Hertz due to power loss limitations. The challenge is to distribute harmonics in a way to get lower current distortion without increasing the switching frequency.

2.4.1.1 Selective harmonic elimination

Selective harmonic elimination (SHE) was proposed in the early 1960s to eliminate two lower order harmonics by introducing additional switching angles in the pulse train [15]. Switching angles were obtained by solving Fourier series expressions of harmonic components, and the fundamental frequency component of the load voltage was controlled by introducing a phase shift between inverter phase legs. Based on this idea, generalized methods were developed to eliminate a predefined number of lower order harmonic components and maintain the desired value of the fundamental component, for a given number of switching angles [3, 16].

The procedure to apply SHE techniques to MLCs is selection of waveform symmetry (usually quarter-wave and half-wave symmetries), identification of all possible multilevel waveforms for a given number of switching angles, calculation of the switching angles that satisfy the given requirements, and assignment of switching angles to each semiconductor device that depends on the converter topology. For multilevel waveforms, usually quarter-wave and half-wave symmetries are introduced. SHE techniques are widely used for MLCs [3, 17–24].

Several attempts have been made to obtain the switching angles in real-time. The main issue with online implementation is increased complexity and higher computational burden to solve a system of equations. One proposed method is to train artificial neural networks with complete and detailed knowledge of switching angle solutions and then utilize the same for obtaining switching angles in real time for a given modulation index [25]. In another attempt,

MPC-based SHE has been suggested to eliminate lower order harmonics in real time [26]. This proposed method utilizes sliding discrete Fourier transformation to obtain amplitudes of harmonic components in real-time. Switching states are then obtained using a predictive model in order to eliminate the undesired harmonics [3].

The main advantage of the SHE technique is that elimination of lower order harmonics is achieved with few commutations in a fundamental cycle. Hence, switching losses as well as filter sizes are significantly reduced in high-power applications. Due to reduced switching losses, it is possible to achieve higher converter efficiency and enable air cooling [3].

As explained in the previous part, the energy present in the eliminated harmonics is distributed over the non-eliminated harmonics, and hence, their amplitudes tend to increase. Therefore, elimination of lower order harmonics never leads to the best system performance. The conclusion is that it is better to use degrees of freedom for minimization of overall harmonics rather than complete elimination of certain lower order harmonics [3].

2.4.1.2 Optimal schemes

Optimal PWM techniques have been developed based on the fact that minimization of overall harmonics is better than complete elimination of certain lower order harmonics [27]. Besides, optimal PWM leads to easier convergence and increased continuity in the solution space. The optimization technique determines the switching patterns based on minimizing a cost function or performance index.

PWM and SVM techniques position the pulses within a fixed clock cycle. To improve their performance, optimal sub-cycle modulation or, in other words, Optimal Space Vector Modulation (OSVM) [28] was introduced, in which the sub-cycle durations of SVM are adjusted in such a way that constant and minimum current distortion are achieved throughout the fundamental period. The cycle duration variations are based on the fact that when the reference voltage vector is close to one of the converter's voltage vectors, less switching is needed in order to approximate the reference signal. Conversely, when the reference is closer to the middle of two voltage vectors, more switching is needed for an accurate approximation. Thus, the sub-cycle durations can be increased in the areas close to the converter's voltage vectors and decreased in the area between them in order to achieve constant and minimum current distortion. Note that with this method, less switching takes place at the corners of the voltage hexagon and more switching takes place in the area between voltage vectors; however, the switching frequency over the fundamental period remains constant.

Optimal durations are calculated offline and stored in memory with the modulation index as parameter. During operation, on-durations of the switching state vectors are computed by SVM and the value of sub-cycle duration that corresponds to the actual operating point is retrieved from memory.

OSVM reduces current distortion resulting from the space vector modulation algorithm, but does not minimize it over the whole fundamental period. To achieve optimum current distortion, the concept of clocking the pulses can be completely eliminated. In this method, switching events are allowed to take place freely over the fundamental period with the constraint of maintaining waveform symmetry. Commutation angles can be calculated to achieve the desired modulation index while minimizing current distortion [1].

This method is known as Optimal Pulse Pattern (OPP) or Optimal Synchronous Modulation

(OSM). It was proposed first in the late 70s [29] and has been further developed in [30] for current distortion optimization of MV drives, in [31, 32] for 3- and 5-level converters and in [33–38] to overcome transient response issues in its application for MV drives.

2.4.2 Direct methods

A typical power electronics controller consists of a main controller with analogue - in most cases sinusoidal - output, a modulator to modulate the analogue output in the form of a pulse train and a converter. In direct methods, the modulator is completely eliminated and the controller is designed in such a way that it directly generates a pulse train. Direct Torque Control (DTC) [39] and Direct Self Control (DSC) [40] are both hysteresis type controllers and apply the concept of direct modulation. Finite Control Set Model Predictive Control (FCS-MPC), which is extensively explained in chapter 3, is a direct method. Simplicity and lower current distortion at low switching frequencies are the main advantages of a direct method. However, variable switching frequency and the necessity for higher sampling time are their main drawbacks.

In principle, SHE and optimal modulation techniques have precalculated look-up tables from which switching instances are fetched based on the operating point. From this perspective, they could be considered as direct methods as well. However, a method is called direct only if the switching states of the converter are directly chosen by the controller. As a result, optimal modulation and SHE schemes in which the controller's output is a continuous voltage vector are considered as programmable modulation schemes.

2.4.3 Reference summary for low switching frequency modulation schemes

A reference summary for low switching frequency modulation schemes based on the application and reference device switching frequency is given in Table 2.6.

Table 2.6: Low switching frequency modulation schemes [3]

Method	Application	$f_{\mathrm{sw}} < 200$ Hz	200 Hz $< f_{\mathrm{sw}} <$ 500 Hz	500 Hz $< f_{\mathrm{sw}} <$ 1 kHz
SVM	Drives	-	-	[41, 42]
OSVM	Drives	-	-	[28]
SHE	Drives	[15, 43–45]	-	-
	AFE Rectifiers	[46]	[47]	-
	STATCOM	-	[48]	-
	Photovoltaic	[49]	-	-
	RL Load	-	[50, 51]	-
OPP	Drives	[29–38, 52, 53]	-	-
	AFE Rectifiers	[54]	-	-
MPC	RL load	-	[55, 56]	[57]
	Drives	[58]	[59–64]	-
	AFE Rectifiers	[65]	[66]	-
	wind power	-	[67–69]	[70]
	STATCOM	-	[71]	-

2.5 Controller and observer design

In principle, all classical closed-loop control algorithms of an induction motor can be divided into two groups: Field Oriented Control (FOC) and Direct Torque Control (DTC) [39].

It is well known that the DC motor drive has an excellent dynamic performance. This is mainly due to the decoupled control of the stator magnetic field and the electromagnetic torque of the motor. FOC, also known as vector control, emulates the DC motor control for AC machines. Using a proper field orientation, the stator current can be decomposed into a flux-producing component and a torque-producing component. These two components are then controlled separately [72].

In the DTC scheme, on the other hand, the electromagnetic torque of the motor is controlled directly. The stator flux amplitude and electromagnetic torque are monitored with a high sampling rate. When the hysteresis bands are exceeded, based on the stator flux position a voltage vector is applied from a switching table in order to bring the torque or stator flux back into the boundary.

Several advanced controllers are proposed for induction motor drives which share some basic principles with FOC and DTC algorithms. A popular example is model predictive control which is analyzed in detail in the next chapter.

Any closed-loop control scheme requires feedback from physical variables of the machine, consisting: the mechanical speed and in some cases the rotor position, phase currents, stator and rotor fluxes. Speed, position and phase current can be directly measured; however, stator and rotor fluxes need to be estimated from the measured signals.

2.5.1 Voltage model flux observer

A very common flux estimator is the so-called voltage model. According to equation (2.3), the stator flux $\boldsymbol{\psi}_\mathrm{s}$ can be calculated based on applied voltages and measured currents

$$\boldsymbol{u}_\mathbf{s} = R_\mathrm{s}\boldsymbol{i}_\mathbf{s} + \frac{d\boldsymbol{\psi}_\mathbf{s}}{dt}. \tag{2.17}$$

Then the rotor flux $\boldsymbol{\psi}_\mathbf{r}$ can be calculated based on the estimated stator flux and measured phase currents

$$\boldsymbol{\psi}_\mathbf{r} = \frac{L_\mathrm{r}}{L_\mathrm{m}}\boldsymbol{\psi}_\mathbf{s} - \left(\frac{L_\mathrm{r}L_\mathrm{s}}{L_\mathrm{m}} + L_\mathrm{r}\right)\boldsymbol{i}_\mathbf{s}. \tag{2.18}$$

Two main problems of the voltage model observer are the stator resistance variation and the open-loop integration (integration without feedback), which can lead to convergence problems. R_s variation does not deteriorate the precision of the flux estimation unless the machine is operated at a very low speed. In such a case, a different flux observer has to be used. Moreover, convergence problems can be solved by using a low pass filter instead of an integrator. Taking these measures into account, the voltage based flux observer is usually accurate enough to examine the performance of a control algorithm.

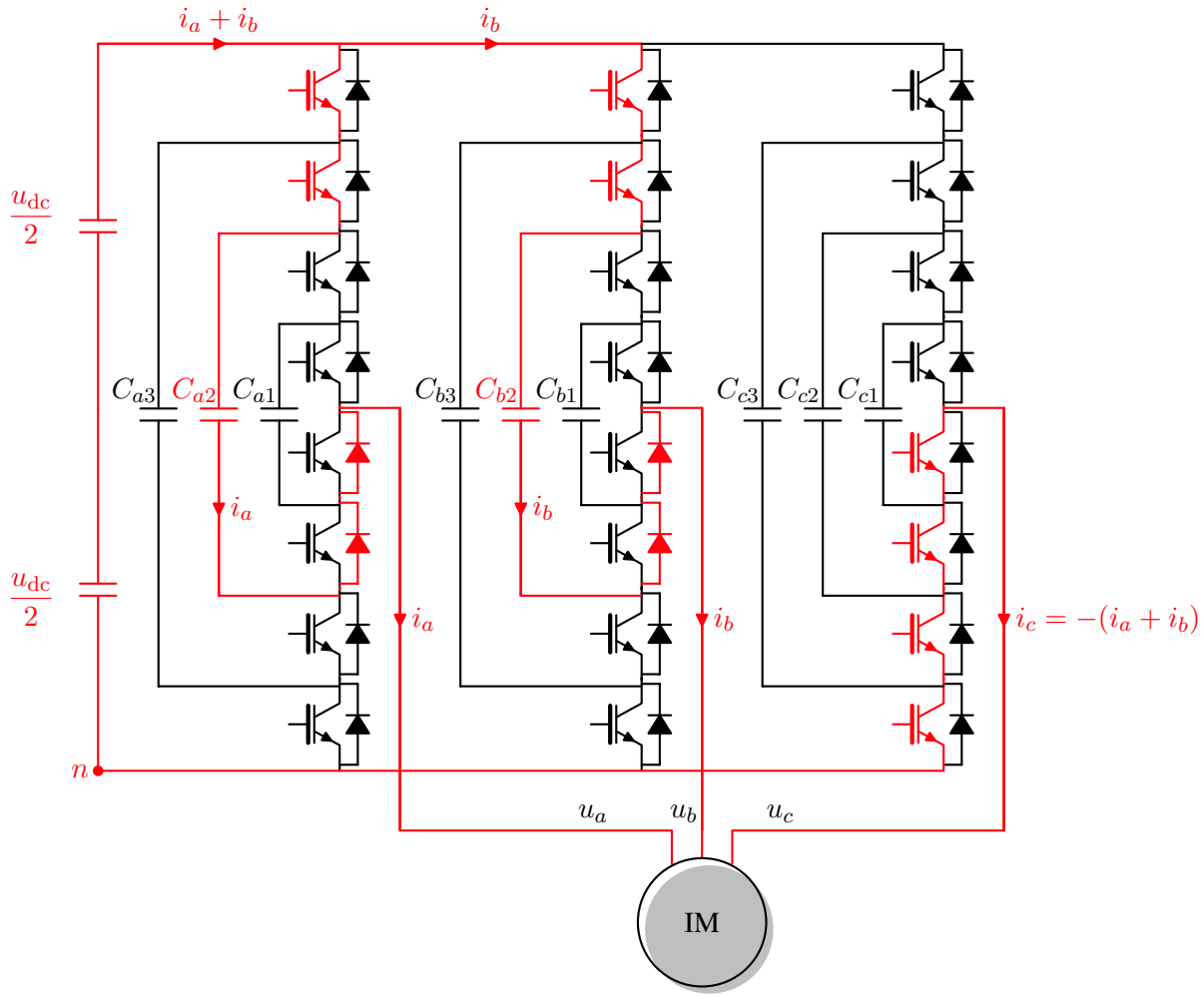

Figure 2.13: Current flow path while applying the voltage vector $\{110\}$ to the 5-level FC converter

In this work, a 5-level flying capacitor converter is used. Although 5-level converters are used in the MV range, based on the available resources it was only feasible to design a $20\ \mathrm{kW}$ prototype. The power rating of the induction motor used is $3\ \mathrm{kW}$. Operating a 5-level converter at such a low power rating makes flux estimation challenging. Let us consider the case in which the voltage vector $\{110\}$ is applied to the converter. The current flow path is shown in Figure 2.13. For phases a and b, current will flow from the DC-link to the load through the two upper IGBTs, the middle flying capacitors and two diodes in the lower part. In phase c, the current flows from the load to the DC-link through four IGBTs in the lower part. Therefore, based on equation (2.10), the phase voltages are expected to be

$$
\begin{aligned}
u_a &= s_{a1}u_{\mathrm{dc}} + (s_{a2} - s_{a1})\, u_{C_{a3}} + (s_{a3} - s_{a2})\, u_{C_{a2}} + (s_{a4} - s_{a3})\, u_{C_{a1}} = \frac{u_{\mathrm{dc}}}{2}, \\
u_b &= s_{b1}u_{\mathrm{dc}} + (s_{b2} - s_{b1})\, u_{C_{b3}} + (s_{b3} - s_{b2})\, u_{C_{b2}} + (s_{b4} - s_{b3})\, u_{C_{b1}} = \frac{u_{\mathrm{dc}}}{2}, \\
u_c &= s_{c1}u_{\mathrm{dc}} + (s_{c2} - s_{c1})\, u_{C_{c3}} + (s_{c3} - s_{c2})\, u_{C_{c2}} + (s_{c4} - s_{c3})\, u_{C_{c1}} = 0.
\end{aligned}
$$

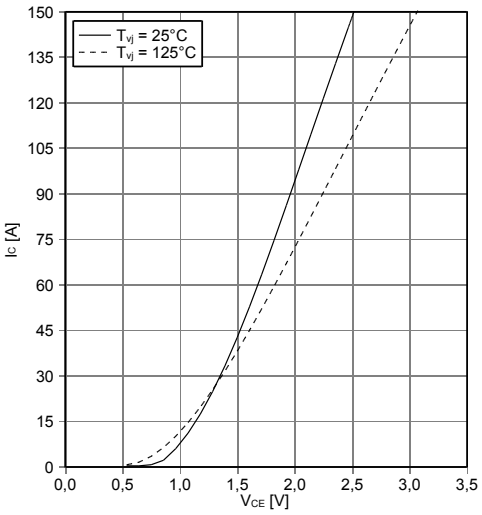

Figure 2.14: Voltage drop of the IGBTs used in the test set-up [14]

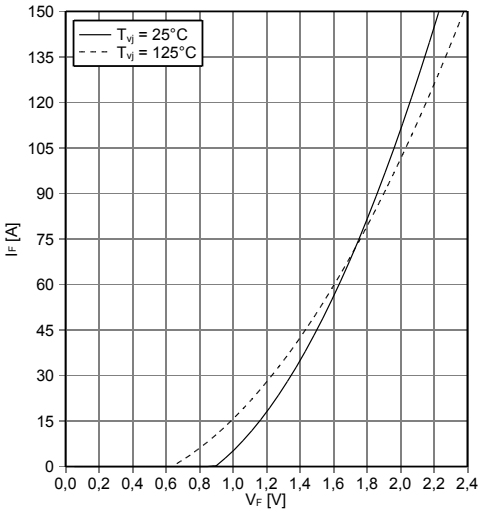

Figure 2.15: Voltage drop of the diodes used in the test set-up [14]

However the phase voltages on the machine terminals would differ from the calculated values. In this case, the voltage drop over two IGBTs, two diodes and one flying capacitor affects u_a and u_b, and the voltage drop over four IGBTs affects u_c. From the forward characteristics of the IGBTs and the diodes, shown in Figures 2.14 and 2.15, it can be seen that for a load current ranging from 0 to 10 A, the voltage drop over each IGBT is in the range of 0.8 to 1 V. The voltage drop over each diode is in the range of 0.9 to 1.1 V. Setting the DC-link voltage to 600 V, the voltages over C_{a2} and C_{b2} are expected to be 300 V. Considering a 5% voltage ripple over the flying capacitors means that the voltage over C_{a2} and C_{b2} will in fact be 300 ± 15 V. Hence, in the worst case, the phase voltages u_a, u_b and u_c are 281 V, 281 V and 4 V instead of 300 V, 300 V and 0 V. It is worth mentioning that the maximum voltage drop across the stator resistance is around 15 V, which in this case is smaller than the converter voltage drop.

In medium and high voltage applications, a voltage drop in the range of 20 V is negligible. Conversely, neglecting such a voltage drop deteriorates flux estimation and thus the control performance of small drives. So the options to circumvent these drawbacks are either considering a very detailed model of the converter in which voltage drops over switches and voltage ripples over flying capacitors are taken into account or choosing another method for flux observation in which stator voltages are not used.

2.5.2 Current model flux observer

The other possibility to estimate the rotor flux, without using the stator voltages, is the so-called current model observer. According to equation (2.3), the rotor flux $\boldsymbol{\psi}_\mathrm{r}$ can be calculated based on the measured currents and mechanical speed

$$\boldsymbol{\psi}_\mathrm{r} + \frac{L_\mathrm{r}}{R_\mathrm{r}} \frac{\mathrm{d}\boldsymbol{\psi}_\mathrm{r}}{\mathrm{dt}} = L_\mathrm{m} \boldsymbol{i}_\mathrm{s} + j\omega_\mathrm{e} \frac{L_\mathrm{r}}{R_\mathrm{r}} \boldsymbol{\psi}_\mathrm{r}. \tag{2.19}$$

Then the rotor flux $\boldsymbol{\psi}_{\mathrm{r}}$ can be calculated based on the estimated rotor flux and measured phase currents

$$\boldsymbol{\psi}_{\mathrm{s}} = \frac{L_{\mathrm{m}}}{L_{\mathrm{r}}} \boldsymbol{\psi}_{\mathrm{r}} + \left(L_{\mathrm{s}} + L_{\mathrm{m}}\right) \boldsymbol{i}_{\mathrm{s}}. \tag{2.20}$$

This estimation is still parameter-dependent; however, it is not affected by the voltage ripple of flying capacitors and voltage drops across switching devices.

2.6 Test bench

The proposed algorithms of this work are implemented in a laboratory setup that includes a real-time system, a power converter and two electrical machine.

A dSpace system is used as a real-time system that consists of an A/D board (ds2004), a PWM board (ds5101), an encoder board (ds3002) and a processor board (ds1006).

The inverter is a 5-level flying capacitor converter with the parameters given in Table 2.7. It is a $20\ \mathrm{kW}$ prototype design with Infineon FF75R12YT3 dual IGBT modules (Figure 2.16), Power Integrations 2SC0108T2Dx-12 gate drive units (Figure 2.17) and low stray inductance ($14\ \mathrm{nH}$) flying capacitors from Epcos.

The electrical machine which is used to be controlled is a two pole-pairs $3\ \mathrm{kW}$ induction motor with the parameters given in Table 2.8. The laboratory test set-up is shown in Figure 2.18. Another $5.5\ \mathrm{kW}$ induction motor is also used as a load.

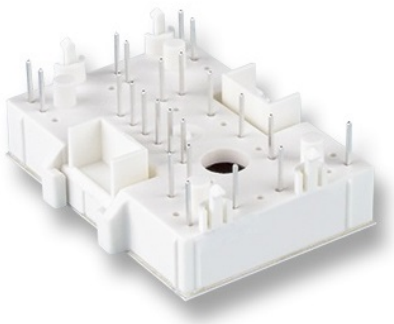

Figure 2.16: Infineon FF75R12YT3 dual IGBT with anti-parallel diode modules

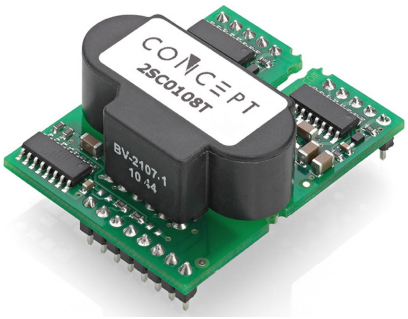

Figure 2.17: Power Integrations 2SC0108T2Dx-12 gate drive unit

Figure 2.18: Laboratory set-up

Table 2.7: 5L-FC converter parameters

Parameter	Value
u_{dc}	600 V
P_{n}	20 kW
C_{FC}	680 μF
C_{dc}	2000 μF

Table 2.8: Induction motor parameters

Parameter	Value
P_{n}	3 kW
ω_{n}	1440 rpm
R_{s}	1.5 Ω
R_{r}	1.4 Ω
L_{s}	197 mH
L_{r}	197 mH
L_{m}	191 mH

CHAPTER 3

Model predictive control - state of the art

This chapter provides background information on Model Predictive Control (MPC) and its application in electrical drives. The following questions are addressed in this part:

- Why MPC?
- What is MPC?
- Why MPC in electrical drives?
- How was MPC developed and raised in the power electronics and drives community?

3.1 Background

All practical problems are subject to constraints of different types. These constraints can be sometimes ignored in design procedures, but when the system is working close to a constraint boundary, they cannot be neglected. In such cases, it is desirable to consider constraints at the beginning of the problem formulation. Various tools, such as anti-windup strategies, have been developed for this purpose. They are probably adequate for simple problems; however, for more complex MIMO problems - especially those having both input and state constraints - a classical approach for dealing with constraints is needed [73]. The capability of Model Predictive Control to handle constraints in a simple and effective manner resulted in its application in order to overcome these issues in its early stages.

The original idea of Model Predictive Control (MPC) and Receding Horizon Control (REC) can be traced back to the 1960s when it was used as a mean to deal with multivariable constrained control problems [74]. The oil, the chemical and the process industry were pioneers in the adoption of MPC, while the first attempt to apply it to an electrical drive system was made more than two decades later [75,76]. Ever since, it has been applied in many different areas, and

various fields have developed their own notation and formulation of the problem, thus creating some confusion about the names used. For example:

- Receding Horizon Control [77]
- Model Predictive Heuristic Control [78, 79]
- Dynamic Matrix Control [80]
- Quadratic Matrix Control [81]
- Adaptive Predictive Control [81]
- Generalized Predictive Control [82]
- Sequential Open-loop Optimization [81]
- Finite Control Set Model Predictive Control [83]
- ...

The above mentioned algorithms are not exactly the same; however, they share common principles that distinguishes MPC from other algorithms:

- a plant model,
- the receding horizon idea,
- an objective function,
- the optimization principle.

3.1.1 Plant model

MPC is a model-based control strategy in which the system model is used to predict the system behavior in response to a set of inputs. For a system with a state vector $\boldsymbol{x}(t) = [x_1(t), x_2(t), ..., x_n(t)]^T \in \mathbb{R}^n$, an input vector $\boldsymbol{u}(t) = [u_1(t), u_2(t), ..., u_m(t)]^T \in \mathbb{R}^m$ and an output vector $\boldsymbol{y}(t) = [y_1(t), y_2(t), ..., y_p(t)]^T \in \mathbb{R}^p$ and $t \in \mathbb{R}$, the system model can be represented by:

$$\frac{d\boldsymbol{x}(t)}{dt} = f(\boldsymbol{x}(t), \boldsymbol{u}(t), t), \tag{3.1a}$$

$$\boldsymbol{y}(t) = g(\boldsymbol{x}(t), \boldsymbol{u}(t), t), \tag{3.1b}$$

where (3.1a) is the state equation and (3.1b) the output equation. In most applications, systems are considered either Linear Time Invariant (LTI) or are linearised around an operating point. In this case, the equations can be expressed as:

$$\frac{d\boldsymbol{x}(t)}{dt} = \boldsymbol{F}\boldsymbol{x}(t) + \boldsymbol{G}\boldsymbol{u}(t), \tag{3.2a}$$

$$\boldsymbol{y}(t) = \boldsymbol{C}\boldsymbol{x}(t) + \boldsymbol{D}\boldsymbol{u}(t), \tag{3.2b}$$

where $\boldsymbol{F} \in \mathbb{R}^{n\times n}$ is the state matrix, $\boldsymbol{G} \in \mathbb{R}^{n\times m}$ the input matrix, $\boldsymbol{C} \in \mathbb{R}^{n\times n}$ the output matrix and $\boldsymbol{D} \in \mathbb{R}^{p\times m}$ the feed-forward matrix, which is considered to be zero in our case. Moreover, the system model is often discretized due to digital implementation. So equation (3.2) is rewritten in a discrete form with $t = kT_s$, where $k \in \mathbb{R}_0$ represents the kth time step and T_s the sampling interval:

$$\boldsymbol{x}(k+1) = \boldsymbol{A}\boldsymbol{x}(k) + \boldsymbol{B}\boldsymbol{u}(k), \tag{3.3a}$$

$$\boldsymbol{y}(k) = \boldsymbol{C}\boldsymbol{x}(k), \tag{3.3b}$$

in which $\boldsymbol{x}(k)$, $\boldsymbol{u}(k)$ and $\boldsymbol{y}(k)$ are defined in the same manner as the vectors $\boldsymbol{x}(t)$, $\boldsymbol{u}(t)$ and $\boldsymbol{y}(t)$, $\boldsymbol{A} = e^{\boldsymbol{F}T_s}$ and $\boldsymbol{B} = -\boldsymbol{F}^{-1}(\boldsymbol{I} - \boldsymbol{A})\boldsymbol{G}$. Moreover, for predictions that span multiple time-steps based on a measurement taken at time-step k, the predicted state vector at time-step $k + l$ is shown by $\boldsymbol{x}(k + l|k)$, where:

$$\boldsymbol{x}(k + l|k) = \boldsymbol{A}\boldsymbol{x}(k + l - 1|k) + \boldsymbol{B}\boldsymbol{u}(k + l - 1|k). \tag{3.4}$$

In applications with relatively small sampling intervals - in the range of $100\mu s$ - matrix A can be simplified to only the first two terms of its *Euler* series: $\boldsymbol{A} = (\boldsymbol{I} + \boldsymbol{F}T_s)$ and $\boldsymbol{B} = \boldsymbol{G}T_s$, where $\boldsymbol{I}$ is the identity matrix.

3.1.2 Receding horizon

The receding horizon idea resembles to chess, in which players analyze the present situation, predict several successive moves but perform a single move. Then, instead of strictly following their plan of action to the very end, they reconsider their prediction each round, adjusting it to the new situation, and perform another single move. This is the main idea of receding horizon control.

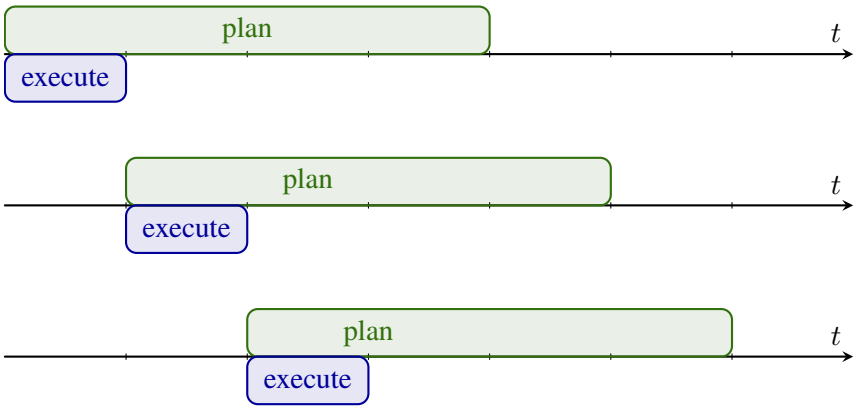

Figure 3.1: Principle of the receding horizon

Figure 3.1 shows the basic principle of the receding horizon idea. In each sample time, successive actions are planned within the prediction horizon. However, only the first action is applied in the next sampling time and precalculations are repeated based on new feedback and/or updated reference signals. All of the precalculations are based on the measured signal at the present time; nonetheless, the plan considers several sample times in the future. During predictions, no feedback is available for the forthcoming sample times, so the planning is open-loop. A closed-loop control and, in other words, the inclusion of feedback in precalculations is achieved by means of the receding horizon principle. For this reason, the receding horizon principle can be considered as feedback for MPC.

3.1.3 Objective function

An objective or cost function is the central part of a predictive controller. It simply translates the user's performance expectations for the controller. As most control problems are known to be reference tracking problems, objective functions are commonly a summation of several errors with weighting factors. However, secondary goals such as current distortion, power loss, device temperature, acoustic noise etc. can be included in an objective function as well. The following choice is a general form of the objective function and encompasses many alternatives documented in the literature

$$J = f(\boldsymbol{x}(k+1|k), \boldsymbol{x}(k+2|k), \ldots, \boldsymbol{x}(k+N|k)), \boldsymbol{u}(k), \boldsymbol{u}(k+1), \ldots, \boldsymbol{u}(k+N-1)) \quad (3.5)$$

Due to the existence of several classical approaches to solve quadratic or linear problems, it is often preferred to formulate the objective function in the quadratic or linear form as well. A typical first norm or linear objective function is

$$J = \sum_{i=k}^{k+N-1} \|\boldsymbol{x}'(i+1|k)\|_1^1 + \boldsymbol{\lambda}_i \|\boldsymbol{u}(i)\|_1^1, \quad (3.6)$$

and a typical second norm or quadratic objective function is

$$J = \sum_{i=k}^{k+N-1} \|\boldsymbol{x}'(i+1|k)\|_2^2 + \boldsymbol{\lambda}_i \|\boldsymbol{u}(i)\|_2^2, \quad (3.7)$$

where $\boldsymbol{\lambda}_i$ is the weighting factor for the ith prediction, N the prediction horizon and $\boldsymbol{x}'(i+1|k) = \boldsymbol{x}(i+1|k) - \boldsymbol{x}^*(i+1|k)$ is the predicted error at the ith prediction.

3.1.4 Optimization

Considering the fact that classical Model Predictive Control is associated with a linear model, polyhedral constraints and a linear or quadratic objective function, the resulting optimization problem is a Linear Program (LP) or a Quadratic Program (QP). Some available techniques to solve LPs are [84, 85]:

- **Interior point:** Uses a primal-dual predictor-corrector algorithm and is especially useful for large-scale problems that have a structure or can be defined using sparse matrices,

- **Active-set:** Minimizes the objective at each iteration over the active set (a subset of the constraints that are locally active) until it reaches a solution,
- **Simplex:** Uses a systematic procedure for generating and testing candidate vertex solutions for a linear program. The simplex algorithm is the most widely used algorithm for linear programming.

And for quadratic programming [84, 86]:

- **Interior-point-convex:** solves convex problems with any combination of constraints,
- **Trust-region-reflective:** solves bound constrained or linear equality constrained problems,
- **Active-set:** solves problems with any combination of constraints.

Although the optimization for MPC first started with LP in 1963 [77], QP is more common nowadays - mostly due to its computational power advantages. Nevertheless, solving QP using general purpose methods can be too slow. This has traditionally limited MPC to the application on systems with slow dynamics, with sample times of several seconds or minutes. One method to apply MPC to dynamic systems is to compute the solution of QP explicitly as a function of the initial state [87, 88], the control action is then implemented online in the form of a lookup table. The major drawback here is that the dimensions of the lookup table increase exponentially with the prediction horizon, the state and the input dimensions.

If the cost function is a nonlinear function as in equation (3.5), nonlinear numerical optimization techniques are necessary for the optimization. Some common techniques are:

- **Gradient descent methods:** These methods provide a linear convergence based on negative gradient and a variable step size (λ_n). The advantage of this algorithm is that only the gradient matrix is used and not the Hessian matrix. Its drawbacks are difficulties in choosing step size, zigzag phenomenons around minima, and slow convergence. Based on this method the next iteration t^{n+1} to optimize the objective function $J(t_n)$ is [89]

$$t_{n+1} = t_n - \lambda_n \nabla J(t_n). \tag{3.8}$$

- **Newton methods:** Newton method exploits negative gradient and Hessian matrices. Thus it is a faster method; however, it needs a very high computational load. Based on this method the next iteration t^{n+1} to optimize the objective function $J(t_n)$ is [89]

$$t_{n+1} = t_n - \left[\nabla^2 J(t_n)\right]^{-1} \nabla J(t_n). \tag{3.9}$$

- **Gauss-Newton method:** It is a method to solve non-linear least square problems. It is a modification of Newton's method for finding a minimum of a function. Unlike Newton's method, the Gauss-Newton algorithm can only be used to minimize a sum of squared function values, but it has the advantage that second derivatives, which can be challenging to compute, are not required. In general a nonlinear least square optimization problem is

to find $t \in \mathbb{R}^n$ that minimizes $J(t) = \|\boldsymbol{R}(t)\|_2^2 = \sum_{i=1}^{m} r_i(t)^2$, where $\boldsymbol{R} : \mathbb{R}^n \to \mathbb{R}^m$. Given a starting guess t^n, $\boldsymbol{R}$ can be linearized around t^n [89]

$$\boldsymbol{R}(t) \approx \boldsymbol{R}(t^n) + \nabla \boldsymbol{R}(t^n)(t - t^n). \tag{3.10}$$

Thus

$$\|\boldsymbol{R}(t)\|_2^2 = \|\boldsymbol{A}^n t - \boldsymbol{B}^n\|_2^2, \tag{3.11}$$

where

$$\begin{aligned} \boldsymbol{A}^n &= \nabla \boldsymbol{R}(t^n), \\ \boldsymbol{B}^n &= \nabla \boldsymbol{R}(t^n) t^n - \boldsymbol{R}(t^n). \end{aligned}$$

The next iteration for this linearized least squares problem is

$$t^{n+1} = \left(\boldsymbol{A}^{nT} \boldsymbol{A}^n\right)^{-1} \boldsymbol{A}^{nT} \boldsymbol{B}^n. \tag{3.12}$$

In the special case in which the system input is limited to finite states, the optimization problem can be simplified to finding a minimum among the finite values of the objective function. This method is called Finite Control Set Model Predictive Control (FCS-MPC) in which the cost function is calculated for each finite state of the input and the input resulting in the minimum value of the cost function is selected. Although this approach is very simple, its calculation time increases exponentially with the prediction horizon. This makes the conventional FCS-MPC impractical for many MPC schemes, which require long prediction horizons.

3.2 MPC for electrical drives

It took almost two decades for MPC to find its way into the power electronics community. First ideas of applying MPC to electrical drives were expressed in the early 1980s by Holtz and Stadtfeld [75] and Kennel and Schröder [76]. They worked independently to apply predictive control to electrical drives. Having different objectives, they chose different schemes. Kennel-Schröder had the idea of developing a model-based controller that is superior to linear controllers due to consideration of system models. Here is a quote from their first paper: “One has to leave linear control theory and to consider the characteristics of load, converter and microcomputer ... To find an optimal algorithm, one has to know exactly the mathematical relations between the output signal, the reference signal and other influencing signals and parameters ...". Therefore, they decided to use a trajectory-based model predictive control. On the other hand, Holtz-Stadtfeld were facing the fact that standard modulation schemes lead to high harmonic distortion at low switching frequencies and hence are not suitable for MV drives. They looked for a substitute for the modulator that is especially superior at very low switching frequencies. Thus they chose a hysteresis-based MPC.

Several control schemes followed these two schemes which share some basic principles with them. For instance, bang-bang control can be regarded as a hysteresis-based predictive control, and Direct Self Control (DSC) can be considered as a trajectory-based predictive control. There

are also some control schemes that exploit various features from each approach. Sliding mode control and Direct Torque Control (DTC) are two examples [82].

A simple search on the IEEE index for MPC for electrical drives results in several thousand publications on the topic. However, there are only a few original contributions that can be clearly differentiated from the others. Some of these schemes which are more popular are discussed in this part.

3.2.1 Hysteresis-based predictive current control

The working principle of hysteresis-based predictive current control is shown in Figure 3.2. The current references are generated by the main controller and the current error vector which is the difference between a reference current, $\boldsymbol{i}_s^*$, and the actual current, $\boldsymbol{i}_s$, is monitored with a high sampling time. A boundary is considered for the reference current, and whenever a boundary condition occurs, the switching state of the converter is changed with the aim of maximizing the time between switching instances or, in other words, minimizing the switching frequency. This selection is made by optimizing the cost function - i.e. finding the switching vector that keeps the actual current longer in the boundary - by predicting the stator current. The performance of this controller can be improved for high modulation indexes by replacing the circular boundary with a rectangular boundary with larger d-axis excursions [2].

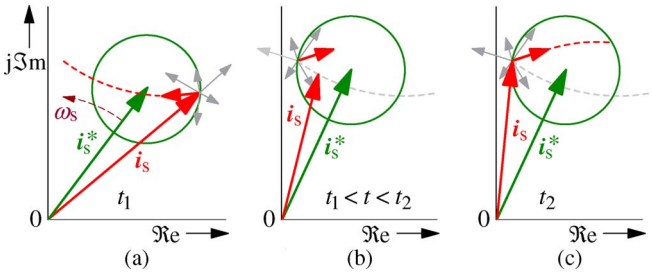

Figure 3.2: Working principle of hysteresis-based predictive current control [2]

A hysteresis-based predictive current control is simulated for an induction motor in order to show the properties of hysteresis control. Figure 3.3 shows the stator current vector in the $\alpha\beta$ plane. As can be seen, the controller provides very fast dynamics. Besides, it is noticeable that the current vector follows a trajectory resembling a triangle within the circular boundary. This is due to the objective of maximizing the time between switching instances at the border of a circular boundary.

Figure 3.4 shows α and β components of steady-state stator currents in time and Figure 3.5 depicts the current spectrum. It is evident that current harmonics are not shaped around multiples of the switching frequency as hysteresis-based predictive current control does not use any modulator and provides a variable switching frequency.

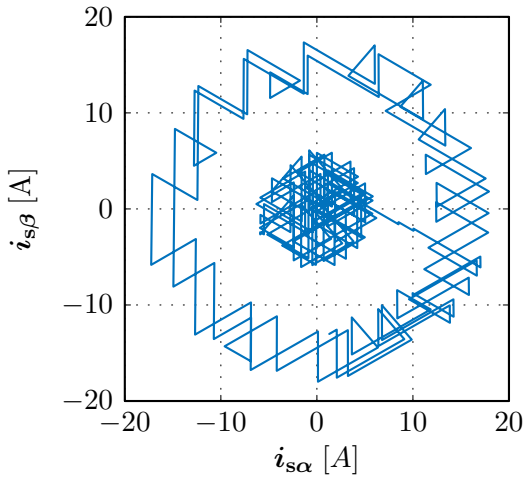

Figure 3.3: Stator current vector in the $\alpha\beta$ plane

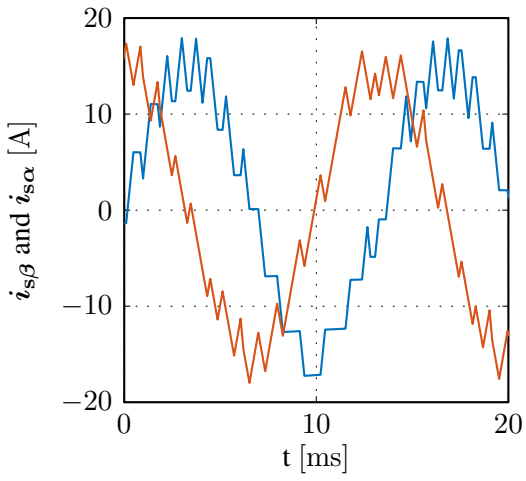

Figure 3.4: α and β components of the steady-state stator currents

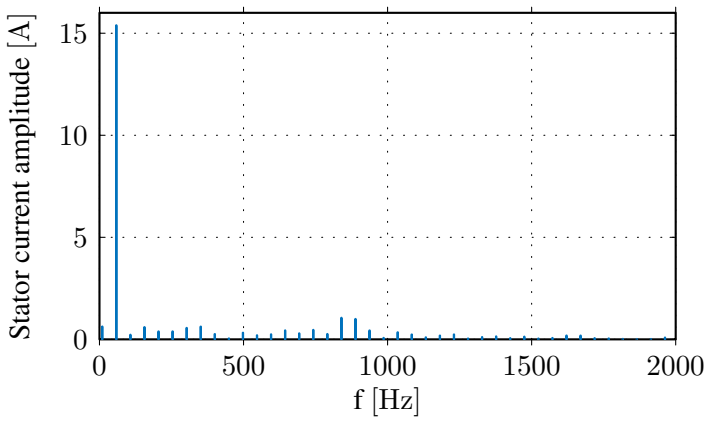

Figure 3.5: Stator current spectrum

3.2.2 Generalized predictive control

Generalized predictive control (GPC) was introduced by Clarke in 1987 [90,91]. It exploits a transfer function based on the CARIMA model and optimizes the objective function by setting its derivatives to zero. Thus mathematically complex solving algorithms like quadratic and linear programming are not required any more [82].

GPC was first applied to electrical drives by Kennel and Linder in 2001. They replaced inner current control loops and the outer speed control loop of a standard field oriented controller with GPC while keeping the modulator in place. Figure 3.6 shows the block diagram of a GPC scheme for electrical drives. Although GPC is simpler than many algorithms such as quadratic and linear programming it was not fast enough to be executed on a standard micro-controller or DSP in a fraction of millisecond back then. They were able to overcome this difficulty firstly by running their algorithm on a self designed real-time system and secondly by performing the calculations partly offline. By assuming, for instance, that machine parameters remain constant

during operation, it was possible to perform matrix inversions offline and store the results in memory.

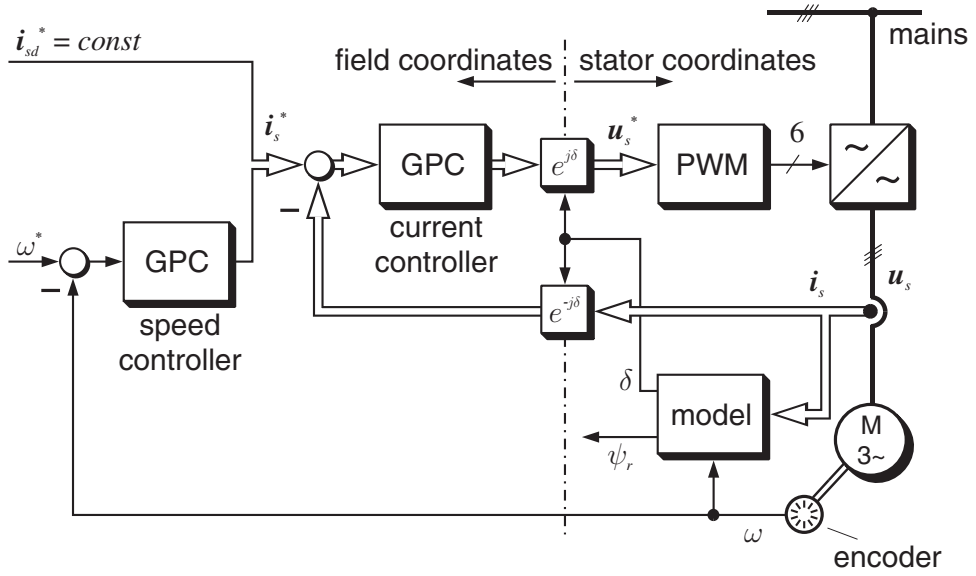

Figure 3.6: Generalized predictive control diagram [82]

3.2.3 Finite control set model predictive control

Finite Control Set Model Predictive Control (FCS-MPC) is the most popular predictive control scheme for power converters and electrical drives [83]. In FCS-MPC, finite states of power switches are directly implemented to the optimal problem formulation. As a result, firstly, the modulation stage is eliminated and secondly, the objective function optimization is converted to an enumeration problem. The objective function is calculated for each feasible voltage vector and the voltage vector which results in the minimum value of the objective function is selected. This procedure is far simpler than any other optimization algorithm, which has made it the most popular approach in the drives community.

A 2-level voltage source inverter can apply $2^3 = 8$ voltage vectors. If the prediction horizon is one, evaluating 8 finite values for the objective function and finding the minimum is not time consuming. However, the number of finite states increases to $2^{3^2} = 64$, $2^{3^3} = 512$ or $2^{3^4} = 4096$ for a prediction horizon equal to two, three or four. These observations only apply to 2-level converters. The respective figures for a 5-level converter are $5^{3^1} = 125$, $5^{3^2} = 1.5 \times 10^4$, $5^{3^3} = 1.9 \times 10^6$ and $5^{3^4} = 2.4 \times 10^8$. It can be seen that FCS-MPC encounters calculation time issues for long prediction horizons despite its simple concept. Therefore, it can be concluded that enumeration is the simplest way, but not always the easiest.

The machine model (2.3) can be used to develop a set of differential equations for the precalculation of the machine's behavior. Only two out of four machine variables ($\boldsymbol{i}_\mathbf{s}$, $\boldsymbol{i}_\mathbf{r}$, $\boldsymbol{\psi}_\mathbf{s}$ and $\boldsymbol{\psi}_\mathbf{r}$) are state variables. Thus the differential equations can be written with any combination of 2 out

of 4. A common approach is to consider $\boldsymbol{i_s}$ and $\boldsymbol{\psi_r}$ as system variables

$$\frac{d\boldsymbol{i_s}}{dt} = \left(\frac{-R_\mathrm{s}}{\sigma L_\mathrm{s}} - \frac{L_\mathrm{m}^2 R_\mathrm{r}}{\sigma L_\mathrm{s} L_\mathrm{r}^2} - \frac{L_\mathrm{m}}{L_\mathrm{r}} j\omega_\mathrm{e}\right)\boldsymbol{i_s} - \left(\frac{R_\mathrm{r} L_\mathrm{m}}{\sigma L_\mathrm{s} L_\mathrm{r}^2} + j\omega_\mathrm{e}\frac{L_\mathrm{m}^2}{\sigma L_\mathrm{s} L_\mathrm{r}}\right)\boldsymbol{\psi_r} + \frac{1}{\sigma L_\mathrm{s}}\boldsymbol{u}_\mathrm{s}, \tag{3.13a}$$

$$\frac{d\boldsymbol{\psi_r}}{dt} = \left(\frac{R_\mathrm{r} L_\mathrm{m}}{L_\mathrm{r}} - j\omega_\mathrm{e}\sigma L_\mathrm{s}\right)\boldsymbol{i}_\mathrm{s} - \left(\frac{R_\mathrm{r}}{L_\mathrm{r}} + j\omega_\mathrm{e}\frac{L_\mathrm{m}}{L_\mathrm{r}}\right)\boldsymbol{\psi}_\mathrm{r}. \tag{3.13b}$$

In discrete form

$$\begin{aligned}\boldsymbol{i}_\mathrm{s}(k+1) = &\left(1 - \frac{T_\mathrm{s} R_\mathrm{s}}{\sigma L_\mathrm{s}} - \frac{T_\mathrm{s} L_\mathrm{m}^2 R_\mathrm{r}}{\sigma L_\mathrm{s} L_\mathrm{r}^2} - \frac{T_\mathrm{s} L_\mathrm{m}}{L_\mathrm{r}} j\omega_\mathrm{e}\right)\boldsymbol{i_s}(k) \\ &- \left(\frac{T_\mathrm{s} R_\mathrm{r} L_\mathrm{m}}{\sigma L_\mathrm{s} L_\mathrm{r}^2} + j\omega_\mathrm{e}\frac{T_\mathrm{s} L_\mathrm{m}^2}{\sigma L_\mathrm{s} L_\mathrm{r}}\right)\boldsymbol{\psi_r} + \frac{T_\mathrm{s}}{\sigma L_\mathrm{s}}\boldsymbol{u}_\mathrm{s}(k),\end{aligned} \tag{3.14a}$$

$$\boldsymbol{\psi}_\mathrm{r}(k+1) = \left(1 + \frac{T_\mathrm{s} R_\mathrm{r} L_\mathrm{m}}{L_\mathrm{r}} - j\omega_\mathrm{e}\sigma L_\mathrm{s} T_\mathrm{s}\right)\boldsymbol{i}_\mathrm{s} - \left(\frac{T_\mathrm{s} R_\mathrm{r}}{L_\mathrm{r}} + j\omega_\mathrm{e}\frac{T_\mathrm{s} L_\mathrm{m}}{L_\mathrm{r}}\right)\boldsymbol{\psi}_\mathrm{r}, \tag{3.14b}$$

$$T(k+1) = \frac{3}{2}P|\boldsymbol{\psi}_\mathrm{r} \times \boldsymbol{i}_\mathrm{s}|. \tag{3.14c}$$

Another approach is to consider $\boldsymbol{\psi_r}$ and $\boldsymbol{\psi_s}$ as system variables as

$$\frac{d\boldsymbol{\psi_s}}{dt} = \frac{-R_s}{\sigma L_s}\boldsymbol{\psi_s} + \frac{R_s L_m}{\sigma L_s L_r}\boldsymbol{\psi_r} + \boldsymbol{u_s}, \tag{3.15a}$$

$$\frac{d\boldsymbol{\psi_r}}{dt} = \frac{R_r L_m}{\sigma L_s L_r}\boldsymbol{\psi_s} - \frac{R_r}{\sigma L_r}\boldsymbol{\psi_r} + j\omega_e\boldsymbol{\psi_r}\cdot \tag{3.15b}$$

In discrete form

$$\boldsymbol{\psi_s}(k+1) = (1 - \frac{R_s}{\sigma L_s})\boldsymbol{\psi_s}(k) + \frac{R_s L_m}{\sigma L_s L_r}\boldsymbol{\psi_r}(k) + \boldsymbol{u_s}(k+1), \tag{3.16a}$$

$$\boldsymbol{\psi_r}(k+1) = (1 + \frac{R_r L_m}{\sigma L_s L_r})\boldsymbol{\psi_s}(k) - \frac{R_r}{\sigma L_r}\boldsymbol{\psi_r}(k) + j\omega_e\boldsymbol{\psi_r}(k), \tag{3.16b}$$

$$T(k+1) = \frac{3}{2}P|\boldsymbol{\psi_r} \times \boldsymbol{\psi_s}|. \tag{3.16c}$$

The objective function can be formulated for torque control

$$J = (T(k+1) - T^*)^2 + \lambda(|\boldsymbol{\psi_s}| - |\boldsymbol{\psi_s^*}|)^2, \tag{3.17}$$

$$\tag{3.18}$$

or current control

$$J = (\boldsymbol{i_{s\alpha}}(k+1) - \boldsymbol{i_{s\alpha}^*})^2 + (\boldsymbol{i_{s\beta}}(k+1) - \boldsymbol{i_{s\beta}^*})^2, \tag{3.19}$$

where λ is a weighting factor and considered as a tuning parameter.

3.2.3.1 Inclusion of secondary goals in the objective function

In some cases, there is a primary goal or a more important control objective that must be achieved. At the same time, there might be additional constraints or requirements that should also be met. In these cases, the objective function consists of primary and secondary terms, where the importance of the secondary term can vary within a wide range, depending on the application and its specific needs. For example one can include a term in the objective function to reduce the switching frequency.

$$J = (T(k+1) - T^*)^2 + \lambda_1(|\boldsymbol{\psi_s}| - |\boldsymbol{\psi_s^*}|)^2 + \lambda_2 n_{\mathrm{sw}}, \tag{3.20a}$$
$$J = (\boldsymbol{i_{s\alpha}}(k+1) - \boldsymbol{i_{s\alpha}^*})^2 + (\boldsymbol{i_{s\beta}}(k+1) - \boldsymbol{i_{s\beta}^*})^2 + \lambda_2 n_{\mathrm{sw}}, \tag{3.20b}$$

where n_{sw} is the number of switchings and λ_2 is the corresponding weighting factors. The same concept can be used to include common mode voltage, acoustic noise, capacitor voltages of a multilevel converter etc. in the objective function.

3.2.3.2 Weighting Factor Selection

There is no classical approach for setting the weighting factor in an objective function; however, some guidelines can be followed for tuning this parameter [92]:

- If the objective function consists of a single variable or several components of a variable as in (3.19), the weighting factor is usually set to 1.

- If the cost function consists of equally important variables as in (3.17), an initial guess for the weighting factor is equal to 1 considering the variables are in per unit. Afterwards, this initial guess can be adjusted accurately based on several simulations at different operating points.

- If the cost function includes secondary terms such as in (3.20), it is usually preferred to perform several simulations starting from setting the weighting factor of the secondary goal term equal to 0. It is usually the designer's task to decide to what extent the primary goals should be sacrificed for the secondary ones. An increase in the weighting factor λ_2 in equation (3.20), for instance, will lead to a decrease of the switching frequency, and the performance of the reference tracking will deteriorate. Figure 3.7 shows simulation results of applying MPC with an objective function as in (3.20b) to an RL load connected to a 2-level inverter. It can be seen that increasing the switching frequency penalizing factor, λ_2, decreases the switching frequency; however, current distortion increases at the same time. So by setting the value of the weighting factor, a trade-off is made between the switching frequency and current distortion.

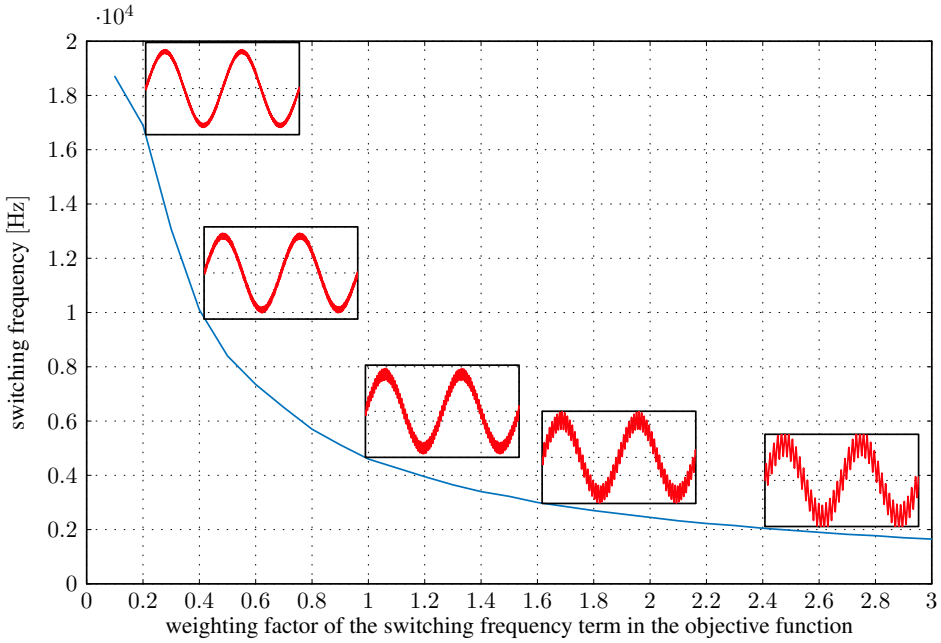

Figure 3.7: Phase current versus weighting factor of the switching frequency term in the objective function

3.2.4 Long prediction horizon MPC

There are mainly three benefits of increasing the prediction horizon: First, for direct MPC, a longer prediction horizon improves the steady state performance in terms of current distortion. Second, for non-minimum phase systems or, in other words, systems with inverse behavior, a long prediction horizon is necessary to assure reference tracking and stable operation during transients. Third, a long prediction horizon reduces the sensitivity to parameters, model mismatch and measurement noise and hence leads to better steady state results. On the other hand, application of long prediction horizon MPC is limited by calculation power limitation. Several techniques which enable long prediction horizon MPC are:

- **MPDxC:** The hysteresis predictive control explained in section 3.2.1 is based on extrapolations of current trajectories within the hysteresis bounds. However, the extrapolation is done only once for each voltage vector of the converter. An improved version utilizing multi-step extrapolations was proposed in [93]. The interesting fact about this method is that hysteresis bands are not only used to bound control variables, but also as a mean of candidate rejection to limit the number of feasible candidates for precalculations. This scheme is developed for direct torque control in [63], direct current control in [94, 95], direct power control in [96] and capacitor voltage balancing in [97].

- **Heuristic FCS-MPC:** As stated before, the computational burden of FCS-MPC increases exponentially with the prediction horizon. In [98], a candidate rejection technique is used to increase the prediction horizon. It is based on the idea that if the reference voltage vector is available, it is possible to enumerate the objective function only for the voltage vectors closest to the reference vector. This decreases the feasible finite states to 3. For

instance, for a 2-level converter and a prediction horizon of 5, the number of cases that shall be evaluated decrease from 2^{3^5} to 3^5. A main advantage of this method is that the number of finite states is always equal to 3^{n_p} regardless of the voltage levels of the converter, where n_p is the prediction horizon,

- **Sphere decoding for linear quadratic problems:** In case of a linear system with a quadratic objective function, there is a classical approach for getting the unconstrained solution. A modified technique similar to linear quadratic regulators (LQR) is used in [60–62] to obtain this unconstrained solution. Then the algorithm iteratively considers candidate sequences that belong to a sphere radius centered in the unconstrained solution and chooses the one that minimizes the objective function. This leads to long prediction horizons of upto 10 steps. However, its application is limited to linear systems with quadratic cost functions.

CHAPTER 4

Sychronous optimal modulation

In PWM and SVM, pulses are positioned within a fixed clock cycle. This concept forces the converter to switch at each clock cycle and hence, distributes the switching actions according to the clock interval. The constraint of equally distributing the switchings within the fundamental period is introduced by the modulator and it is not a physical limitation.

The switching frequency of the converter determines the number of permissible switchings per fundamental period. Besides, the controller demands a certain output voltage or modulation index. Switching frequency and modulation index are the only elements that need to be considered in designing a modulator. Therefore, one can omit the concept of clocking the pulses and calculate the switching angles in order to achieve a secondary goal such as optimal current distortion, elimination of certain harmonics, torque ripple optimization etc. In this case, switching events are allowed to take place freely over the fundamental period, with the constraint of maintaining waveform symmetry. An approach with such characteristics is known as Synchronous Optimal Modulation (SOM) or Optimal Pulse Pattern (OPP) technique.

Optimal pulse patterns are not only known for their low current distortion in the electrical drives community, but also for the problems associated with running the optimization process and applying it to a real machine. A major problem is the very slow calculation process. It gets even slower for multi-level converters because the calculation time increases exponentially with the number of voltage levels of the converter. Here, it is shown that it is possible to immensely accelerate the optimization procedure by reformulating the optimization problem. Moreover, it is demonstrated that there is a unique voltage vector sequence at each operating point of the machine that leads to less current harmonic distortion.

This chapter introduces OPPs for 5-level converters, proceeds with algorithms to calculate these patterns and concludes with their application to electrical drives and the application of voltage vector sequences to MPC based current distortion optimization is discussed in the next chapter.

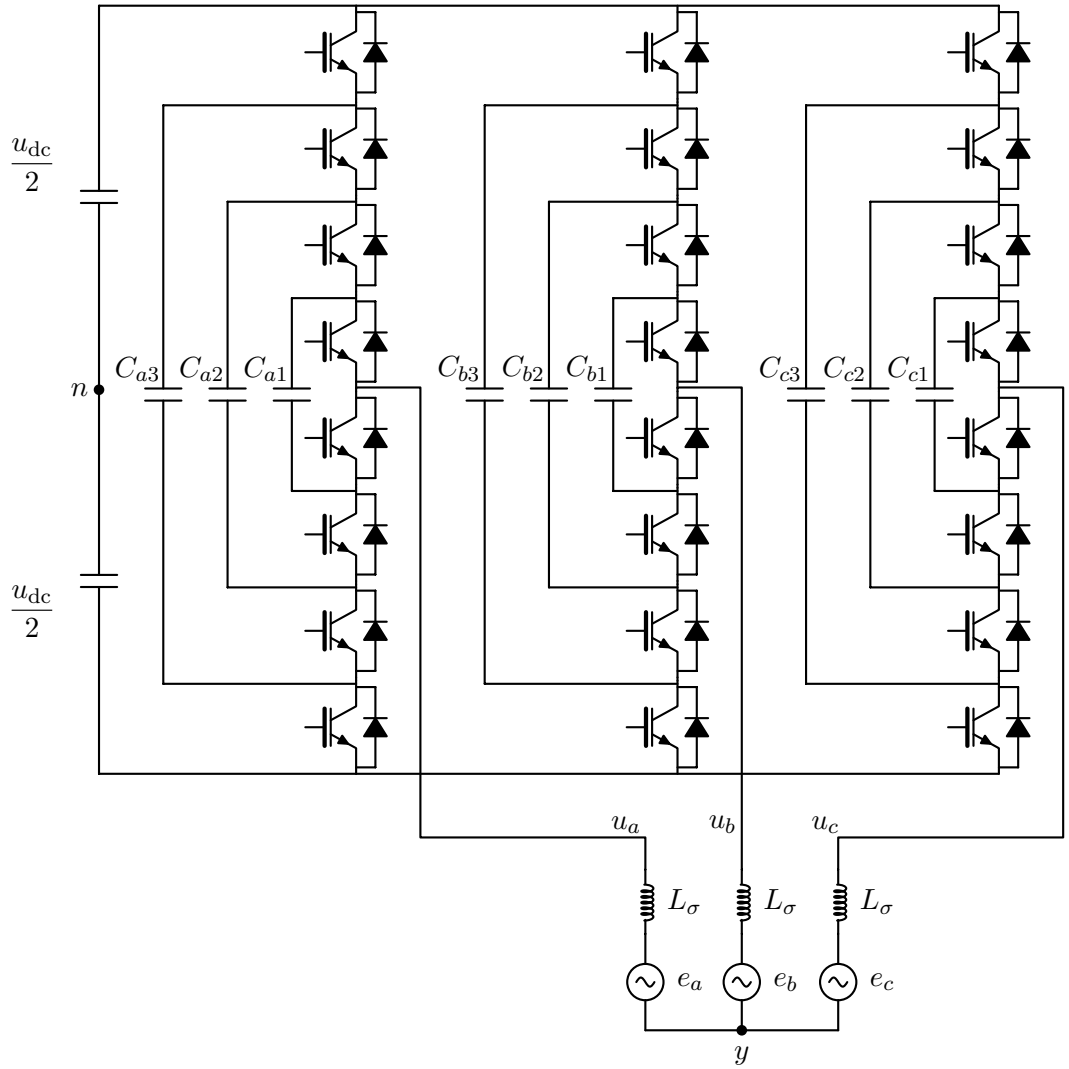

Figure 4.1: 5L-FC converter connected to an inductive load with a sinusoidal back EMF

4.1 5-level voltage waveform

A 5L-FC converter connected to an inductive load with a sinusoidal back EMF is shown in Figure 4.1. The phase voltages of the converter, $u_a = u_{an}$, $u_b = u_{bn}$ and $u_c = u_{cn}$, can be calculated based on the flying capacitor voltages and switching states (2.10). However, it is also necessary to calculate the load-side phase voltages u_{ay}, u_{by} and u_{cy} in order to determine the load currents. For this purpose, we define u_{yn} to be the voltage between the load side neutral point and the DC-link midpoint

$$u_{yn}(t) = \frac{1}{3}(u_a(t) + u_b(t) + u_c(t)). \tag{4.1}$$

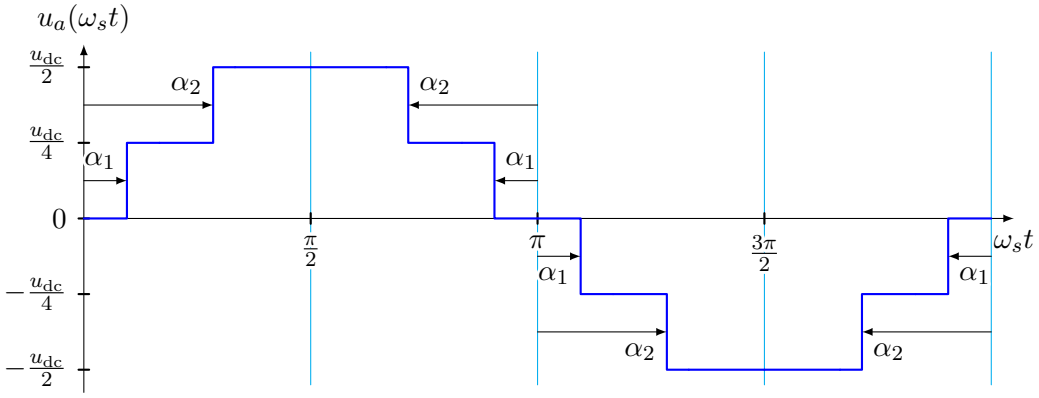

Figure 4.2: Three-phase voltages of a 5-level inverter

Thus, the load side phase voltages can be expressed as

$$u_{ay}(t) = u_a(t) - u_{yn}(t) = \frac{2}{3}u_a(t) - \frac{1}{3}(u_b(t) + u_c(t)), \tag{4.2a}$$

$$u_{by}(t) = u_b(t) - u_{yn}(t) = \frac{2}{3}u_b(t) - \frac{1}{3}(u_a(t) + u_c(t)), \tag{4.2b}$$

$$u_{cy}(t) = u_c(t) - u_{yn}(t) = \frac{2}{3}u_c(t) - \frac{1}{3}(u_a(t) + u_b(t)). \tag{4.2c}$$

The primary goal of pulse patterns is to emulate a symmetrical, sinusoidal three-phase voltage system with variable frequency and amplitude on the load phases. To achieve this, the voltage waveform is considered to have the following properties

(C_1) pulse patterns are periodic with period $T_1 = \frac{2\pi}{\omega_s}$, i.e. $u_a(t + T_1) = u_a(t)$,

(C_2) identical pulse patterns are used for all three inverter legs,

(C_3) the phase shift between patterns from one leg to the next is $\frac{2\pi}{3} \equiv 120°$,
i.e. $u_b(t) = u_a\left(t - \frac{1}{\omega_s}\frac{2\pi}{3}\right)$ and $u_c(t) = u_a\left(t + \frac{1}{\omega_s}\frac{2\pi}{3}\right)$,

(C_4) $u_a(t)$ has half-wave and odd quarter-wave symmetry,
i.e. $u_a(t) = -u_a(t - \frac{1}{\omega_s}\pi)$ and $u_a(t) = u_a(\frac{1}{\omega_s}\pi - t)$,

(C_5) p commutations occur at $\omega_s t \in \{\alpha_1, \alpha_2, \ldots \alpha_p\}$ with commutation angles $0 < \alpha_1 < \alpha_2 < \ldots < \alpha_p < \frac{\pi}{2}$ within the first quarter of each period of $u_a(t)$.

A 5-level voltage waveform that satisfies these conditions is shown in Figure 4.2. Based on the three-phase and quarter-waveform symmetries, calculations can be done for a quarter of a single phase waveform and results can be extended to the whole period and the three phases.

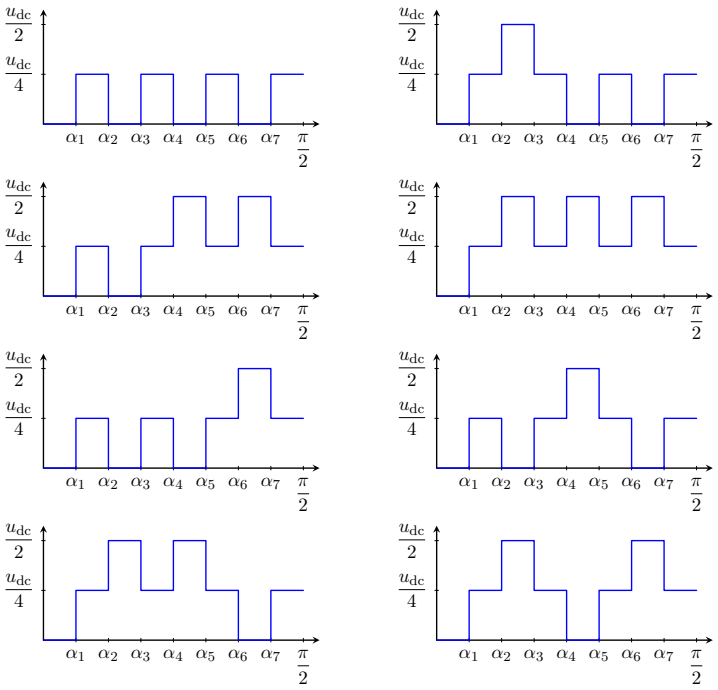

Figure 4.3: Pulse pattern structures of a 5-level inverter for $p = 7$

4.1.1 Voltage waveform structures

Assume a pulse pattern with p switchings in a quarter of a waveform period. Considering the fact that the voltage level is zero at the starting point and only a single level transition is allowed at each switching, $2^{\lfloor p/2 \rfloor}$ different voltage waveforms can be generated for each pulse number p. For instance, and as it is depicted in Figure 4.3, $2^{\lfloor 7/2 \rfloor} = 8$ voltage waveforms exist for $p = 7$ switchings per quarter of a period. Each of these unique voltage waveforms is called a voltage structure. A voltage level matrix $\boldsymbol{L}$ is introduced to describe all voltage structures for a certain pulse number p. Each row of this matrix represents voltage levels of a voltage structure. For example, the voltage level matrix for $p = 7$ is

$$\mathbf{L} = \begin{bmatrix} 0 & 1 & 0 & 1 & 0 & 1 & 0 & 1 \\ 0 & 1 & 2 & 1 & 0 & 1 & 0 & 1 \\ 0 & 1 & 0 & 1 & 2 & 1 & 2 & 1 \\ 0 & 1 & 2 & 1 & 2 & 1 & 2 & 1 \\ 0 & 1 & 0 & 1 & 0 & 1 & 2 & 1 \\ 0 & 1 & 0 & 1 & 2 & 1 & 0 & 1 \\ 0 & 1 & 2 & 1 & 2 & 1 & 0 & 1 \\ 0 & 1 & 2 & 1 & 0 & 1 & 2 & 1 \end{bmatrix}. \tag{4.3}$$

4.1.2 Fundamentals and harmonics of inverter leg voltages

The periodic inverter leg voltages $u_a(t)$, $u_b(t)$ and $u_c(t)$ can be written as their Fourier series representations

$$u_a(t) = \sum_{k=1}^{\infty} u_{a,k} \cdot \sin\left(k\omega_s t\right), \tag{4.4a}$$

$$u_b(t) = \sum_{k=1}^{\infty} u_{a,k} \cdot \sin\left(k\left(\omega_s t - \frac{2\pi}{3}\right)\right), \tag{4.4b}$$

$$u_c(t) = \sum_{k=1}^{\infty} u_{a,k} \cdot \sin\left(k\left(\omega_s t + \frac{2\pi}{3}\right)\right). \tag{4.4c}$$

In equation (4.4), the k-th harmonic has an amplitude of $u_{a,k}$. Amplitudes are the same for all three phases because of three-phase symmetry - property (C_2). A fixed phase shift between switching patterns is already incorporated - property (C_3). Finally, there are no cosine-coefficients in the Fourier series because of the odd waveform symmetry - property (C_4).

When (4.4) is inserted into (4.2), it yields

$$\begin{aligned}
u_{ay}(t) &= \frac{2}{3}u_a(t) - \frac{1}{3}\left(u_b(t) + u_c(t)\right) \\
&= +\frac{2}{3}\sum_{k=0}^{\infty} u_{a,k} \cdot \sin\left(k\omega_s t\right) \\
&\quad -\frac{1}{3}\sum_{k=0}^{\infty} u_{a,k} \cdot \sin\left(k\left(\omega_s t - \frac{2\pi}{3}\right)\right) \\
&\quad -\frac{1}{3}\sum_{k=0}^{\infty} u_{a,k} \cdot \sin\left(k\left(\omega_s t + \frac{2\pi}{3}\right)\right) \\
&= \frac{1}{3}\sum_{k=1}^{\infty} u_{a,k} \cdot \left(2\sin\left(k\omega_s t\right) - \sin\left(k\left(\omega_s t - \frac{2\pi}{3}\right)\right) - \sin\left(k\left(\omega_s t + \frac{2\pi}{3}\right)\right)\right) \\
&= \frac{1}{3}\sum_{k=1}^{\infty} u_{a,k} \cdot 4\left(\sin\left(\frac{k\pi}{3}\right)\right)^2 \cdot \sin\left(k\omega_s t\right).
\end{aligned}$$

The expression within the sum can be further simplified,

$$4\left(\sin\left(\frac{k\pi}{3}\right)\right)^2 = \begin{cases} 3\,, & k \neq 3n,\ n \in \mathbb{N} \\ 0\,, & k = 3n,\ n \in \mathbb{N} \end{cases}$$

leading to the Fourier series representation of $u_{ay}(t)$

$$\left.\begin{aligned} u_{ay}(t) &= \sum_{k=1}^{\infty} u_{ay,k} \cdot \sin\left(k\omega_s t\right), \\ u_{ay,k} &= \begin{cases} u_{a,k}\,, & k \neq 3n,\ n \in \mathbb{N} \\ 0\,, & k = 3n,\ n \in \mathbb{N} \end{cases} \end{aligned}\right\} \tag{4.5}$$

The same sequence of steps can be repeated for $u_{by,k}$ and $u_{cy,k}$.

Equation (4.5) shows two fundamental properties of the relation between inverter leg voltages and load phase voltages

1. All harmonics of order $k = 3n$, $n \in \mathbb{N}$, ("triplen harmonics") of inverter leg voltages disappear in machine phase voltages.

2. All other harmonics ("non-triplen harmonics") have the same amplitude for inverter leg voltages and machine phase voltages. Hence, it would be acceptable to consider the converter voltages for calculations and extend the results to the load voltage.

Now the Fourier coefficients of inverter leg voltage $u_a(t)$ and thus all other leg and load voltages can be derived from commutation angles. For this purpose, we introduce two additional, fixed angles $\alpha_0 = 0$ and $\alpha_{p+1} = \frac{\pi}{2}$. The half-wave symmetry in the property (C_4) leads to the cancellation of all harmonics of even order.

For odd k, the Fourier coefficients are

$$
\begin{aligned}
u_{a,k} &= \frac{8}{T_1} \int_0^{\frac{T_1}{4}} u_a(t) \cdot \sin\left(k \frac{2\pi}{T_1} t\right) \mathrm{dt} \\
&= \frac{8}{T_1} \sum_{i=0}^{p} \left(\int_{\alpha_i \frac{T_1}{2\pi}}^{\alpha_{i+1} \frac{T_1}{2\pi}} l\left(i\right) \cdot \frac{u_{\mathrm{dc}}}{2} \sin\left(k \frac{2\pi}{T_1} t\right) \mathrm{dt} \right) \\
&= \frac{4u_{\mathrm{dc}}}{T_1} \sum_{i=0}^{p} \left(l\left(i\right) \cdot \left[-\frac{T_1}{2k\pi} \cdot \cos\left(k \frac{2\pi}{T_1} t\right) \right] \Bigg|_{t=\alpha_i \frac{T_1}{2\pi}}^{\alpha_{i+1} \frac{T_1}{2\pi}} \right) \\
&= \frac{2u_{\mathrm{dc}}}{k\pi} \sum_{i=0}^{p} \left(l\left(i\right) \cdot \left(\cos\left(k\alpha_i\right) - \cos\left(k\alpha_{i+1}\right) \right) \right) \\
&= \frac{2u_{\mathrm{dc}}}{k\pi} \left(l\left(0\right) \cdot \cos\left(k\alpha_0\right) - l\left(0\right) \cdot \cos\left(k\alpha_1\right) + l\left(1\right) \cdot \cos\left(k\alpha_1\right) - l\left(1\right) \cdot \cos\left(k\alpha_2\right) + \cdots \right) \\
&= \frac{2u_{\mathrm{dc}}}{k\pi} \left(\underbrace{\left(l(1) - l(0)\right)}_{s(1)} \cdot \cos\left(k\alpha_1\right) + \underbrace{\left(l(2) - l(1)\right)}_{s(2)} \cdot \cos\left(k\alpha_2\right) \cdots \underbrace{\left(l(p) - l(p-1)\right)}_{s(p)} \cdot \cos\left(k\alpha_p\right) \right),
\end{aligned}
$$

where $l(i)$ represents the voltage structure with i equal to the corresponding row of the voltage level matrix $\boldsymbol{L}$, and $s(i)$ is equal to 1 during a transition to a higher voltage level and equal to -1 during a transition to a lower voltage level. It is also important to notice that $\alpha_p = \frac{\pi}{2}$ yield $\cos\left(\alpha_p\right) = 0$. Besides, $l(0) = 0$.

Finally, Fourier coefficients $u_{a,k}$ are obtained

$$
u_{a,k} = \frac{2u_d}{k\pi} \sum_{i=1}^{p} s(i) \cos\left(k\alpha_i\right). \tag{4.6}
$$

Equation (4.6) represents the fundamental and harmonics of the converter's voltage based on the switching angles α_i. The fundamental amplitude can be found by setting $k = 1$ in (4.6)

$$u_{a,1} = \frac{2u_d}{\pi} \sum_{i=1}^{p} s(i) \cos(\alpha_i). \tag{4.7}$$

4.1.2.1 Modulation index

Equation (4.7) is used to define the converter's modulation index based on switching angles. The modulation index m is defined as

$$m = \frac{u_{a,1}}{\frac{u_{\mathrm{dc}}}{2}} = \frac{u_{la,1}}{\frac{u_{\mathrm{dc}}}{2}}. \tag{4.8}$$

Using equation (4.7) and (4.8), the modulation index for a given pulse pattern is

$$m = \frac{4}{\pi} \sum_{i=1}^{p} s(i) \cos(\alpha_i). \tag{4.9}$$

The maximum value of the modulation index m is reached when the converter is operating in six-step mode. In six-step mode, the converter generates a square pulse with an amplitude of $\frac{u_{\mathrm{dc}}}{2}$ and $p = 0$. Hence, the maximum value of the modulation index or, in other words, the modulation index of six-step mode can be found by setting $p = 0$ in (4.10)

$$m_{max} = \frac{4}{\pi} \approx 1.273. \tag{4.10}$$

Remark: Some publications define the modulation index $m = \frac{u_{a,1}}{u_{a,1,\text{six-step}}}$ based on the fundamental amplitude $u_{a,1,\text{six-step}}$ of six-step mode [99]. In this case, the maximum value of the modulation index will be 1.

4.1.2.2 The considered of harmonics

Equation (4.6) gives the amplitude of all harmonics of a pulse pattern. In practice, it is not possible to consider an infinite number of harmonics to analyze a voltage waveform. As a result, harmonics that are considered in calculation and optimization need to be limited to a certain number. Based on symmetries and according to (4.5), only odd and non-triplen harmonics exist in the load voltage. So the harmonic orders that are considered are: $\boldsymbol{H} = \{k \in \mathbb{N} \mid k > 1 \wedge k \notin \{2n, 3n\} \, \forall n \in \mathbb{N}\} = \{5, 7, 11, 13, 17, 19, \ldots\}$. In this work, these harmonics are considered up to harmonic order of 101. To ensure that harmonic orders up to 101 are enough to represent the pulse pattern, a voltage waveform with $p = 9$ is considered and its harmonic orders are calculated. Afterwards, the pulse pattern is regenerated with harmonic orders up to 101 via a reverse Fourier transformation. The resultant waveform can be seen in Figure 4.4.

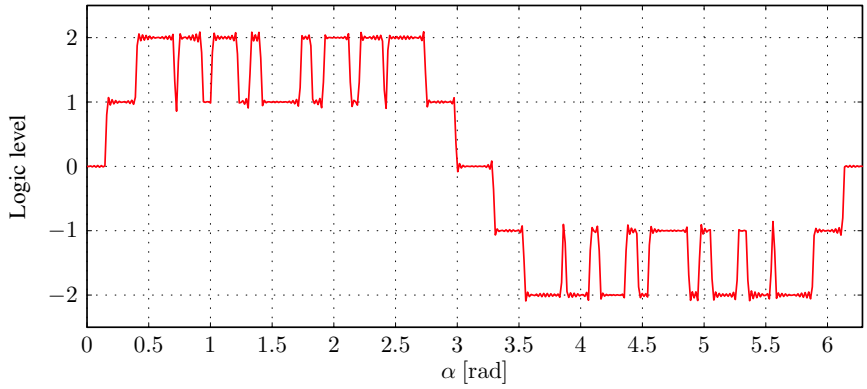

Figure 4.4: Reverse Fourier transformation of a pulse pattern considering the first 101 harmonics

4.1.2.3 Visualization of harmonic content

It is useful to visualize harmonic contents of pulse patterns as a function of switching angles. There are two switching angles for $p = 2$: α_1 and α_2. The fundamental component of inverter leg voltage as a function of switching angles can be derived from equation (4.7)

$$u_{a,1} = \frac{2u_{\mathrm{dc}}}{\pi}(\cos(\alpha_1) + \cos(\alpha_2)). \tag{4.11}$$

The 5^{th}, 7^{th}, 11^{th} and 13^{th} harmonics for $p = 2$ can also be derived from (4.6) in a similar way

$$u_{a,5} = \frac{2u_{\mathrm{dc}}}{5\pi}(\cos(5\alpha_1) + \cos(5\alpha_2)), \tag{4.12a}$$

$$u_{a,7} = \frac{2u_{\mathrm{dc}}}{7\pi}(\cos(7\alpha_1) + \cos(7\alpha_2)), \tag{4.12b}$$

$$u_{a,11} = \frac{2u_{\mathrm{dc}}}{11\pi}(\cos(11\alpha_1) + \cos(11\alpha_2)), \tag{4.12c}$$

$$u_{a,13} = \frac{2u_{\mathrm{dc}}}{13\pi}(\cos(13\alpha_1) + \cos(13\alpha_2)). \tag{4.12d}$$

The two commutation angles α_1 and α_2 are varied within their feasible bounds and the resultant fundamental component is plotted in Figure 4.5. The same concept is applied to plot the 5^{th}, 7^{th}, 11^{th} and 13^{th} harmonic and the results are shown in the Figures 4.6 to 4.9. It is not possible to plot these functions for $p > 2$ due to the multidimensionality of the problem. However, this single case gives a useful insight into the dependency of fundamental and harmonic components of a signal on the switching angles.

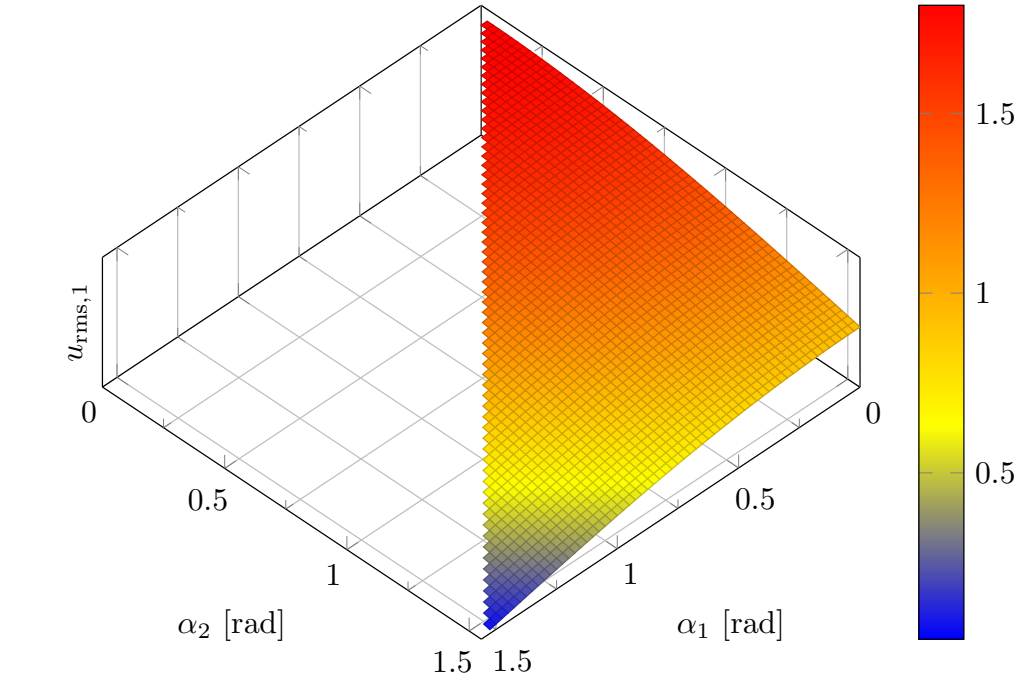

Figure 4.5: Normalized RMS value of the fundamental component for $p = 2$

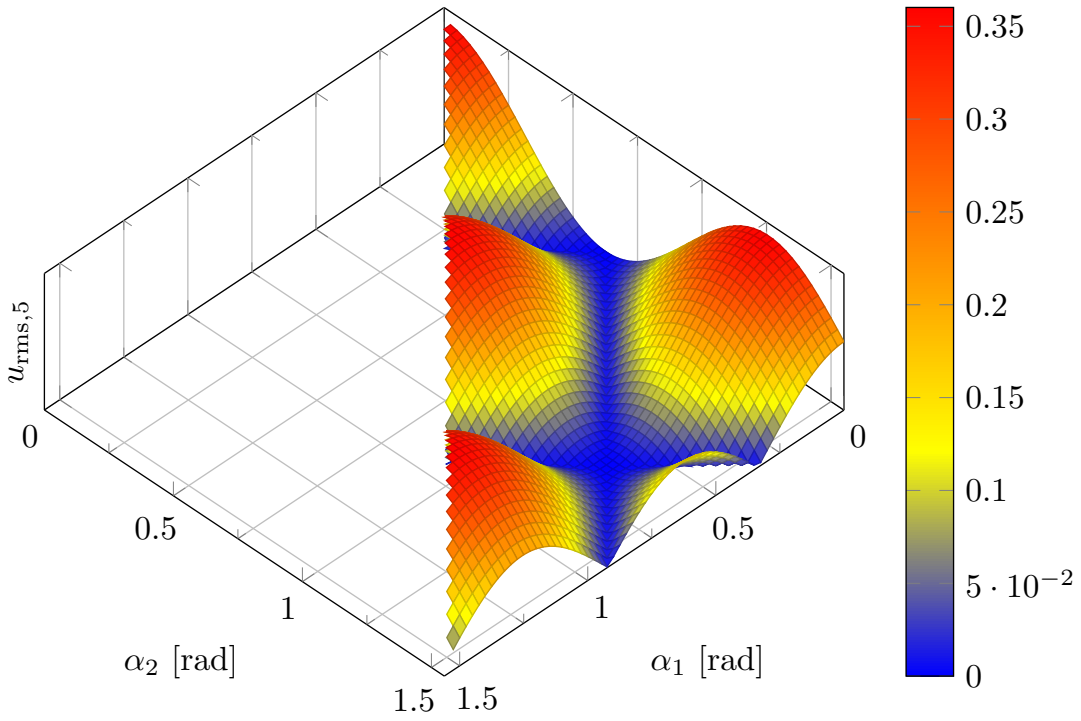

Figure 4.6: Normalized RMS value of the 5^{th} harmonic for $p = 2$

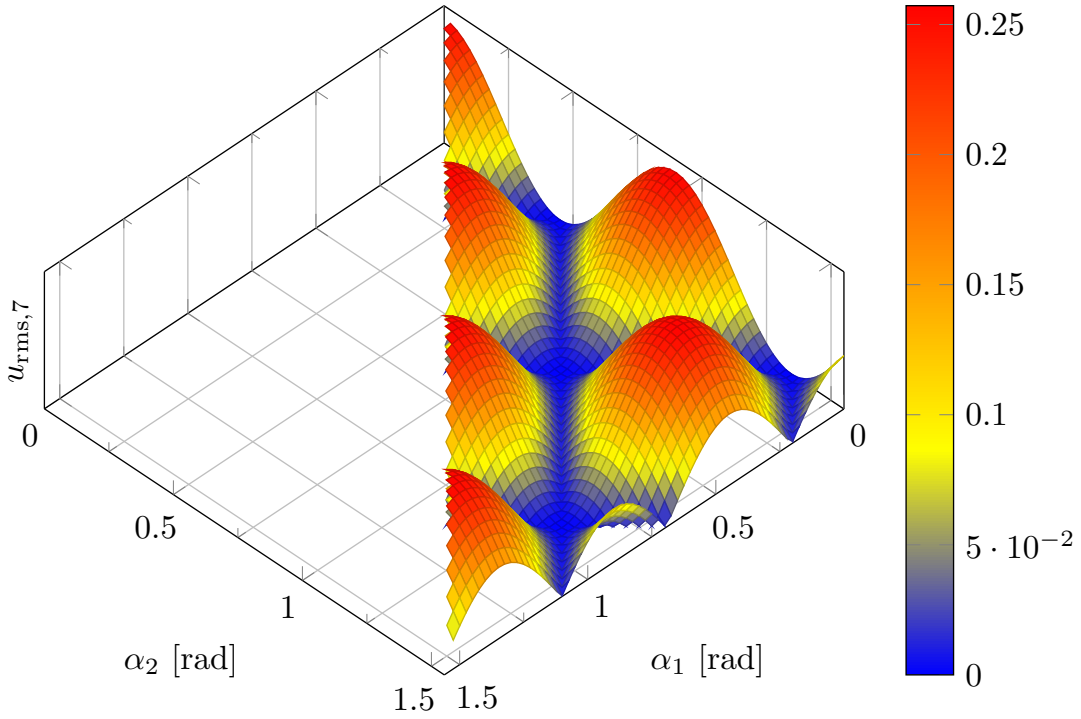

Figure 4.7: Normalized RMS value of the 7^{th} harmonic for $p = 2$

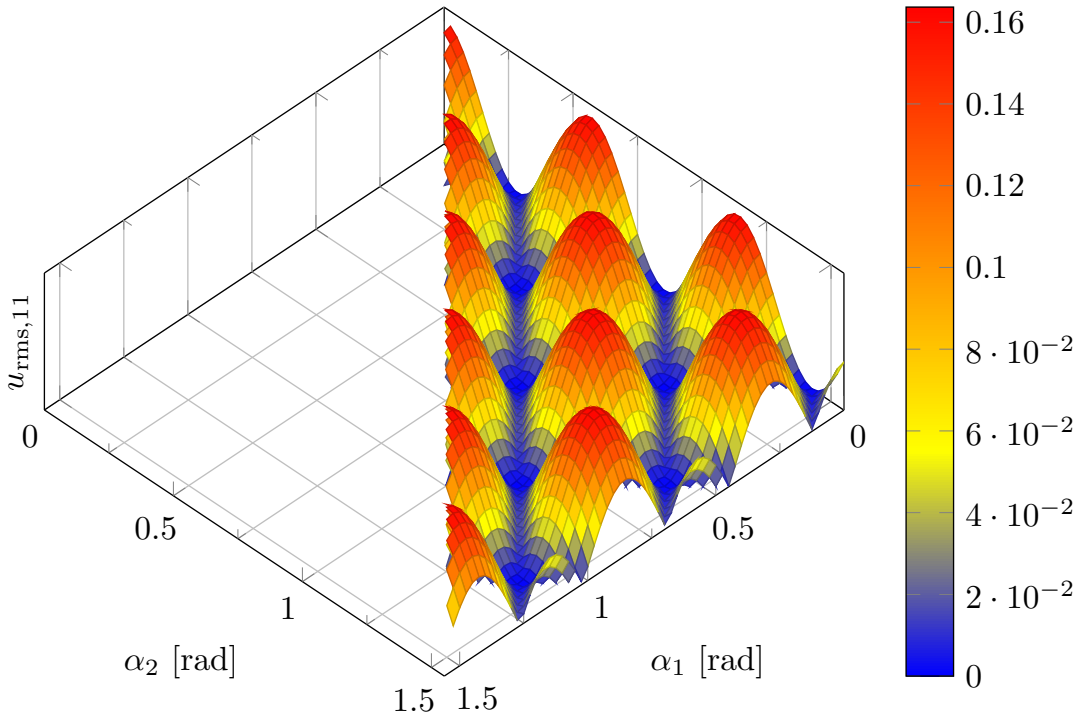

Figure 4.8: Normalized RMS value of the 11^{th} harmonic for $p = 2$

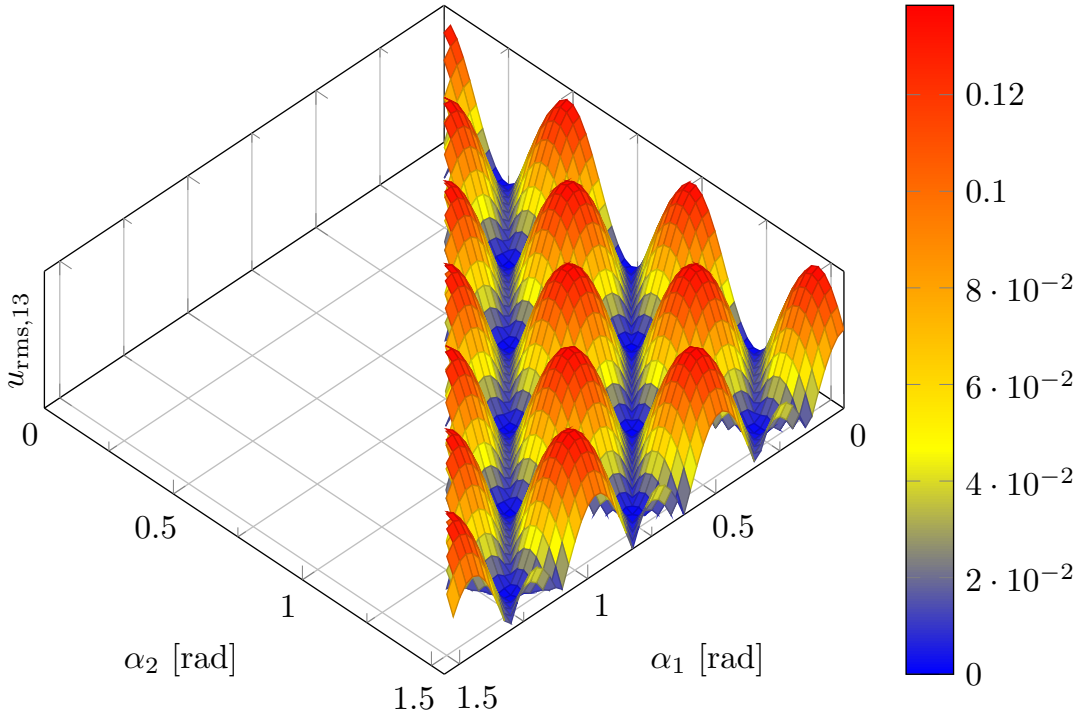

Figure 4.9: Normalized RMS value of the 13^{th} harmonic for $p = 2$

4.2 Current distortion

An optimal pulse pattern should transfer a maximum of real power from the inverter to the load. As a result, any components of the load side phase voltages that do not contribute to this, but produces losses, should be minimized. The instantaneous phase power of an inductive load L_σ with a back EMF e_a is

$$p_a(t) = u_{aY}(t) \cdot i_a(t) = \left(L_\sigma \frac{\mathrm{di_a(t)}}{\mathrm{dt}} + e_a(t) \right) \cdot i_a(t) = L_\sigma \frac{\mathrm{di_a(t)}}{\mathrm{dt}} i_a(t) + e_a(t) \cdot i_a(t)\,. \quad (4.13)$$

Given a phase voltage $u_{la}(t)$ from (4.5), the load current $i_a(t)$ can be written as a Fourier series

$$i_a(t) = \sum_{k=1}^{\infty} i_{a,k} \cdot \sin\left(k\omega_\mathrm{s} t + \varphi_{i,k}\right), \quad (4.14)$$

with harmonic orders $k \in \mathbb{N}_{>0}$, corresponding amplitudes $i_{a,k}$ and phase shifts $\varphi_{i,k}$.

By assuming a sinusoidal EMF, the the induced voltage $e_a(t)$ consists only of a fundamental component.

$$e_a(t) = e_i \cdot \sin\left(\omega_\mathrm{s} t + \varphi_{ei}\right) \quad (4.15)$$

Replacing $i_a(t)$ and $e_a(t)$ in (4.13) results in

$$p_a(t) = \left(L_\sigma \cdot \sum_{k=1}^{\infty} i_{a,k} \cdot \cos\left(k\omega_\mathrm{s} t + \varphi_{i,k}\right) \cdot \frac{1}{k\omega_\mathrm{s}} + e_i \cdot \sin\left(\omega_\mathrm{s} t + \varphi_{ei}\right) \right) \tag{4.16}$$

$$\cdot \sum_{k=1}^{\infty} i_{a,k} \cdot \sin\left(k\omega_\mathrm{s} t + \varphi_{i,k}\right). \tag{4.17}$$

The real load phase power P_a is the time average of the instantaneous phase power $p_a(t)$

$$\begin{aligned} P_a &= \frac{1}{T_1} \int_0^{T_1} p_a(t)\,\mathrm{dt} \\ &= \frac{1}{T_1} \int_0^{T_1} \left(L_\sigma \cdot \sum_{k=1}^{\infty} i_{a,k} \cdot \cos\left(k\omega_\mathrm{s} t + \varphi_{i,k}\right) \cdot \frac{1}{k\omega_\mathrm{s}} + e_i \cdot \sin\left(\omega_\mathrm{s} t + \varphi_{ei}\right) \right) \\ &\qquad \cdot \sum_{k=1}^{\infty} i_{a,k} \cdot \sin\left(k\omega_\mathrm{s} t + \varphi_{i,k}\right) \mathrm{dt}\,. \end{aligned} \tag{4.18}$$

Note the following for an integral over the full period of the product of two sinusoidal functions

$$\int_0^{T_1} \cos\left(k_1\omega_\mathrm{s} t + \varphi_{k1}\right) \cdot \sin\left(k_2\omega_\mathrm{s} t + \varphi_{k2}\right) \mathrm{dt} = \begin{cases} -\frac{\pi}{\omega_\mathrm{s}} \cdot \sin\left(\varphi_{k1} - \varphi_{k2}\right), & k_1 = k_2, \\ 0\,, & k_1 \neq k_2. \end{cases} \tag{4.19}$$

For $k_1 \neq k_2$ (mixed frequency terms), the contribution to real power is zero. For $k_1 = k_2 = k$, $\varphi_{k1} = \varphi_{k2}$ and $\sin\left(\varphi_{k1} - \varphi_{k2}\right) = 0$. Thus, a first simplification of (4.18) is

$$P_a = \frac{1}{T_1} \int_0^{T_1} e_i \cdot \sin\left(\omega_\mathrm{s} t + \varphi_{ei}\right) \cdot \sum_{k=1}^{\infty} i_{a,k} \cdot \sin\left(k\omega_\mathrm{s} t + \varphi_{i,k}\right) \mathrm{dt}\,. \tag{4.20}$$

Again, mixed frequency terms do not contribute to the integral, and a further simplification in equation (4.20) yields

$$P_a = \frac{1}{2} \cdot e_i \cdot i_{a,1} \cdot \cos\left(\varphi_{ei} - \varphi_{i,1}\right). \tag{4.21}$$

As a result, only fundamental load current results in real power. Any current harmonic with $k > 1$ is thus to be minimized to optimize the pulse pattern.

Amplitudes $i_{a,k}$ of load current harmonics depend on the load phase voltage as well as on the load impedance. By assuming a linear inductive load, $i_{a,k}$ can be calculated separately for

each harmonic order k. For harmonics $i_{a,k}$ with $k > 1$, e_a is short-circuited because $e_a(t)$ was assumed to be sinusoidal with fundamental speed ω_s. This results in

$$i_{a,k} = \frac{1}{k\omega_\mathrm{s} L_\sigma} \cdot u_{la,k}\,, \quad \forall k > 1\,. \tag{4.22}$$

$u_{ay,k}$ is known from (4.5) to be $u_{a,k}$ for non-triplen harmonics and zero for triplen harmonics. To sum up

$$i_{a,k} = \begin{cases} \frac{1}{k\omega_\mathrm{s} L_\sigma} \cdot u_{a,k}\,, & k \neq 3n,\ n \in \mathbb{N},\ k > 1\,, \\ 0\,, & k = 3n,\ n \in \mathbb{N}. \end{cases} \tag{4.23}$$

Furthermore, $u_{a,k}$ is zero for all harmonics of even order because of half-wave symmetry - property (C_4). This results in a reduced set of inverter leg voltage harmonics that are able to produce currents on the load side.

Note that the load is considered to contain no resistive part. This assumption is made to ease the calculation of harmonic current amplitudes with a strongly inductive load. As a consequence, harmonic currents do not lead to any losses at all in this particular load model. However, when a small resistance R is connected in series to L_σ, a resistive loss term appears in (4.18). Instantaneous losses produced by the current $i_a(t)$ in a resistor R are

$$p_{R,a}(t) = R \cdot (i_a(t))^2\,, \tag{4.24}$$

and the corresponding real power is

$$P_{R,a} = \frac{1}{T_1}\int_0^{T_1} p_{R,a}(t)\,\mathrm{dt} = \frac{1}{T_1}\int_0^{T_1} R \cdot (i_a(t))^2\,\mathrm{dt} = R \cdot \frac{1}{T_1}\int_0^{T_1} (i_a(t))^2\,\mathrm{dt}. \tag{4.25}$$

Besides, the RMS value of $i_a(t)$ is

$$I_{a,rms} = \sqrt{\frac{1}{T_1}\int_0^{T_1} (i_a(t))^2\,\mathrm{dt}}, \tag{4.26}$$

which can be used to evaluate losses

$$P_{R,a} = R \cdot (I_{a,rms})^2\,. \tag{4.27}$$

By applying Parseval's theorem, $I_{a,rms}$ can be calculated from the Fourier coefficients $i_{a,k}$ as well

$$I_{a,rms} = \sqrt{\sum_{k=1}^{\infty} \left(\frac{i_{a,k}}{\sqrt{2}}\right)^2}. \tag{4.28}$$

As mentioned in (4.1.2.2), only current harmonics from the harmonic array $\boldsymbol{H}$ are considered. Hence

$$I_{a,H} = \sqrt{\sum_{k\in H}\left(\frac{i_{a,k}}{\sqrt{2}}\right)^2}\,. \tag{4.29}$$

Using (4.23), $I_{a,H}$ can be calculated from the Fourier coefficients $u_{a,k}$ of inverter leg voltage $u_a(t)$

$$\begin{aligned} I_{a,H} &= \sqrt{\sum_{k\in H}\left(\frac{1}{\sqrt{2}k\omega_\mathrm{s}L_\sigma}\cdot u_{a,k}\right)^2} = \\ &= \sqrt{\sum_{k\in H}\left(\frac{1}{\sqrt{2}k\omega_\mathrm{s}L_\sigma}\frac{2u_d}{k\pi}\sum_{i=1}^{p}s(i)\cos\left(k\alpha_i\right)\right)^2} = \\ &= \frac{\sqrt{2}u_d}{\omega_\mathrm{s}L_\sigma\pi}\sqrt{\sum_{k\in H}\frac{1}{k^4}\left(\sum_{i=1}^{p}s(i)\cos\left(k\alpha_i\right)\right)^2}\,. \end{aligned} \tag{4.30}$$

Equation (4.30) shows the advantage of the assumptions introduced in this chapter and gives an analytical solution to calculating the RMS values of current harmonics from switching angles of a given pulse pattern.

The harmonic distortion of a pulse pattern d is defined as

$$d = \frac{I_{a,H}}{I_{a,H,\text{six-step}}}\,, \tag{4.31}$$

where $I_{a,H,\text{six-step}}$ is the RMS value of load current harmonics $k \in \boldsymbol{H}$ in six-step mode. $I_{a,H,\text{six-step}}$ can be calculated using (4.30) with $p = 0$

$$I_{a,H,\text{six-step}} = \frac{\sqrt{2}u_d}{\omega_\mathrm{s}L_\sigma\pi}\sqrt{\sum_{k\in H}\frac{1}{k^4}}\,. \tag{4.32}$$

Inserting (4.30) and (4.32) into (4.31) yields

$$d = \sqrt{\frac{\sum\limits_{k\in H}\frac{1}{k^4}\left(\sum\limits_{i=1}^{p}s(i)\cos\left(k\alpha_i\right)\right)^2}{\sum\limits_{k\in H}\frac{1}{k^4}}}\,. \tag{4.33}$$

In (4.33), distortion d does not depend on model parameters, it is only a function of commutation angles α. Thus it can be used in the optimization process to quantify the performance of a pulse pattern with a single number, based on the losses caused by harmonic load currents, without

involving parameters of the inverter or load. Additionally, it is important to note that the value of the distortion function plays no role in the optimization procedure; though the location of its minimum defines the optimal switching angles and the optimal pulse pattern. As a result, constant values and the square root in equation (4.33) can be neglected in the optimization procedure and the objective function can be considered as

$$J_d = \sum_{k \in H} \frac{1}{k^4} \left(\sum_{i=1}^{p} s(i) \cos\left(k\alpha_i\right) \right)^2 . \tag{4.34}$$

In order to get an impression of the objective function J_d, it is plotted as a function of commutation angles for $p = 2$ pulse numbers in Figure 4.10. As can be seen, the objective function is a non-convex function, which means that it has several local minima. This needs to be considered in choosing an optimization technique.

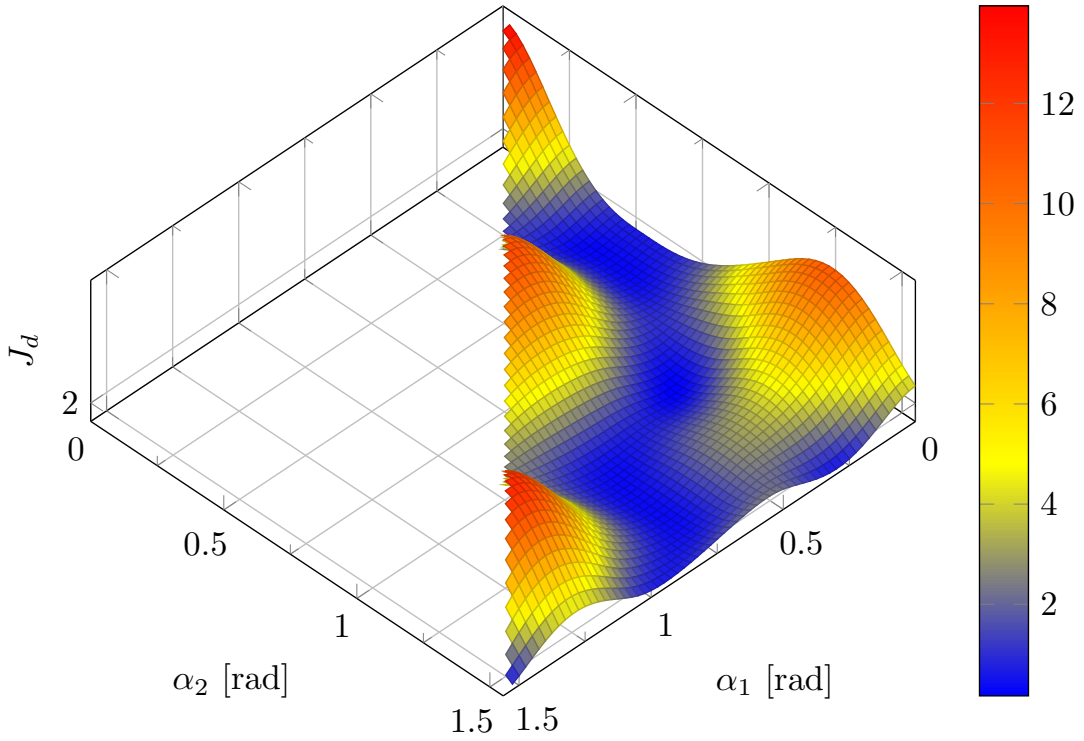

Figure 4.10: Objective function for $p = 2$

4.3 Optimization

The aim of the optimization process is to find commutation angles that minimize the objective function J_d, and thus, minimize the losses that are generated by harmonic currents. Feasible solutions have to maintain a specific modulation index m at the output terminals. The expressions for J_d (4.34) and m (4.10) are nonlinear transcendental functions of commutation angles. Thus, an analytical solution for the optimization is not viable, and the process is done in an iterative way [31].

4.3.1 Objective function

Objective function (4.34) consists of two summations. These summations are usually equivalent to *for-loops* in programming and increase calculation time. Writing the objective function in matrix format is an alternative. For this purpose, commutation angle matrix $\boldsymbol{\alpha}$ and harmonic matrix $\boldsymbol{K}$ are introduced as

$$\boldsymbol{\alpha} = \begin{bmatrix} \alpha_1 & \alpha_2 & \cdots & \alpha_p \end{bmatrix}^T \in \mathbb{R}^{p\times 1}\,, \tag{4.35}$$

$$\boldsymbol{K} = \begin{bmatrix} 5 & 7 & 11 & \dots & k_{\max} \end{bmatrix}^\top \in \mathbb{N}^{|K|\times 1}. \tag{4.36}$$

With this, the product

$$\boldsymbol{K}\cdot\boldsymbol{\alpha}^\top = \begin{bmatrix} 5\alpha_1 & 5\alpha_2 & \cdots & 5\alpha_p \\ 7\alpha_1 & 7\alpha_2 & \cdots & 7\alpha_p \\ \vdots & \vdots & & \vdots \\ k_{\max}\alpha_1 & k_{\max}\alpha_2 & \cdots & k_{\max}\alpha_p \end{bmatrix} \in \mathbb{R}^{|K|\times p}, \tag{4.37}$$

results in a matrix containing all combinations of $k\alpha_i$, which occur in (4.34).

Addtionally, the voltage structure matrix $\boldsymbol{S}$ is introduced as a $1 \times p$ matrix. Voltage structure matrix indexes are equal to 1 for switching to an upper voltage level and are equal to -1 for switching to a lower voltage level.

In MATLAB, it is easy to apply built-in functions to vectors and matrices element by element using a single instruction. Applying the cosine function to each element of $\boldsymbol{K}\cdot\boldsymbol{\alpha}^\top$ is

$$\cos\left(\boldsymbol{K}\cdot\boldsymbol{\alpha}^\top\right)\cdot\boldsymbol{s} \in \mathbb{R}^{|K|\times 1}. \tag{4.38}$$

The result is a column vector. Each row contains the result of the inner sum in (4.34) for the corresponding element in $\boldsymbol{K}$. Now, the objective function can be written in a single line of code, using no explicit summation loops or iterations through vector elements

$$J_d(\boldsymbol{\alpha}) = \left(\frac{1}{\boldsymbol{K}^4}\right)^\top \cdot \left(\cos\left(\boldsymbol{K}\cdot\boldsymbol{\alpha}^\top\right)\cdot\boldsymbol{s}\right)^2\,. \tag{4.39}$$

The division and power operators acting on vectors are, like the cosine function, to be executed element by element, i.e. they are implemented using the $\cdot^\wedge$ operator in MATLAB.

4.3.2 Constraints

Constraints for optimization variables are used to assure that

1. The modulation index of the optimized pulse pattern matches the preset value m.

2. The commutation angles meet (C_5).

Using (4.10), a nonlinear equality constraint for m can be set up

$$c_{\text{eq}}(\boldsymbol{\alpha}) = \frac{4}{\pi} \sum_{i=1}^{p} s(i) \cos(\alpha_i) - m \stackrel{!}{=} 0. \tag{4.40}$$

The second constraint sets a minimum interval between commutations. Let $\Delta\alpha$ be the minimum angle between any two commutations in a pulse pattern, then the commutation angles need to comply with

$$\begin{aligned} \alpha_1 &\geq \Delta\alpha \\ \alpha_2 &\geq \alpha_1 + \Delta\alpha \\ &\vdots \qquad \vdots \\ \alpha_p &\geq \alpha_{p-1} + \Delta\alpha \\ \frac{\pi}{2} &\geq \alpha_p + \frac{\Delta\alpha}{2} \end{aligned}$$

These expressions can be brought into matrix-vector form as well

$$\underbrace{\begin{bmatrix} -1 & 0 & 0 & \cdots & 0 & 0 & 0 \\ 1 & -1 & 0 & \cdots & 0 & 0 & 0 \\ 0 & 1 & -1 & \cdots & 0 & 0 & 0 \\ \vdots & & & & & & \vdots \\ 0 & 0 & 0 & \cdots & 1 & -1 & 0 \\ 0 & 0 & 0 & \cdots & 0 & 1 & -1 \\ 0 & 0 & 0 & \cdots & 0 & 0 & 1 \end{bmatrix}}_{\boldsymbol{A}} \cdot \boldsymbol{\alpha} \leq \underbrace{\begin{bmatrix} -\Delta\alpha \\ -\Delta\alpha \\ -\Delta\alpha \\ \vdots \\ -\Delta\alpha \\ -\Delta\alpha \\ \frac{\pi}{2} - \frac{\Delta\alpha}{2} \end{bmatrix}}_{\boldsymbol{b}}. \tag{4.41}$$

4.3.3 Local optimization

A setpoint for the optimization of a pulse pattern is defined by its associated values of the modulation index m, the minimum distance between commutations $\Delta\alpha$ and the number of commutations p.

The nonlinear objective function $J_d(\boldsymbol{\alpha})$ is minimized with the constraints (4.40) and (4.41). Thus, the optimization problem optimization becomes

$$\begin{aligned} &\min_{\boldsymbol{\alpha}} J_d(\boldsymbol{\alpha}) \\ &\text{subject to} \begin{cases} c_{\text{eq}}(\boldsymbol{\alpha}) = 0 & (4.40) \\ \boldsymbol{A} \cdot \boldsymbol{\alpha} \leq \boldsymbol{b} & (4.41) \end{cases} \end{aligned}$$

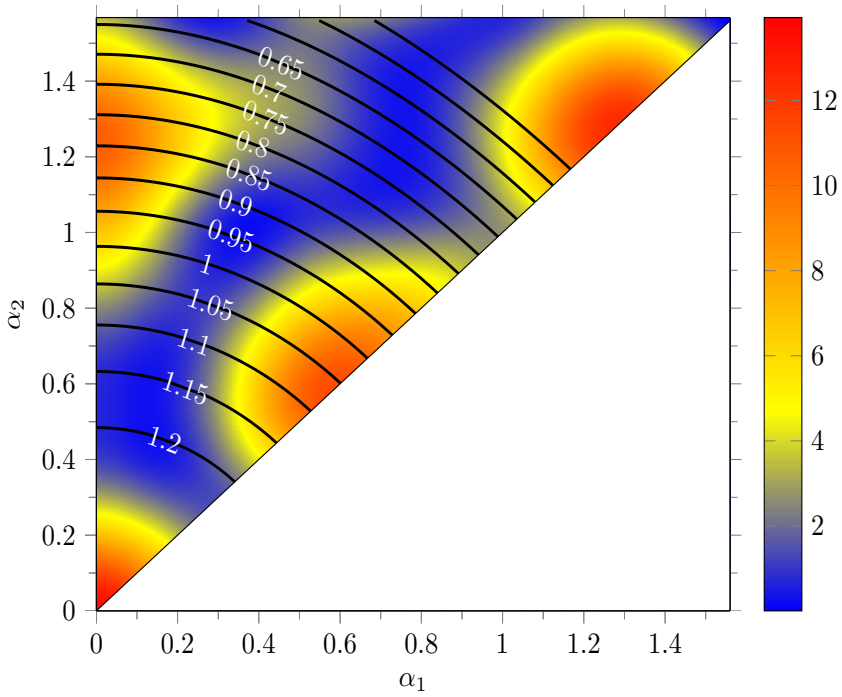

Figure 4.11: Objective function with imposed modulation index constraint lines for $p = 2$

The number of commutations p defines the problem dimension. To ease implementation, the predefined MATLAB function `fmincon` is used for optimization since it can handle nonlinear cost functions as well as linear and nonlinear constraints. It uses an initial $\boldsymbol{\alpha}$ and iterates towards the next local minimum by evaluating gradients of the cost function. As a prerequisite, the cost function needs to be continuously differentiable. This is true for (4.34) and its equivalent vectorized form (4.39).

4.3.4 Global optimization

The constraint optimization is visualized in Figure 4.11 for $p = 2$. The objective function is shown as a function of commutation angles. The domain of the objective function satisfies inequity constraints ($0 \leq \alpha_1 \leq \alpha_2 \leq \frac{\pi}{2}$). On the other hand, modulation index constraint lines are imposed on the domain of the objective function. From this perspective, the optimization procedure at each modulation index m is equivalent to finding the minimum value of the objective function on each of the modulation index constraint lines.

To find a global optimum of the function $J_d(\boldsymbol{\alpha})$, some possible approaches are

1. evaluation of $J_d(\boldsymbol{\alpha})$ on a tight grid of $\boldsymbol{\alpha}$ and selection of the minimum as solution

2. local optimization for several initial values of $\boldsymbol{\alpha}$ and selection of the best local minimum as solution

3. local optimization of one initial $\boldsymbol{\alpha}$ and estimation of the size of its basin of attraction, followed by multiple local optimizations outside this region

4. genetic algorithms

5. pattern search

All five methods are available in MATLAB as predefined functions (2 - 5) or can be programmed easily (1). From a practical point of view, the primary requirements of each method are speed and memory consumption for a certain precision of the solution. A supplementary requirement is the ability to parallelize, i.e. execute the algorithm on multiple CPU cores, which helps to speed up computations. Approach 1 can be implemented using `arrayfun` and needs an exhaustive number of grid points. The parallelization of function evaluations is easy since computations for individual points are independent.

Approach 2 is available through the function `MultiStart` and can consider user-defined initial points. Parallel optimization is possible, and the memory consumption is lower than with approach 1 because of the local optimizations.

Approach 3 uses an involved algorithm and can be accessed through the function `GlobalS--earch`. Only one initial point can be provided by the user, and parallelization is not possible at a global optimization level for one set-point because the selection of new initial points depends on the solution of local optimization runs of the algorithm.

Approach 4 uses random variations in multiple $\boldsymbol{\alpha}$ to generate succeeding iterations ("populations"). In each iteration, the objective function is evaluated to find the best $\boldsymbol{\alpha}$ as a basis for the next iteration.

Approach 5 was not evaluated because of its sparse description in MATLAB documentation.

Approaches 2 and 3 seemed to be the most promising for the given problem and were investigated more thoroughly. For low values of $p < 8$, `GlobalSearch` was fast and proved to provide reliable results. However, since it is not possible to supply more than one initial value for the optimization, there is no way, other than through constraint (4.41), to include knowledge about the necessary ordering of individual commutation angles. In contrast, `MultiStart` allows custom initial points to be supplied by the user. When random sets of initial $\boldsymbol{\alpha}$ with ordered vector entries were supplied to `MultiStart`, it turned out to be faster than `GlobalSearch` for $p \geq 8$.

Based on these observations, the following steps are made to find the global minimum for a specific modulation index m and pulse number p

1. Find all voltage vector structures

2. Calculate the objective function for each voltage vector structure.

3. Generate k randomly chosen initial values on the domain of each calculated distortion function (random initial values on the domain of the objective function for $p = 2$ are shown in Figure 4.12).

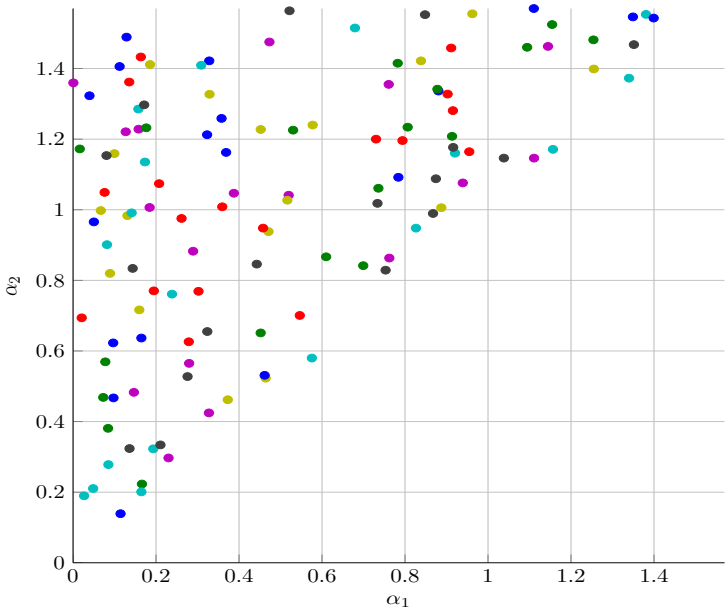

Figure 4.12: Random initial values on the domain of the objective function for $p = 2$

4. Find the optimum value of each objective function starting from any of its initial values using `fmincon` (considering equality and inequality constraints).

5. Find the minimum value of previous optimum values and store commutation angles for selected P and m.

Steps 2 and 3 are a part of the `MultiStart` algorithm.

With random initial values, there is no guarantee that the global optimum has been reached. However, using a large k, the probability to find the global optimum or at least a very good local one is high.

To find an approximate k for reliable results, multiple global optimization runs were done for a single set-point with different k and the results were compared. It took around 20 days for a normal PC to run the optimization for the pulse numbers 2 to 10 for a 5-level inverter.

4.4 Acceleration of the optimization procedure

As mentioned in the previous part, the optimization procedure is very slow. This is due to the fact that our objective function is non-convex. Hence, optimization has to be done repeatedly starting from several different initial points. Then, the results have to be compared in order to find the global minimum and not just a local one. On top of that, the optimization needs to be done for each modulation index, pulse number and voltage waveform structure separately. Besides, each optimization takes several iterations in order to converge to an optimum value. Therefore, the number of calculations that are needed to find optimal pulse patterns for each pulse number p can be expressed as

$$k_p = N_{\text{str}} \cdot N_{\text{m}} \cdot N_{\text{in}} \cdot N_{\text{it}}, \tag{4.42}$$

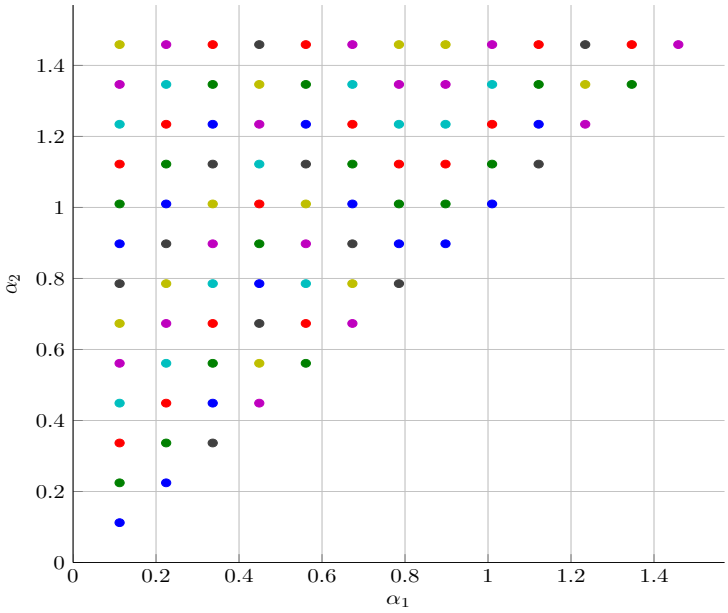

Figure 4.13: Equally distributed initial values on the domain of the objective function for $p = 2$

where N_{str} is the number of voltage structures, N_{m} the number of considered modulation indexes, N_{in} the number of initial values and N_{it} the number of iterations till convergence.

N_{m} is a fixed value that expresses the number of considered modulation index constraints, and is defined based on the desired resolution. For instance, aiming to calculate the optimal switching instances for a modulation range from 0.5 to 1.25 with modulation steps of 0.05 will result in $N_{\text{m}} = 16$. Apparently, N_{m} is a user-defined requirement that cannot be reduced. Therefore, speeding up the calculation procedure is limited to the reduction of N_{str}, N_{in} and N_{it}. In section 4.4.1, it is shown that initial values can be selected only on modulation index constraint lines without affecting optimization precision. As a result, by a reduction in N_{in}, the value k_{p} can be decreased as well. This is being further developed in section 4.4.2. It is shown that the domain of the objective function can be divided into sub-domain regions, where the optimization is necessary only in some of them. It is demonstrated that this scheme reduces k_p by affecting all three terms N_{str}, N_{in} and N_{it}.

4.4.1 Initial values on modulation index constraints

A set of randomly generated initial values on the domain of the objective function is shown in Figure 4.12 for $p = 2$. It is also possible to choose equally distributed initial values as shown in Figure 4.13. Nonetheless, the generation of distributed initial values is not an easy task in higher dimensions.

Choosing random initial values on the domain of objective functions increases the calculation time in two different ways. Firstly, the number of initial values should be big enough to cover the whole domain. As a result, N_{in} shall have a high value. Secondly, most of the chosen initial values are located far away from the optimum point and modulation index constraint line; hence, the number of iterations needed to converge to an optimum value is relatively high. It is noteworthy that in many cases there is no convergence. For instance, imagine a case in

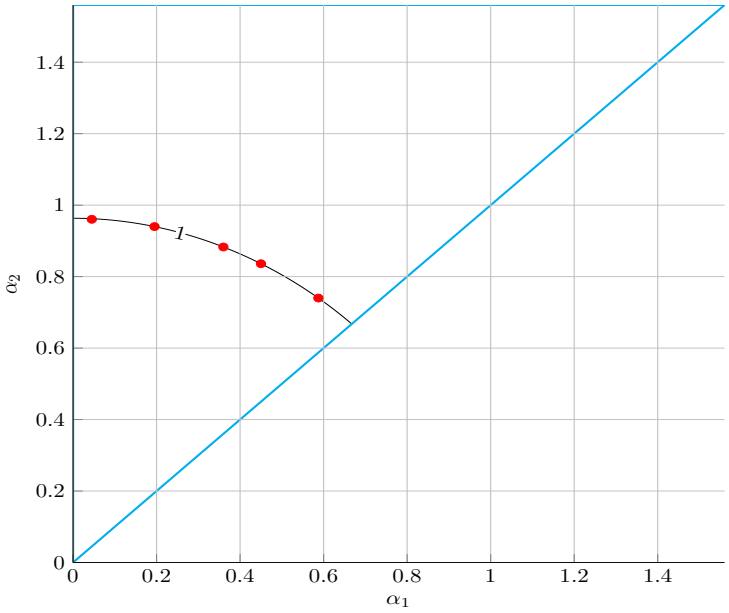

Figure 4.14: Choosing the initial value on the modulation index constraint at $m = 1$ and for $p = 2$

which a local minimum is located close to the chosen initial value and the modulation index constraint is located in a farther distance. It is highly probable that the optimization algorithm gets trapped in the local minimum and does not converge to any minimum that satisfies the modulation index constraint. Consequently, N_{it} in many cases has a high value.

A better approach is to choose initial values on the modulation index constraint. As the optimum value shall satisfy optimization constraints, it has to be located on the modulation constraint as well. Therefore, it is enough to choose several initial values on the respective modulation index constraint and not on the whole domain of the objective function. This is shown for $p = 2$ and modulation index constraint $m = 1$ in Figure 4.14.

There are two switching angles, α_1 and α_2, for $p = 2$. Consequently, the objective function domain is two-dimensional and hence, it is a plane. The modulation index constraint has one dimension less and is a line in this case. In section 4.3.2, the modulation index constraint was defined as

$$c_{\text{eq}}(\boldsymbol{\alpha}) = \frac{4}{\pi} \sum_{i=1}^{p} s(i) \cos(\alpha_i) - m \stackrel{!}{=} 0. \tag{4.43}$$

In general, for a pulse number p the objective function is p-dimensional and the modulation index constraint is $(p-1)$-dimensional. For example, with $p = 3$ the domain is in $3D$ space and the modulation index constraint is a plane. In this case, the selection of the initial values over the modulation index constraint is equivalent to choosing the initial values from a plane instead of from the whole three-dimensional domain.

Let us consider the example for $p = 3$ in more detail. The domain of the objective function is a volume in three-dimensional space where $0 \leq \alpha_1 \leq \alpha_2 \leq \alpha_3 \leq \frac{\pi}{2}$. There are two voltage structures for $p = 3$. The first voltage structure corresponds to voltage levels 0121 and the

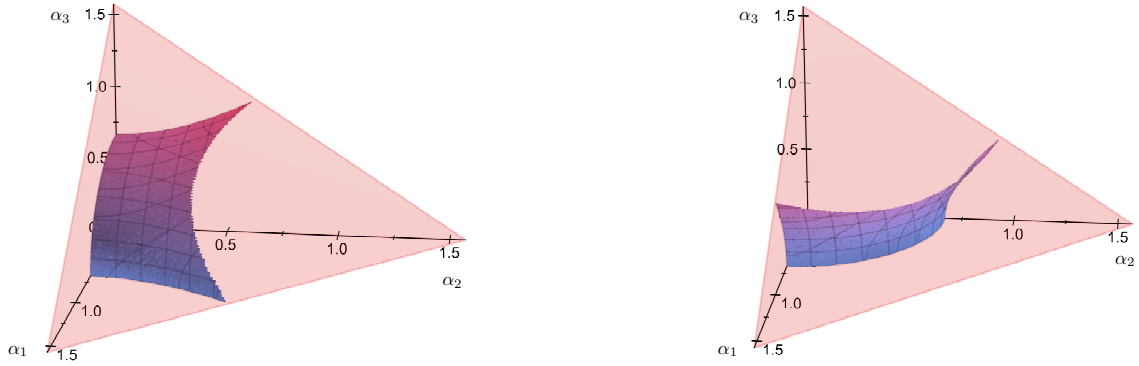

Figure 4.15: Domain of the objective function and modulation index constraints of each voltage structure for $p = 3$

second corresponds to voltage levels 0101. The objective function and the modulation index constraints for voltage structure 0121 are defined as

$$J_{d,1} = \sum_{k \in H} \frac{1}{k^4} \left(\cos\left(k\alpha_1\right) + \cos\left(k\alpha_2\right) - \cos\left(k\alpha_3\right)\right)^2, \tag{4.44}$$

$$\frac{4}{\pi} \left(\cos\left(\alpha_1\right) + \cos\left(\alpha_2\right) - \cos\left(\alpha_3\right)\right) - m = 0, \tag{4.45}$$

and for voltage structure 0101

$$J_{d,2} = \sum_{k \in H} \frac{1}{k^4} \left(\cos\left(k\alpha_1\right) - \cos\left(k\alpha_2\right) + \cos\left(k\alpha_3\right)\right)^2, \tag{4.46}$$

$$\frac{4}{\pi} \left(\cos\left(\alpha_1\right) - \cos\left(\alpha_2\right) + \cos\left(\alpha_3\right)\right) - m = 0. \tag{4.47}$$

In the standard approach randomly generated initial values are chosen in the three-dimensional space where $0 \leq \alpha_1 \leq \alpha_2 \leq \alpha_3 \leq \frac{\pi}{2}$ and two constrained optimization problems are solved separately. Afterwards, the results are compared and the switching angles and the voltage structure corresponding to minimum distortion are chosen. Conversely, the approach with initial values on the modulation index constraint only considers randomly generated initial values on the surface described in (4.45) to optimize the objective function $J_{d,1}$ and on the surface described in (4.47) to optimize the objective function $J_{d,2}$. Eventually, the results are compared to find the optimum switching angles and voltage structure. The objective function domain and the modulation index constraints are depicted in Figure 4.15 for $m = 1$.

Limiting the initial values to the modulation index constraints speeds up the calculation procedure. Firstly, initial values are selected randomly on a $(p-1)$-dimensional space instead of on a p-dimensional space. Secondly, the optimization procedure always starts from a point on the optimization constraints. So the convergence is fast and more probable. However, the

optimization time will remain relatively high due to the fact that still too many initial values have to be evaluated in each case and the optimization is done for each voltage vector structure separately.

4.4.2 Spliting the global optimization to multiple regional optimizations

Assumption (C_3) was introduced to exploit three-phase symmetry, based on which it became possible to run the optimization for a single-phase system and extend the results to a three-phase system. In this part, the problem is reconsidered in all three phases in order to see if this simplification results in losing useful information that could have been used to facilitate the optimization procedure.

The 5-level voltage waveform of Figure 4.2 is shifted by 120° and 240° to obtain the corresponding three-phase waveform. The result is shown in Figure 4.16. The three segments in the first quarter of phase a, with a length of 30°, are plotted in different colors. In the next quarters, the segments are plotted with the same color as their corresponding symmetrical part in the first quarter. This waveform is shifted by 120° and 240° for the phases b and c. It can be seen that in each 30°-segment of the three-phase waveform, all three colors exist. This means that with the information in 30° of a three-phase waveform, the rest can be derived by symmetry properties. In other words, half-wave and quarter-wave symmetries of a single-phase waveform are equivalent to 30°-symmetry in three-phase waveforms.

Three-phase voltages can be transformed to stator-fixed coordinates via Clarke transformation. 5-level voltage vectors and their symmetries in the $\alpha\beta$ plane are shown in Figure 4.17.

Figure 4.18 displays all voltage vectors of a 5-level converter in the 30° segment specified in Figure 4.17 together with the imposed modulation index lines. Every voltage waveform corresponds to a certain voltage vector sequence in this 30° segment, while optimal voltage vector sequences shall comply with the following rules

- Switching is allowed only from one voltage vector to another adjacent voltage vector.
- At each switching transition, only one leg of the converter is allowed to switch one level up or down. As a result, switching from $\{001\}$ to $\{-1-10\}$ is not allowed because switching takes place in all the phases and switching from $\{-1-21\}$ to $\{-1-2-1\}$ is not allowed due to the fact that phase c has a two-level change.
- A feasible voltage vector sequence for each modulation index consists of voltage vectors in the vicinity of the modulation index constraint as shown in Figure 4.18.
- A feasible voltage vector sequence starts with a voltage vector at the beginning of a 30° section and terminates with a voltage vector at its end.

In addition, each point on the domain of the objective function represents a voltage vector sequence. Let us go back to our typical case study with $p = 2$. Each point on the objective function (Figure 4.11) represents a certain voltage waveform for phase a. Three-phase symmetry can be used to generate the corresponding three-phase waveform for each point. Afterwards, three-phase waveforms are transfered to $\alpha\beta$ coordinates. Finally, the α and β waveform is translated to a set of voltage vector sequences.

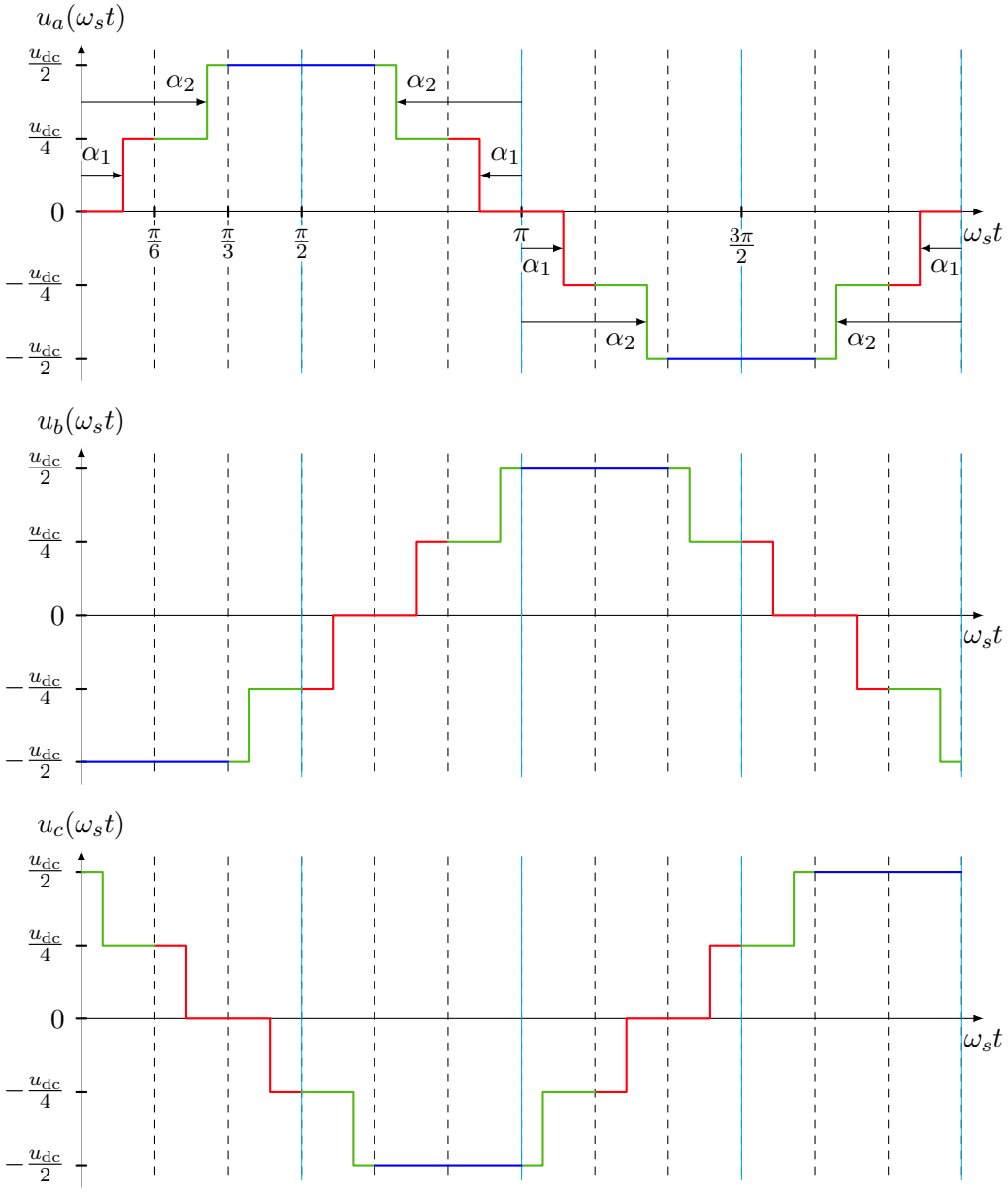

Figure 4.16: Three-phase voltages of a five level inverter

Changing the switching angles α_1 and α_2 from 0 to $\frac{\pi}{2}$ and obtaining the corresponding voltage vector sequence for each point defines certain regions over the domain of the objective function in which the voltage vector sequence is unique. These regions are shown in Figure 4.19 for $p = 2$.

Voltage vector sequences for $p > 2$ can be defined by the same principle.

Here we face two new pieces of information. One is used to divide the voltage vector sequences into feasible and infeasible sequences and the other to split the objective function domain into regions with a unique voltage vector sequence. Obviously, it makes no sense to run the optimization in the regions with infeasible voltage vector sequences. As a result, the

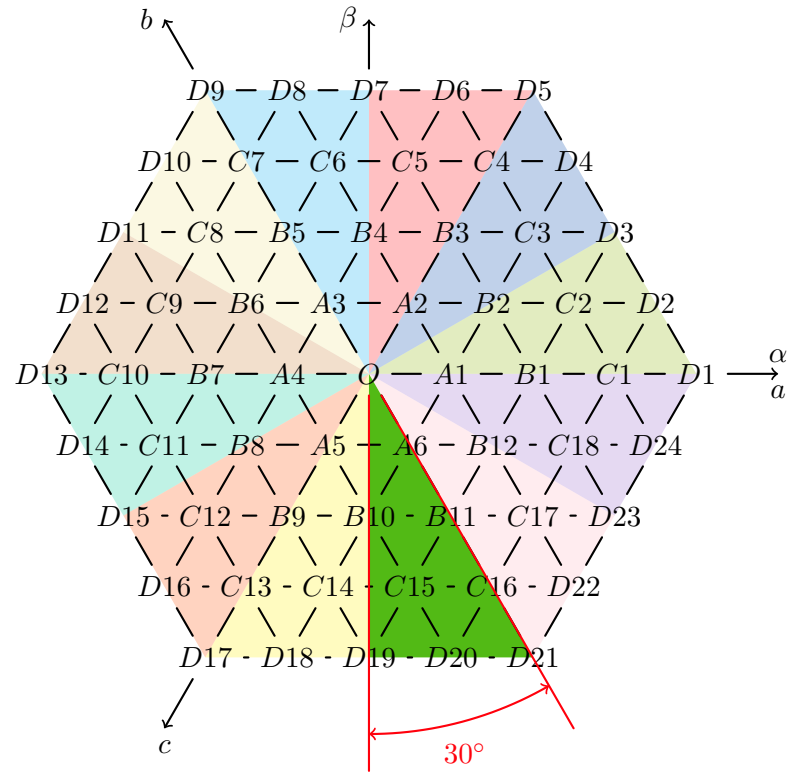

Figure 4.17: Three-phase voltages of a 5-level inverter

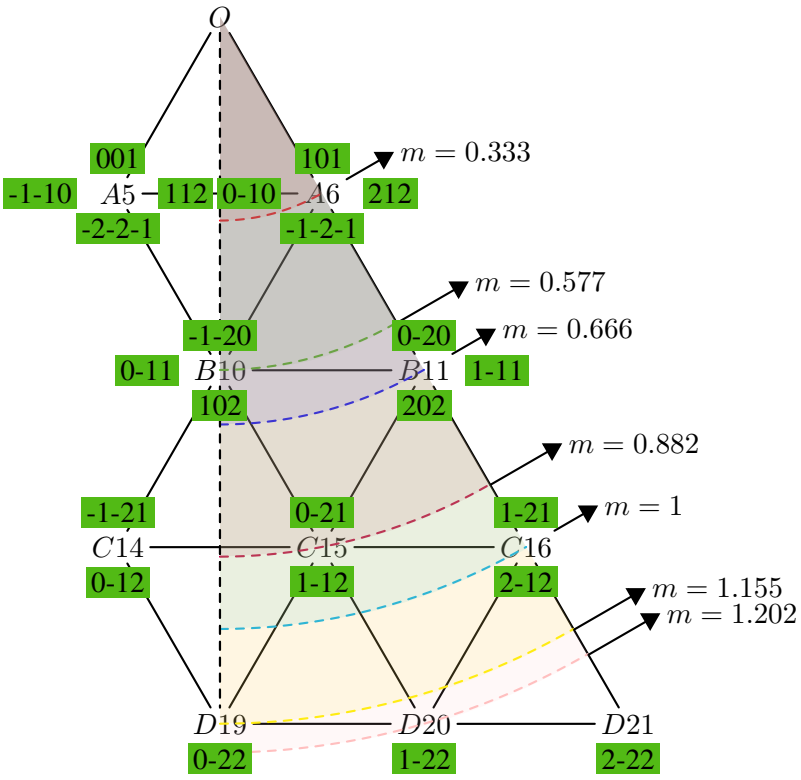

Figure 4.18: Three-phase voltages of a 5-level inverter

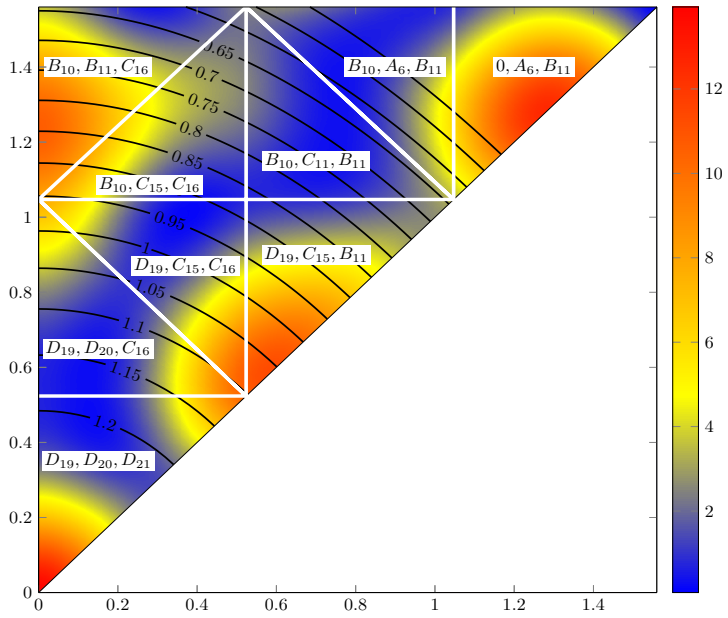

Figure 4.19: Objective function with imposed modulation index constraint lines and voltage vector sequences for $p = 2$

optimization procedure can be modified for a specific pulse number p and modulation index m to

- Find all feasible voltage vector sequences.
- Calculate the distortion of each voltage vector sequence as a function of commutation angles.
- Choose a single initial value for each objective function in the voltage vector sequence region and on the modulation index constraint (this is shown in Figure 4.20 for $p = 2$ and $m = 1$).
- Find the constrained optimum value of each distortion function starting from the selected initial value using `fmincon`.
- Repeat the previous two steps in the case of no convergence.
- Find the minimum value of previous optimal values and store the commutation angles for the selected p and m.

In the classical approach, optimization is done for all voltage vector structures, whereas in the second approach, optimization is done for each feasible voltage vector sequence. As a result, it is not required to evaluate as many voltage vector structures. Besides, a regional optimization would be enough for the considered voltage structures.

The number of calculations in this approach for each modulation index constraint m and for each pulse number p is only dependent on the number of feasible regions and calculation iterations. Therefore, the number of calculations needed to find optimal pulse patterns for each pulse number p can be expressed as

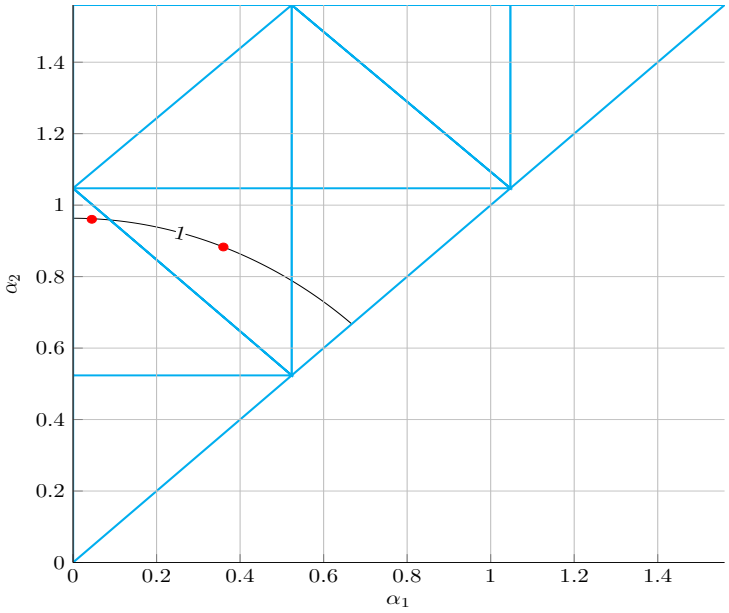

Figure 4.20: Initial values for $p = 2$

$$k_p = \sum_{m \in \boldsymbol{M}} N_{\text{vvs,m}} \cdot N_{\text{it,m}}, \tag{4.48}$$

where $N_{\text{vvs,m}}$ is the number of feasible voltage vector sequences for the modulation index m, $N_{\text{it,m}}$ is the number of iterations needed to converge to an optimal value and $\boldsymbol{M}$ is the modulation index array. An example is given for $p = 7$ and the modulation index array, $\boldsymbol{M} = \{0.5, 0.55, ..., 1.25\}$. With the classical approach, the number of calculations is equal to $k_p = 8.8 \times 10^8$, whereas it reduces to 3400 by applying the alternative approach.

The next notable advantage of splitting the global optimization to multiple regional optimizations is that not only much fewer cases are required to be optimized (i.e. fewer voltage structures and less initial values), but also the number of iterations needed for convergence is much lower. This is due to the fact that the initial value is always chosen in a feasible region and on the modulation index constraint. Hence, the initial value is already very close to the optimum point. As a result, few iterations are enough to converge from the initial point to an optimum.

It is not proven that voltage vector sequence regions are convex; however, in most cases selection of a single initial value in each region is enough to find its minimum. As can be seen in Figure 4.19, the cost function in each region is either convex or concave. This trend is also observed for higher pulse numbers by performing several simulations. Notwithstanding that there is no mathematical proof for the regional convexness, the consensus is that very few initial points and in most cases only one initial value is enough to perform the optimization in each region. This has been examined by running the optimization several times with different initial values and getting the same optimal point repeatedly.

4.5 Optimization results

Classical and accelerated approaches are used to solve the same optimization problem. Therefore, both result in identical optimal voltage waveforms. However, it takes over 400 hours for a normal PC to calculate optimal pulse patterns for a 5-level converter with the standard approach, while applying the accelerated optimization reduces calculation time to a few hours.

Optimization is done for pulse numbers p from 2 to 10 and modulation index array $\boldsymbol{M} = \{0.5, 0.51, 0.52..., 1.27\}$. Optimal switching angles are shown in Figure 4.21. In addition to switching angles, voltage structures or voltage vector sequences are also needed to generate the optimal pulse pattern. Table 4.1 contains optimal switching angles and optimal voltage vector sequences for $p = 10$. The results for $p = 2$ to $p = 10$ can be found in Appendix B.

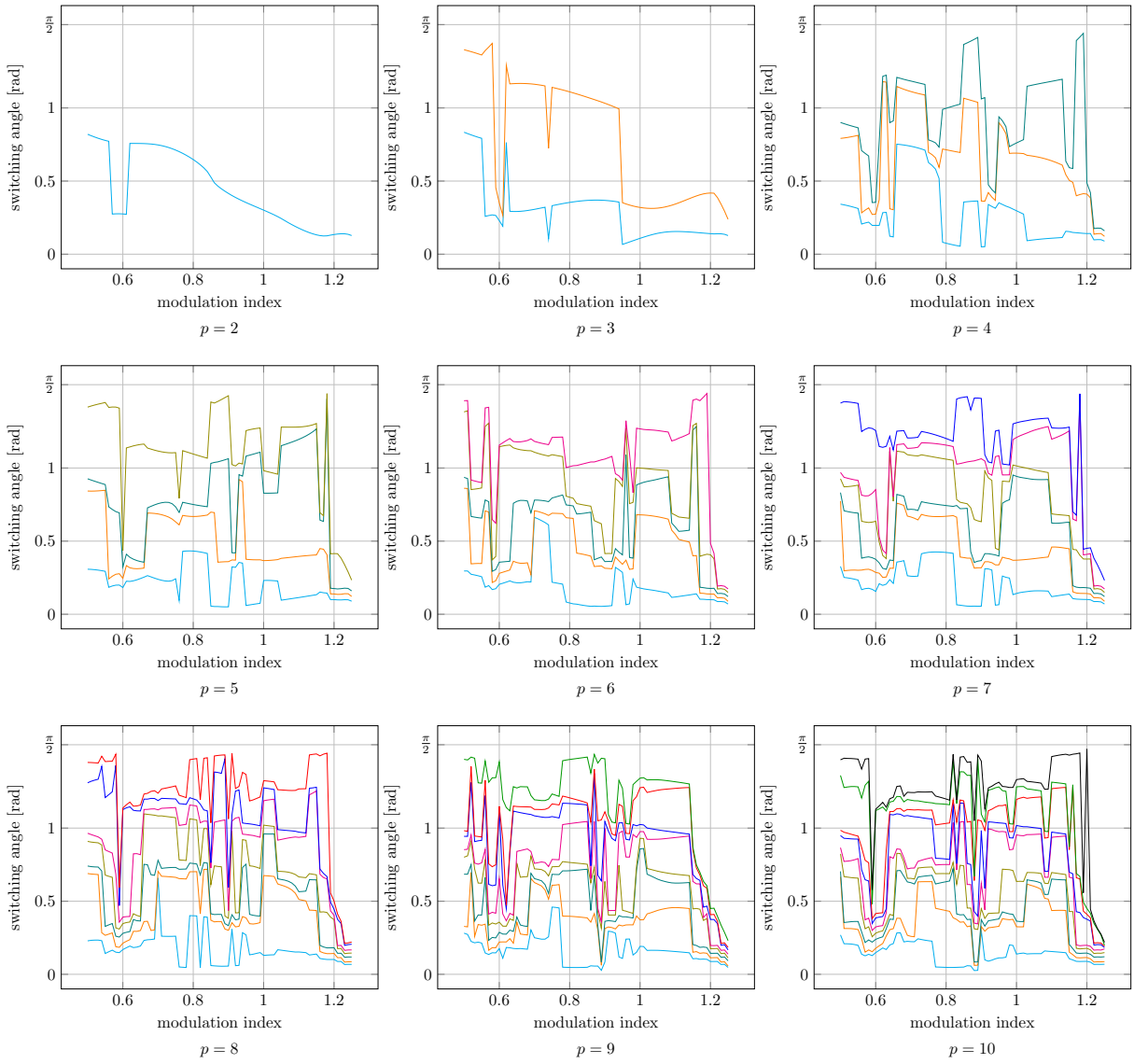

Figure 4.21: Optimal switching angles for $p = 2$ to $p = 10$

Table 4.1: Optimization results for $p = 10$

m	0,50	0,55	0,60	0,65	0,70	0,75	0,80	0,85	0,90	0,95	1,00	1,05	1,10	1,15	1,20	1,25
$\boldsymbol{\alpha}$	0,269	0,198	0,160	0,210	0,223	0,230	0,048	0,049	0,085	0,112	0,138	0,141	0,156	0,099	0,087	0,068
	0,667	0,306	0,194	0,312	0,260	0,634	0,436	0,359	0,297	0,328	0,325	0,602	0,435	0,133	0,113	0,086
	0,704	0,361	0,256	0,375	0,627	0,674	0,633	0,408	0,330	0,379	0,364	0,638	0,652	0,171	0,144	0,120
	0,823	0,658	0,305	0,402	0,656	0,733	0,689	0,742	0,380	0,420	0,635	0,695	0,696	0,433	0,176	0,129
	0,866	0,792	0,347	0,794	0,726	0,793	0,751	1,045	0,432	0,975	0,954	0,957	0,937	0,654	0,197	0,131
	0,949	0,925	0,421	1,090	1,081	1,064	0,789	1,170	0,597	1,035	1,018	1,003	0,972	0,688	0,375	0,144
	0,985	0,945	0,609	1,113	1,125	1,123	1,032	1,186	0,998	1,154	1,196	1,210	1,270	1,256	0,407	0,166
	1,360	1,282	1,129	1,184	1,191	1,175	1,163	1,384	1,045	1,282	1,282	1,262	1,314	1,279	0,450	0,205
	1,467	1,471	1,141	1,211	1,243	1,247	1,199	1,489	1,111	1,314	1,331	1,314	1,488	1,504	1,558	0,220
	1,536	1,550	1,507	1,325	1,332	1,552	1,529	1,540	1,527	1,564	1,436	1,357	1,556	1,551	1,568	0,221
Structure	1	3	24	15	28	31	7	26	31	15	31	31	31	30	12	18
Vector sequence	B10	B10	B10	B10	B10	B10	B10	B10	D19	D19	D19	D19	D19	D19	D19	D19
	A6	A6	C15	C15	C15	C15	C14	C14	C15	C15	C15	C15	C15	D20	D20	D20
	B10	B10	B10	B10	B10	B10	C15	C15	D19	D19	D19	D19	D19	D19	D19	D19
	A6	B11	B11	C15	C15	C15	B10	B10	C14	C14	D20	D20	D20	D20	D20	D20
	B10	A6	B10	B10	B10	B10	C15	C15	C15	C15	C15	C15	C15	C15	D19	D21
	B11	B10	B11	B11	B11	B11	B11	B11	C16	D20	D20	D20	D20	D20	D20	D20
	A6	B11	B10	C15	B10	C15	C15	C16	C15	C15	C15	C15	C16	C16	D21	D19
	B10	B10	B11	B10	C15	B11	B11	C15	C16	C16	C16	D20	D20	D20	D20	D20
	A6	A6	B10	B11	B11	C15	C15	C16	C15	C15	C15	C16	D21	D21	D21	D19
	B11	B11	A6	B10	C15	B11	C16	B11	B11	C16	D20	D20	C16	C16	C16	D20
	A6	A6	B11	B11	B11	C16	B11	C16	C16	B11	C16	C16	D21	D21	B11	D21
d	0,054	0,047	0,037	0,041	0,046	0,050	0,049	0,045	0,037	0,044	0,048	0,046	0,048	0,037	0,102	0,528

4.5.1 Optimal voltage waveform

Optimal pulse pattern for $p = 4$ and $m = 0.8$ is fetched from the table and the optimal phase voltage u_a is generated for the converter with a DC-link voltage of $500\ \mathrm{V}$. Phase voltage u_a and phase to phase voltage u_{ab} are shown in Figure 4.22 with their respective harmonic spectrum.

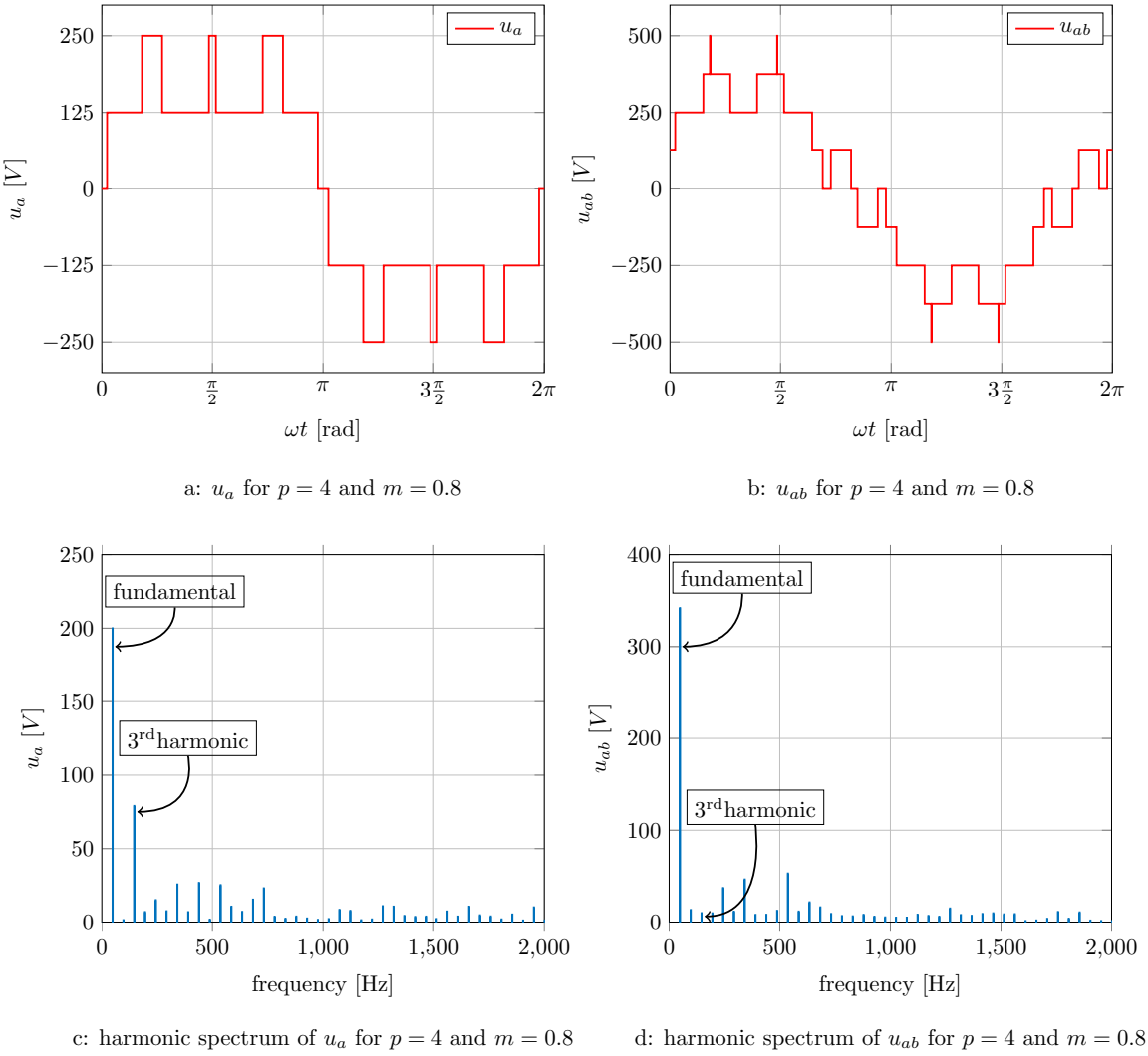

a: u_a for $p = 4$ and $m = 0.8$

b: u_{ab} for $p = 4$ and $m = 0.8$

c: harmonic spectrum of u_a for $p = 4$ and $m = 0.8$

d: harmonic spectrum of u_{ab} for $p = 4$ and $m = 0.8$

Figure 4.22: Voltage waveforms and their harmonic spectrum for $p = 4$ at $m = 0.8$

The RMS value of u_a can be divided into its fundamental, triplen and non-triplen harmonics

$$u_{a,\mathrm{rms}}^2 = u_{a1,\mathrm{rms}}^2 + \left(u_{a3,\mathrm{rms}}^2 + u_{a9,\mathrm{rms}}^2 \cdots\right) + \left(u_{a5,\mathrm{rms}}^2 + u_{a7,\mathrm{rms}}^2 + \cdots\right). \tag{4.49}$$

The optimization is done in order to find switching angles in which $u_{a1,\mathrm{rms}}$ meets the modulation index constraint and in which the weighted sum of non-triplen harmonics are minimal. As a result, it is expected that triplen harmonics have a high amplitude in the optimal voltage waveforms. This can be seen in the harmonic spectrum of u_a, in which the fundamental's am-

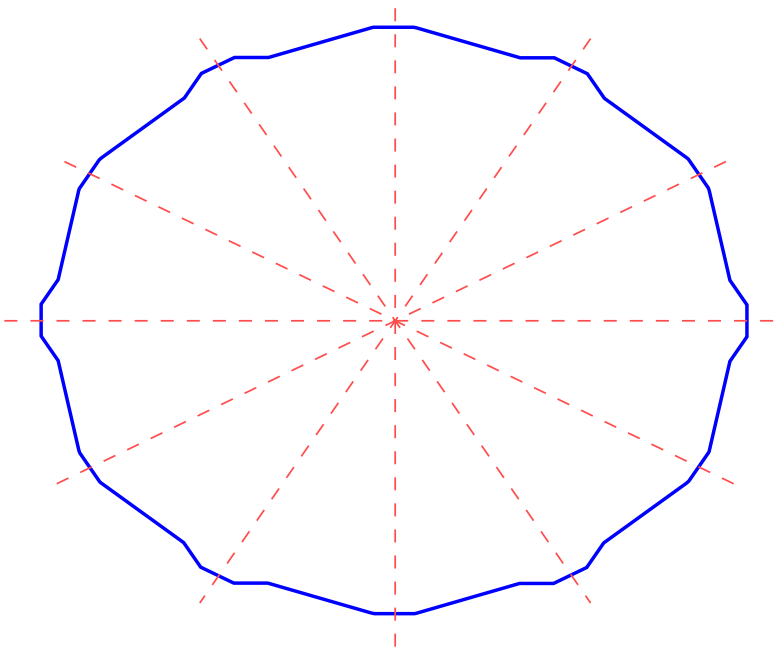

Figure 4.23: Integral of optimal pulse train for $p = 4$ and $m = 0.8$ in $\alpha\beta$ plane

plitude is 200 V, which is exactly equal to 80% of $\frac{u_{\mathrm{dc}}}{2} = 250V$, and in which the 3^{rd} harmonic's amplitude is over 30%.

An induction motor is usually considered as a highly inductive load. Thus, $\int \boldsymbol{u} \cdot dt$ is a good approximation of the stator flux or current from the distortion point of view. $\int \boldsymbol{u} \cdot dt$ is plotted in $\alpha\beta$ plane for $p = 4$ and $m = 0.8$ in Figure 4.23. The trajectory has a clear 30° symmetry, which is equivalent to the introduced half-wave and quarter-wave symmetries in the single-phase waveform.

It has to be mentioned that when a voltage vector is applied , $\int \boldsymbol{u} \cdot dt$ in $\alpha\beta$ plane will start from its initial value and continue in the same direction as the applied voltage vector. A close look at the trajectory of $\int \boldsymbol{u} \cdot dt$ reveals that in an optimal trajectory, switching transitions take place from one voltage vector to another one that has a relatively small phase shift. As a result, the flux trajectory has smooth corners at each switching point. This is another clue for the fact that two adjacent voltage vectors in an optimal voltage vector sequence have to be on the same triangle in the voltage vector hexagon of the converter.

4.5.2 Discontinuities of optimal switching angles

Optimized commutation angles usually exhibit discontinuities (large differences in switching angles for two adjacent modulation indexes). This causes transients in the phase current whenever the modulation index passes a point of discontinuity. A post-optimization technique is proposed in [32] to avoid the problem. It recalculates the switching angles starting at the point of discontinuity by considering the initial values equal to the optimal commutation angles just before the point of discontinuity. In fact, the discontinuity occurs when the optimal value

is chosen from two different regions of voltage vector sequences for two adjacent modulation indexes. In principle, starting the optimization at the point of discontinuity with the previous optimal point as an initial value will find an optimum value in the same voltage vector sequence region before the discontinuity. Therefore, it would be sufficient to choose the optimal point from a single region for a certain range of the modulation index instead of re-optimizing the objective function.

This post-optimization procedure is beyond the motivation of this work. However, a similar approach is used in the following chapter in order to define the optimal voltage vector sequence at each operating point.

4.5.3 Application of Optimal Pulse Patterns

Optimal pulse patterns are determined by offline calculations and with the assumption of steady-state operation points. So the simplest way of operating a machine with OPPs is to determine the pulse number p and modulation index m at the desired operating point, fetch the corresponding pulse number from the look-up table and finally apply the pulses to the converter. This is an open-loop approach that is commonly used for several low performance MV drive applications such as industrial fans and pumps.

Figure 4.24 depicts the structure of an open-loop U/f control scheme with optimal pulse patterns. The U/f controller generates a reference voltage vector $\boldsymbol{u}_\mathrm{s}^*$. The pulse number p and the modulation index m are defined based on the magnitude and the frequency of $\boldsymbol{u}_\mathrm{s}^*$. Then, the switching angles can be fetched from the look-up table in order to generate the optimal pulse train $\boldsymbol{u}_\mathrm{opt}$. It is noteworthy that the switching angles are usually stored for the first quarter of the voltage waveform. Hence, with $\boldsymbol{u}_{\mathrm{opt},1}$ being the optimal pulse train for $0 \leq \alpha \leq \frac{\pi}{2}$, the

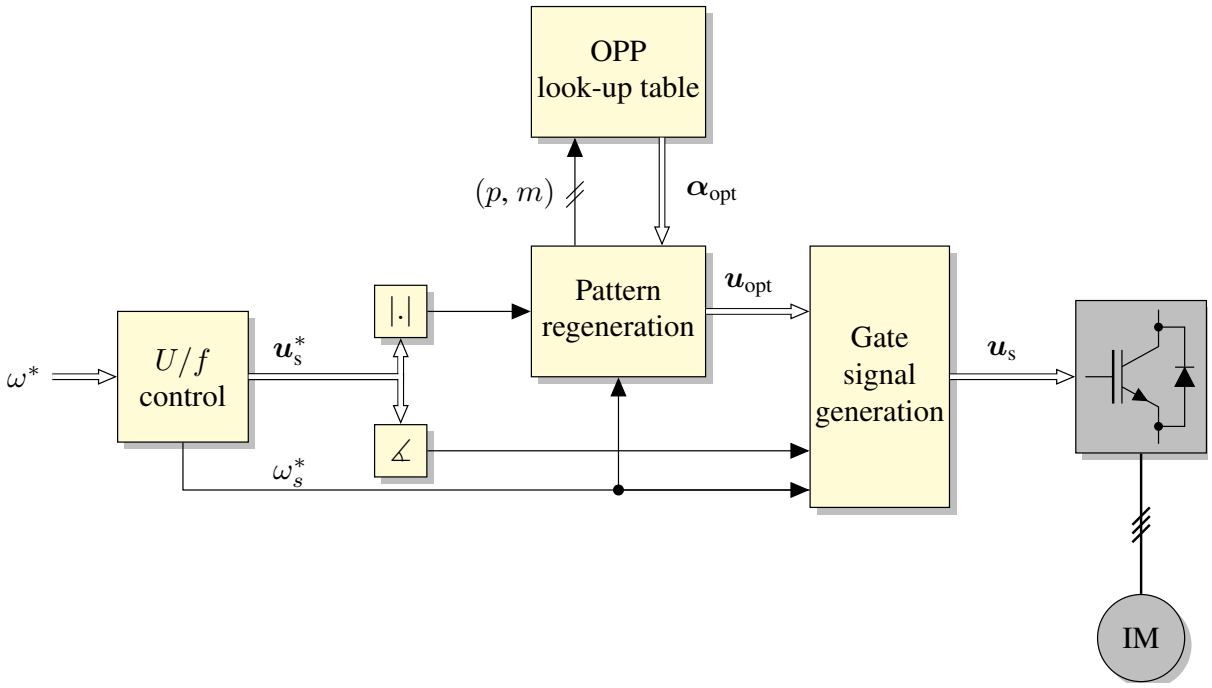

Figure 4.24: Open-loop U/f control scheme with optimal pulse patterns

remaining portions of a full fundamental cycle are determined using half-wave and quarter-wave symmetries

$$\begin{aligned} &\text{for } \frac{\pi}{2} \leq \alpha \leq \pi: && \boldsymbol{u}_{\mathrm{opt}} = \boldsymbol{u}_{\mathrm{opt},2} = \boldsymbol{u}_{\mathrm{opt},1}(\pi - \alpha), \\ &\text{for } \pi \leq \alpha \leq 2\pi: && \boldsymbol{u}_{\mathrm{opt}} = \boldsymbol{u}_{\mathrm{opt},3} = \boldsymbol{u}_{\mathrm{opt},1,2}(2\pi - \alpha). \end{aligned}$$

Finally, $\boldsymbol{u}_{\mathrm{opt}}(\alpha)$ is transferred to $\boldsymbol{u}_{\mathrm{opt}}(t)$ based on the synchronous frequency ω_{s}^*, and the gate signals are generated according to $\measuredangle \boldsymbol{u}_{\mathrm{s}}^*$.

The performance of optimal pulse patterns in an open-loop U/f control at steady-state operation is shown for $\omega_{\mathrm{m}} = 600\ \mathrm{rpm}$ and $\omega_{\mathrm{m}} = 1450\ \mathrm{rpm}$ with and without load. Figures 4.25 and 4.27 illustrate the phase voltages and stator currents at $\omega_{\mathrm{m}} = 600\ \mathrm{rpm}$ and at no-load operation, whereas Figures 4.26 and 4.28 show the voltage and current waveforms at $T = 15$ Nm. The current in no-load operation is more distorted than the current in the presence of a load. At $\omega_{\mathrm{m}} = 600\ \mathrm{rpm}$ and thus with a pulse number equal to 10, Total Harmonic Distortion (THD) decreases from $5.9\ \%$ to $3.6\ \%$ while the load increases from $0\ \mathrm{Nm}$ to $15\ \mathrm{Nm}$. Besides, the steady-state current trajectories are shown in Figures 4.29 and 4.30.

Figures 4.31 and 4.33 shows phase voltages and stator currents at nominal speed and no-load operation. The results for $T = 15$ Nm at nominal speed are given in Figures 4.32 and 4.34 respectively. The results match with the previous observation that the current in no-load operation is more distorted than the current in the presence of a load. At $\omega_{\mathrm{m}} = 1450\ \mathrm{rpm}$ and thus with a pulse number equal to 2, THD decreases from $12.5\ \%$ to $8.0\ \%$, while the load increases from $0\ \mathrm{Nm}$ to $10\ \mathrm{Nm}$.

Figure 4.34 shows the stator current with only two switchings per a quarter of the fundamental period. It is impossible to achieve such a low current distortion at a switching frequency of only $100\ \mathrm{Hz}$ without setting the switching instances based on the distortion optimization results. Stator current trajectories are also given for nominal speed operation point in Figures 4.35 and 4.36.

As the machine is regulated with an open-loop control scheme, it is not expected to have good dynamics. The use of optimal pulse patterns in a closed-loop control system is difficult. Having a closed-loop control means that the drive system is operating at quasi steady-state instead of steady-state. Quasi steady-state operation implies that the reference voltage vector varies, at least slightly, from each sample time to the other. Transferring between neighboring pulse patterns takes place as a consequence. Discontinuities of the switching angles and transitions between neighboring pulse patterns can introduce harmonic excursions.

Too many transitions between optimal pulses cause two problems

- Current spikes and harmonic excursions increase the total harmonic distortion. Hence, the drive does not operate at optimal current distortion any more.
- In addition to the fact that current overshoots deteriorate the performance, they also lead to unwanted trips in some cases.

The most promising solution to overcome the problems associated with OPP's application to a closed-loop control scheme is stator flux trajectory control, in which optimized pulses are

shifted in time based on the error between the estimated flux and the flux trajectory of an optimal pulse train [34]. The details of the pulse shifting scheme are explained in the next chapter.

Steady-state results at $\omega_{\mathrm{m}} = 600$ rpm and $p = 10$

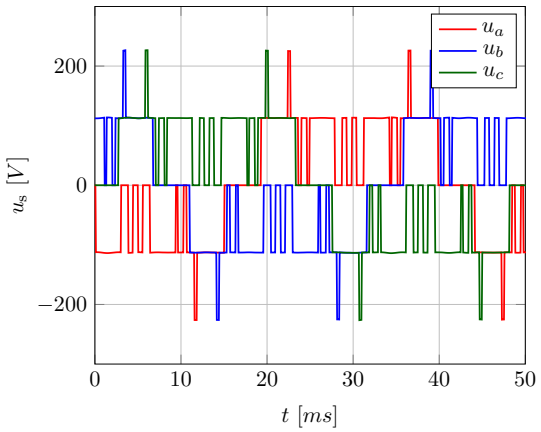

Figure 4.25: Stator voltages at no-load operation

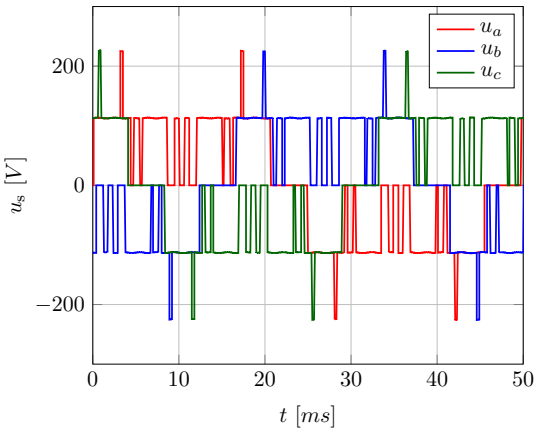

Figure 4.26: Stator voltages at $T = 15$ Nm

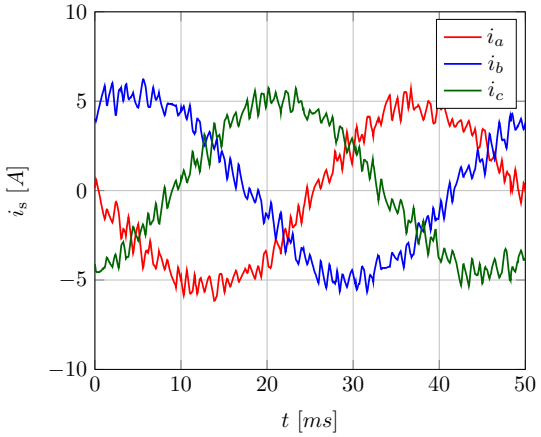

Figure 4.27: Stator currents at no-load operation

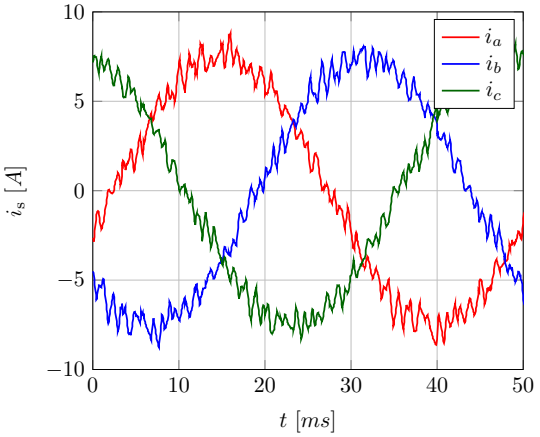

Figure 4.28: Stator currents at $T = 15$ Nm

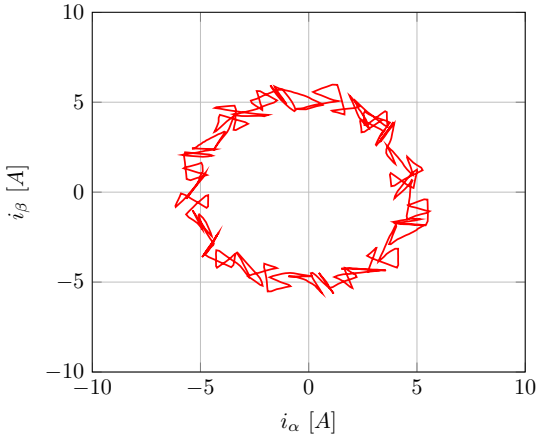

Figure 4.29: Stator current in $\alpha\beta$ at no-load operation

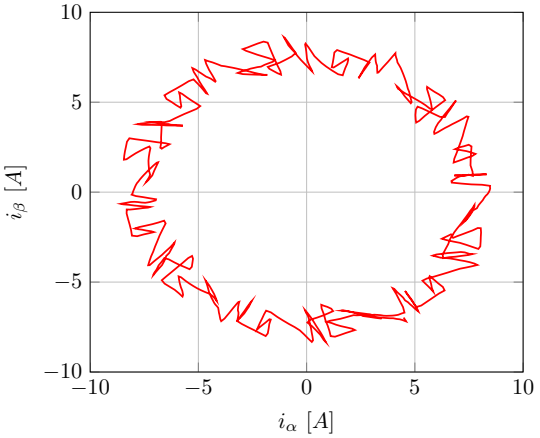

Figure 4.30: Stator current in $\alpha\beta$ at $T = 15$ Nm

Steady-state results at $\omega_{\mathrm{m}} = 1450$ rpm and $p = 2$

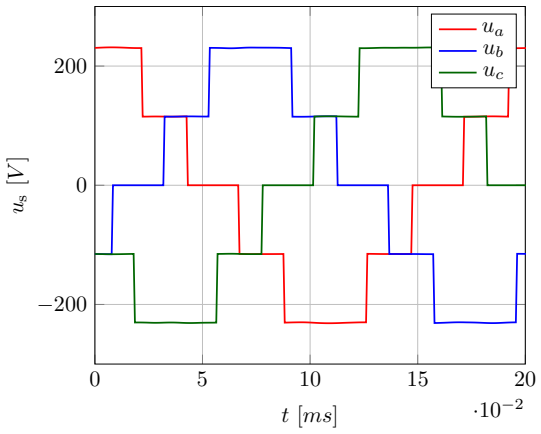

Figure 4.31: Stator voltages at no-load operation

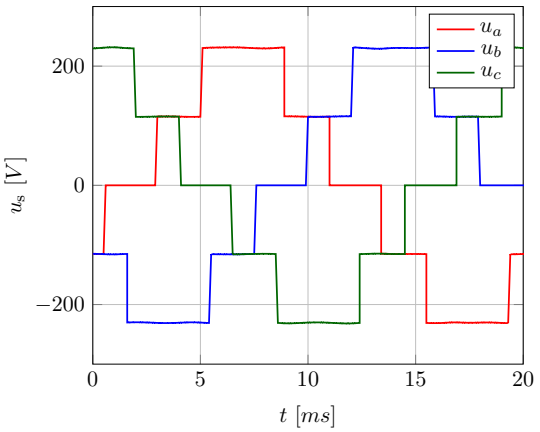

Figure 4.32: Stator voltages at $T = 15$ Nm

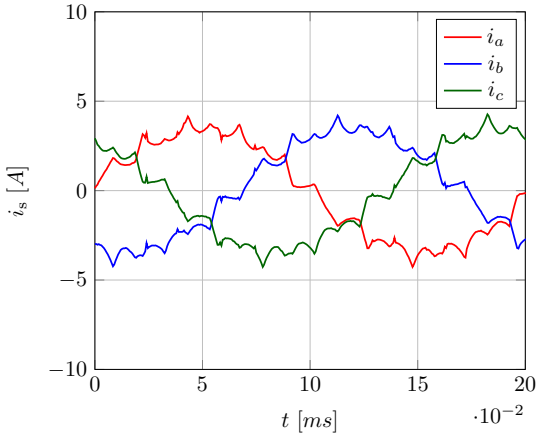

Figure 4.33: Stator currents at no-load operation

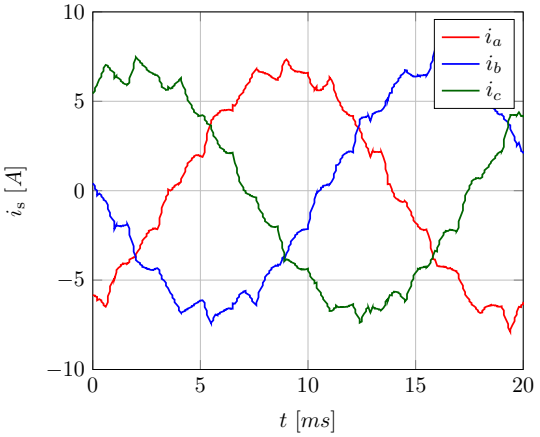

Figure 4.34: Stator currents at $T = 15$ Nm

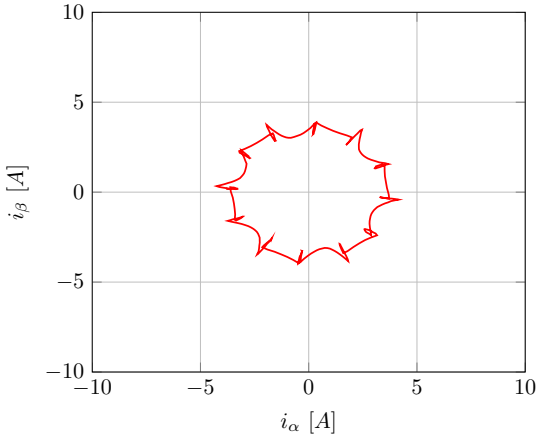

Figure 4.35: Stator current in $\alpha\beta$ at no-load operation

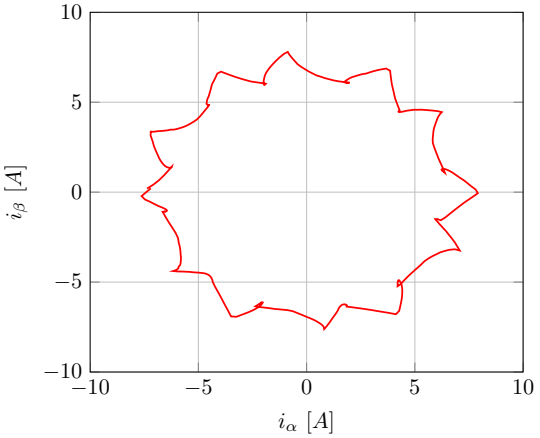

Figure 4.36: Stator current in $\alpha\beta$ at $T = 15$ Nm

CHAPTER 5

Predictive-based current distortion optimization

As summarized in Table 2.6, SHE, OPP and hysteresis-based MPC are the only schemes which are available for very low switching frequencies (below $200\ \mathrm{Hz}$). SHE and OPP share a similar concept. In both approaches, switching instances of the converter are calculated in order to either eliminate undesired harmonics or shape the whole spectrum in a certain way. However, OPP has a superior performance regarding harmonic distortion and overall harmonic losses.

In literature it is reported [2, 100, 101] that OPP and hysteresis-based MPC schemes have a comparably low current distortion. However, MPC has a variable switching frequency and is executable in real-time, while OPPs exploit the concept of synchronous modulation and are based on offline optimization results. Features of both schemes can be achieved via a single predictive-based approach in which:

- The current distortion is included in the objective function.
- The prediction horizon is proportional to the period of the fundamental current waveform.
- The number of switching transitions in the prediction horizon is fixed.

5.1 Real-time optimization

Two remarks about the calculation time and optimization range of the real-time optimizer need to be made at the very beginning. Firstly, dealing with real-time optimization, it is important to consider the calculation time in each step of the control design from system modeling to the objective function and the solver selection. Secondly, it should be noted that regardless of the applied modulation scheme, harmonic distortion is very low at a low modulation index. This is because for low modulation indexes, a zero vector is turned on for most of the sub-cycle time and active voltage vectors lead to only a small change in the pulse train, which generate little distortion. Therefore, current optimization is done only for a modulation index range of $m = 0.5$ to $m = 1.25$.

The procedure for designing the controller starts in a very similar way to that of any other predictive controller: A system model needs to be defined for precalculations, control goals are being translated to an objective function and an optimization method shall be used to minimize the cost function.

5.1.1 System model

The stator equation is used for stator flux prediction:

$$\frac{d\boldsymbol{\psi}_\mathrm{s}}{dt} = R_\mathrm{s}\boldsymbol{i}_\mathrm{s} + \boldsymbol{u}_\mathrm{s}. \tag{5.1}$$

Considering the fact that current optimization is done only in a range of medium and high modulation indexes, the term $R_\mathrm{s}\boldsymbol{i}_\mathrm{s}$ in (5.1) can be neglected.

$$\frac{d\boldsymbol{\psi}_\mathrm{s}}{dt} = \boldsymbol{u}_\mathrm{s} \tag{5.2}$$

It shall be noted that the predicted stator flux will be used only for current distortion optimization. This simplification is equivalent to the assumption of having a highly inductive load when calculating OPPs, where the resistive part of the load was neglected as well.

As explained in section 4.4.2, quarter-wave and half-wave symmetries in a single-phase system turn to a $30°$ symmetry in a balanced three-phase system. Thus setting the prediction horizon t_ph equal to $30°$ or $1/12$ of the fundamental period is equivalent to setting it equal to the whole period. Therefore, $t_\mathrm{ph} = T_1/12$ is considered to be the prediction horizon. Besides, it is assumed that a finite number of switchings p are allowed to take place within the prediction horizon t_ph. This is shown in Figure 5.1 where the prediction horizon is divided into finite time intervals. No switching is allowed to take place during an interval. Conversely, when moving from one interval to an adjacent one, one switching will take place. Hence, the number of intervals defines the switching frequency.

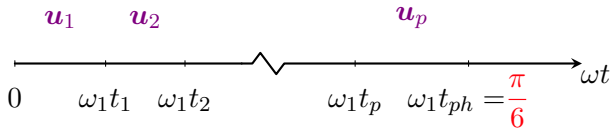

Figure 5.1: Prediction horizon

The stator flux trajectory can be predicted as follows:

$$\boldsymbol{\psi}_{s,p}(t) = \begin{cases} \boldsymbol{\psi}_s(0) + t \cdot \boldsymbol{u_1} & \text{for } t \le t_1, \\ \boldsymbol{\psi}_s(0) + t_1 \cdot \boldsymbol{u_1} + (t - t_1) \cdot \boldsymbol{u_2} & \text{for } t_1 \le t \le t_2, \\ \vdots & \\ \boldsymbol{\psi}_s(0) + t_1 \cdot \boldsymbol{u_1} + \cdots + (t - t_\mathrm{p}) \cdot \boldsymbol{u_p} & \text{for } t_p \le t \le t_\mathrm{ph}, \end{cases} \tag{5.3}$$

where p is the pulse number, $\boldsymbol{\psi}_s(0)$ is the stator flux estimation at the beginning of each $30°$ sector, $\boldsymbol{u_1}$ to $\boldsymbol{u_p}$ are the optimal voltage vector sequences at each operating point, $\boldsymbol{\psi}_{s,p}$ is the predicted value of the stator flux $\boldsymbol{\psi}_s$ and t_1 to t_p are the commutation times of the voltage vectors.

5.1.2 Objective function

The reference flux trajectory shall have a sinusoidal waveform with a constant amplitude. Therefore, a sinusoidal extrapolation of the flux reference at the beginning of each 30° section is assumed to be the flux reference in that section.

$$\boldsymbol{\psi}_s^*(t) = |\boldsymbol{\psi}_s^*|. \begin{bmatrix} cos(\omega_\mathrm{s} t) \\ sin(\omega_\mathrm{s} t) \end{bmatrix} \tag{5.4}$$

The objective function for minimizing the stator flux distortion, and hence the current distortion, is equivalent to the integral of the error between the predicted trajectories and the reference trajectory of the stator flux. So the objective function is introduced as follows:

$$\Gamma = \int_0^{t_\mathrm{ph}} (\boldsymbol{\psi}_{s,p}(t) - \boldsymbol{\psi}_s^*(t))\, dt. \tag{5.5}$$

The objective function can be divided into the sum of the errors of each switching interval as:

$$\begin{aligned} \Gamma &= \int_0^{t_\mathrm{ph}} (\boldsymbol{\psi}_{s,p}(t) - \boldsymbol{\psi}_s^*(t))\, dt \\ &= \int_0^{t_1} (\boldsymbol{\psi}_{s,p}(t) - \boldsymbol{\psi}_s^*(t))\, dt \\ &\quad + \int_{t_1}^{t_2} (\boldsymbol{\psi}_{s,p}(t) - \boldsymbol{\psi}_s^*(t))\, dt \\ &\quad + \cdots \\ &\quad + \int_{t_\mathrm{p}}^{t_\mathrm{ph}} (\boldsymbol{\psi}_{s,p}(t) - \boldsymbol{\psi}_s^*(t))\, dt. \end{aligned}$$

By defining an error matrix $\boldsymbol{R}$ as

$$\boldsymbol{R} = \begin{bmatrix} \int_0^{t_1} (\boldsymbol{\psi}_{s,p}(t) - \boldsymbol{\psi}_s^*(t))\, dt \\ \int_{t_1}^{t_2} (\boldsymbol{\psi}_{s,p}(t) - \boldsymbol{\psi}_s^*(t))\, dt \\ \vdots \\ \int_{t_\mathrm{p}}^{t_\mathrm{ph}} (\boldsymbol{\psi}_{s,p}(t) - \boldsymbol{\psi}_s^*(t))\, dt \end{bmatrix}, \tag{5.6}$$

the objective function can be defined as the second norm of the error matrix $\boldsymbol{R}$

$$J = \left\| \boldsymbol{R} \right\|_2^2. \tag{5.7}$$

The objective function (5.7) is a function of voltage vector sequences $\boldsymbol{u_1}$ to $\boldsymbol{u_p}$ and switching instances t_1 to t_p. The following two sections provide a procedure for selecting each of these sets in order to minimize the objective function.

Remark: Matrix $\boldsymbol{R}$ can be symbolically calculated using the `Symbolic Math Toolbox` of MATLAB. Each line of the matrix is a very long equation (with over a thousand characters). The length of the equations increases with the pulse number. The computational power of a ds1006 board from dSpace, which has a quad-core 2.8 GHz processor, made it possible to realize the optimization. However, matrix $\boldsymbol{R}_1$ is a good approximation of the error matrix $\boldsymbol{R}$ and can be used to reduce the requirements of the calculation resources:

$$\boldsymbol{R}_1 = \begin{bmatrix} \boldsymbol{\psi}_{s,p}(t_1) - \boldsymbol{\psi}_s^*(t_1) \\ \boldsymbol{\psi}_{s,p}(t_2) - \boldsymbol{\psi}_s^*(t_2) \\ \vdots \\ \boldsymbol{\psi}_{s,p}(t_{\mathrm{ph}}) - \boldsymbol{\psi}_s^*(t_{\mathrm{ph}}) \end{bmatrix}. \tag{5.8}$$

Instead of taking the integral of the flux error into account, matrix $\boldsymbol{R}_1$ uses the error value at the end of each switching interval.

5.1.3 Optimal voltage vector sequences

To achieve a synchronous modulation, the switching frequency needs to be set equal to a multiple of the fundamental frequency, $f_{\mathrm{sw}} = p \cot f_1$. In addition, setting the stator flux of an induction motor to a constant value keeps the proportion of the modulation index to the fundamental frequency constant.

$$\frac{m}{f_1} = 4\pi \frac{|\boldsymbol{\psi}_s|}{u_{\mathrm{dc}}} \tag{5.9}$$

Therefore, for an induction motor drive with constant flux and synchronous modulation, the switching frequency can be defined as:

$$f_{\mathrm{sw}} = k \cdot p \cdot m, \tag{5.10}$$

in which

$$k = \frac{u_{\mathrm{dc}}}{4\pi |\boldsymbol{\psi}_s|} \tag{5.11}$$

is a constant value, p the pulse number and m the modulation index.

Equation (5.10) defines f_{sw} against the modulation index lines for each pulse number p; however, the machine operates only in a segment of the line where:

$$p = \left\lfloor \frac{f_{\mathrm{sw,max}}}{k \cdot m} \right\rfloor. \tag{5.12}$$

$\lfloor \rfloor$ is the symbol for a floor function and $f_{\mathrm{sw,max}}$ is the maximum switching frequency.

Figure 5.2 shows the relationship between $f_{\mathrm{sw,max}}$, f_{sw}, the pulse number p and the modulation index m. As can be seen, pulse number being a fixed number in a synchronous modulation results in small changes in the switching frequency.

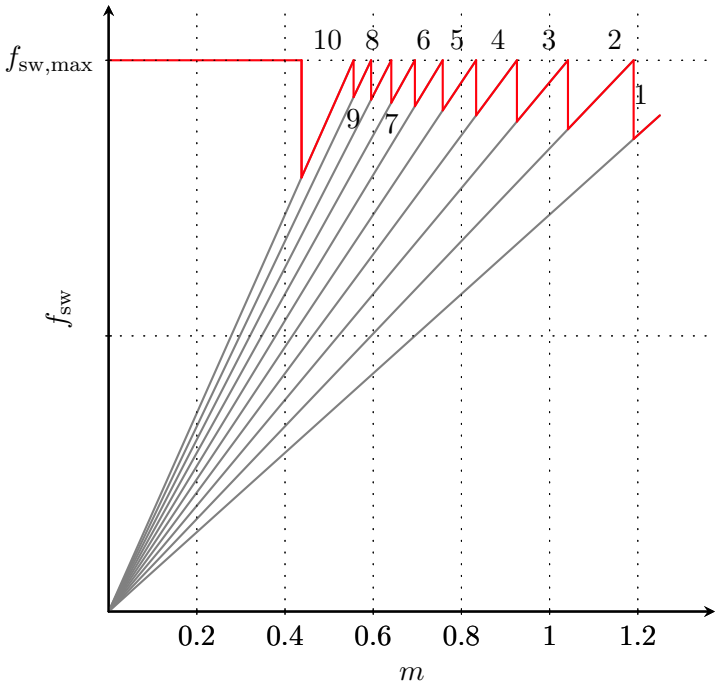

Figure 5.2: Switching frequency versus modulation index

By increasing the speed from 0 to nominal speed, the modulation index and the fundamental frequency increase as well. In low speed region, where the modulation index is low, any classical approach can be used to apply the pulses. The optimization is done for mechanical speeds $\omega_{\mathrm{m}} > 500\ \mathrm{rpm}$. In this region, the pulse number is defined by equation (5.12).

Based on equation (5.9), the relationship between the fundamental frequency and the modulation index is shown in Figure 5.3. The steady-state operating point is always located on this line. Considering the fact that the pulse number p is:

$$p = \left\lfloor \frac{f_{\mathrm{sw}}}{f_1} \right\rfloor, \tag{5.13}$$

the fundamental frequency axis can be divided into spans, each of which corresponds to a pulse number.

It was shown in the previous chapter that the modulation index can be divided into spans, in which a unique voltage vector sequence exists that results in less current distortion. Optimal voltage vector sequences for each pulse number and modulation index can be found in Appendix B.

For each pulse number span on the fundamental frequency axis, the modulation index axis can also be divided into spans corresponding to an optimal voltage vector sequence from the tables of Appendix B. As a result, optimal voltage vector sequence regions can be mapped onto

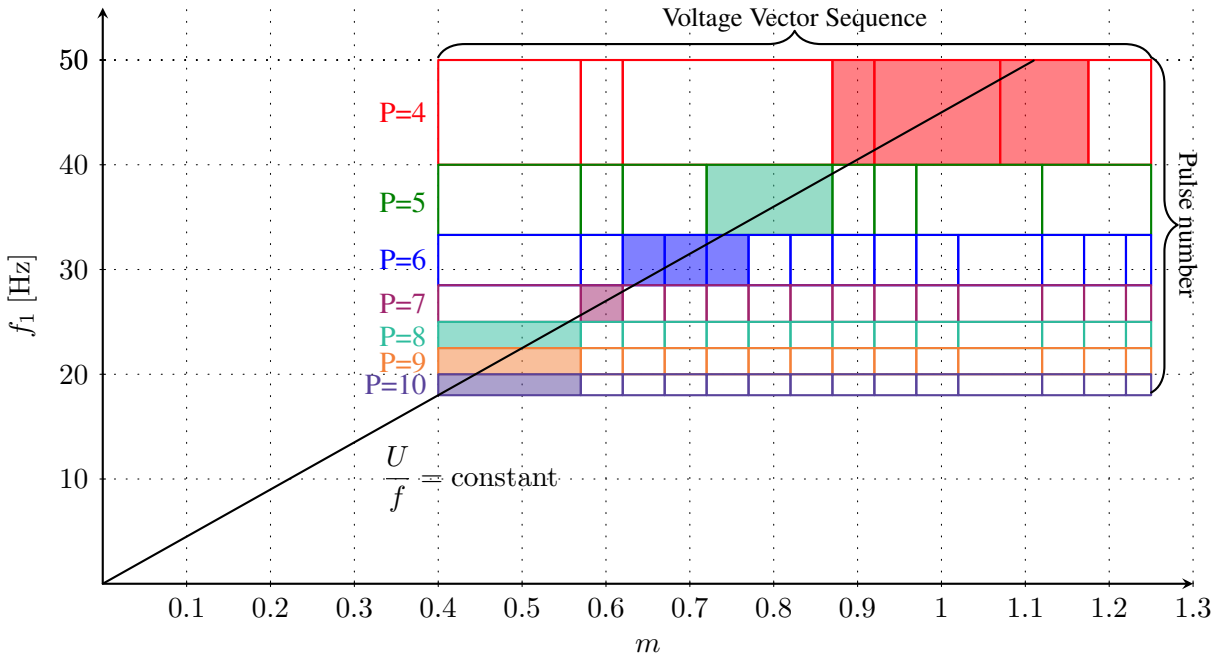

Figure 5.3: Fundamental frequency versus modulation index with optimal voltage vector sequence regions

the fundamental frequency versus the modulation index graph as well. An illustrative mapping is shown in Figure 5.3.

To define the voltage vector sequence that shall be used for the optimization, the following two steps shall be made:

1. The steady state operating point of the machine shall be defined on the line described in (5.9).

2. The region in which the steady state operating point is located defines the voltage vector sequence.

5.1.4 Online solver

The objective function (5.7) is a function of voltage vector sequences, $\boldsymbol{u_1}$ to $\boldsymbol{u_p}$, and switching instances, t_1 to t_p. Now that the voltage vector sequences are defined, switching times can be set to minimize the objective function.

The objective function (5.7) is a nonlinear function, hence one of the nonlinear numerical optimization techniques of section (3.1.4) can be used to find its optimum value. The main criterion for choosing a method is calculation time. In the following, it is explained why the convergence speed is not important in our case.

As the objective function is already a sum of squared function values, the Gauss-Newton method seems to be the best choice. In general, we are looking for a $\boldsymbol{T} \in \mathbb{R}^n$ that minimizes

$$J(\boldsymbol{T}) = \|\boldsymbol{R}(\boldsymbol{T})\|_2^2 = \sum_{i=1}^{m} r_i^2, \tag{5.14}$$

where $\boldsymbol{R}(\boldsymbol{T}) : \mathbb{R}^n \to \mathbb{R}^m$.
Given a starting guess $\boldsymbol{T}^{(n)} = [t_1, t_2, \ldots, t_m]^\top$, $\boldsymbol{R}(\boldsymbol{T})$ can be linearized near this initial value:

$$\boldsymbol{R}(\boldsymbol{T}) \approx \boldsymbol{R}(\boldsymbol{T}^{(n)}) + \nabla \boldsymbol{R}(\boldsymbol{T}^{(n)})(\boldsymbol{T} - \boldsymbol{T}^{(n)}), \tag{5.15}$$

where ∇ is the Jacobian. The elements (ij) of the Jacobian matrix are defined by:

$$(\nabla \boldsymbol{R})_{ij} = \frac{\partial \boldsymbol{R}_i}{\partial t_j}. \tag{5.16}$$

Thus:

$$\|\boldsymbol{R}(\boldsymbol{T})\|_2^2 = \|\boldsymbol{A}^{(n)}\boldsymbol{T} - \boldsymbol{B}^{(n)}\|_2^2, \tag{5.17}$$

where:

$$\begin{aligned}
\boldsymbol{A}^{(n)} &= \nabla \boldsymbol{R}(\boldsymbol{T}^{(n)}), \\
\boldsymbol{B}^{(n)} &= \nabla \boldsymbol{R}(\boldsymbol{T}^{(n)})\boldsymbol{T}^{(n)} - \boldsymbol{R}(\boldsymbol{T}^{(n)}).
\end{aligned}$$

and finally, the next iteration for this linearized least square problem is:

$$\boldsymbol{T}^{(n+1)} = \left(\boldsymbol{A}^{(n)\top}\boldsymbol{A}^{(n)}\right)^{-1}\boldsymbol{A}^{(n)\top}\boldsymbol{B}^{(n)}. \tag{5.18}$$

The online optimization is executed once at the beginning of each 30° sector with an initial guess, optimal voltage vector sequences, references, estimated stator flux and predicted values for that sector.

Remark: It is noteworthy that the optimization procedure starts with an initial guess. As the operating point does not change at steady-state operation, there are tiny variations in switching times from sector to sector. Hence, one can use the result of the optimization of a sector as an initial guess for the next sector. That is why convergence time is not very important for choosing a numerical optimization technique. Even though the optimization does not converge to the optimum point in the first sector, it will ultimately converge after solving the optimization for a few successive sectors.

5.1.5 Results of online optimization

It is necessary to analyze the performance of the online optimizer before taking further steps to design the whole control algorithm. Main benchmarks are calculation time and a comparison between the switching angles obtained from online and offline optimizations.

5.1.5.1 Calculation time

The online optimization algorithm is executed on the dSpace ds1006 processor board in real-time. The board is built around the AMD Opteron™, x86-compatible 64-bit server multi-core processor. It provides 512 kB of L2 cache per core and 6 MB of shared L3 cache. The ds1006 also has 1 GB of local memory for executing real-time models, 128 MB of global memory per core for exchanging data with the host PC, and 2 MB of on-board boot flash memory. One of the cores is assigned exclusively to the online optimization task.

Calculation time evidently increases with the number of iterations and the dimension of matrices. Matrix dimensions grow with the pulse number p. The calculation time is measured for the pulse number $p = 10$, which is the highest pulse number evaluated in this work, and a single iteration. Figure 5.4 shows the calculation time of each processor core in the dSpace Profiler window. It can be seen that the first core sends an interrupt via the IPI Block. This happens at the beginning of each $30°$ sector. Then the third core performs the online optimization, which shall be applied to the next $30°$ sector. The execution time is equal to $480\ \mu$s, which is still less than the length of a $30°$ sector at 500 rpm (5 ms).

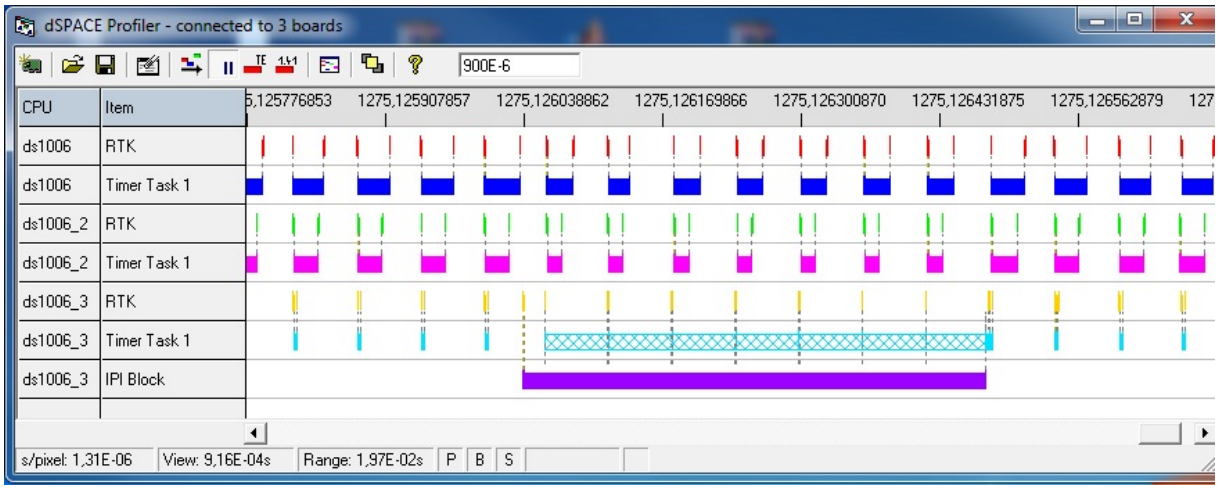

Figure 5.4: Online optimization calculation time for $p = 10$

5.1.5.2 Online results vs. offline results

Online optimization is used to calculate optimum switching times and current distortion at different operating points. The results are then compared with the results of the offline optimization from the previous chapter. Switching angles $\boldsymbol{\alpha}$ and the distortion of pulse patterns d are given in Tables (5.1) to (5.4) for $p = 2$, $p = 6$ and $p = 10$. Comparing the switching angles and pulse train distortion at different cases shows that the results of online and offline optimization are equivalent.

Table 5.1: Online and offline optimized switching angles for $p = 2$

$\boldsymbol{\alpha}$ $[rad]$	online	offline
1	0.063	0.063
2	0.356	0.353
d	0.1192	0.1185

m=0.95

Table 5.2: Online and offline calculated optimal firing angles for $p = 2$

$\boldsymbol{\alpha}$ $[rad]$	online	offline
1	0.133	0.135
2	0.303	0.304
d	0.1546	0.1545

m=0.71

Table 5.3: Online and offline optimized switching angles for $p = 6$

$\boldsymbol{\alpha}$ $[rad]$	online	offline
1	0.059	0.059
2	0.118	0.123
3	0.157	0.158
4	0.199	0.208
5	0.280	0.282
6	0.374	0.380
d	0.0759	0.0754

m=1.05

Table 5.4: Online and offline calculated optimal firing angles for $p = 10$

$\boldsymbol{\alpha}$ $[rad]$	online	offline
1	0.088	0.082
2	0.130	0.119
3	0.217	0.209
4	0.247	0.234
5	0.280	0.273
6	0.314	0.313
7	0.350	0.357
8	0.377	0.382
9	0.417	0.429
10	0.481	0.496
d	0.0565	0.0524

m=0.52

5.2 Transient response

The online optimization is executed at the beginning of each 30° sector. The optimal switching angles can then be applied as shown in Figure 5.5. In this way, although a very long prediction horizon is achieved, no receding horizon principle is applied. In order to apply the receding horizon policy, as depicted in Figure 5.6, one has to either increase the planning time or divide the action times into smaller intervals and repeat the optimization after each of them.

Planning is done for 30° of the fundamental period, which is equivalent to the whole period due to wave-form symmetries. As a result, increasing the prediction horizon to 60° or 90° is the same as solving a periodic problem in 2 or 3 cycles, and hence does not lead to any improvement. In addition, applying a part of the plan and re-planning from any point other than the corners of a 30° sector contradicts the synchronism of the switching and fundamental frequency. Note that a fixed switching frequency and a synchronous modulation-like behavior is achieved by setting the prediction horizon equal to 30° sectors. Considering these two points, the receding horizon policy cannot be applied to this optimization problem.

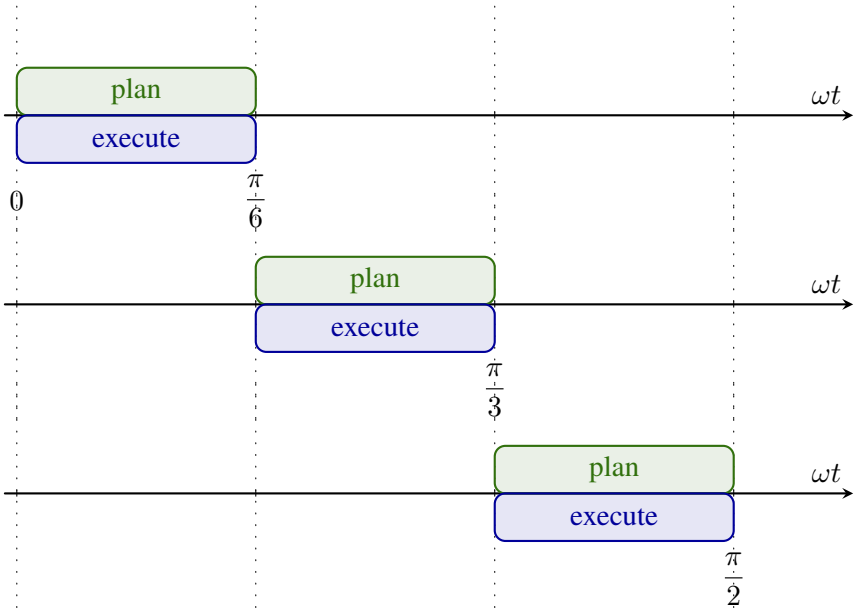

Figure 5.5: Long prediction horizon MPC without receiding horizon principle

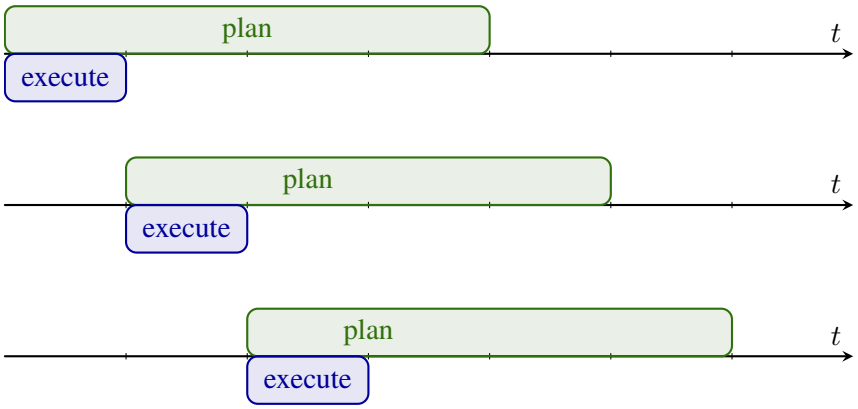

Figure 5.6: Principle of receding horizon

As explained in section (3.1.2), the receding horizon acts as feedback for the open-loop precalculations. Now that the receding horizon idea cannot be applied, an alternative solution has to be developed. Having no feedback within the $30°$ sectors leads to 2 problems. Firstly, the controller is blind to transients that take place during action intervals. This slows down the controller dynamics. Secondly, in quasi steady-state operation, the reference changes slightly all the time. Neglecting the reference changes for a long time leads to control variables diverging from reference values.

Figure 5.7 shows the measured steady-state flux error during online optimization. It can be seen that the error increases while the pulses are being applied. The error decreases immediately after re-optimizing the angles based on the actual measurements. Divergence of stator flux from its reference value is a drawback, which is a result of open-loop precalculations. As can be seen in Figure 5.7, under steady-state operating conditions, the stator flux error is small, typically around two percent of the flux magnitude (the stator flux magnitude is 0.8 Wb in this

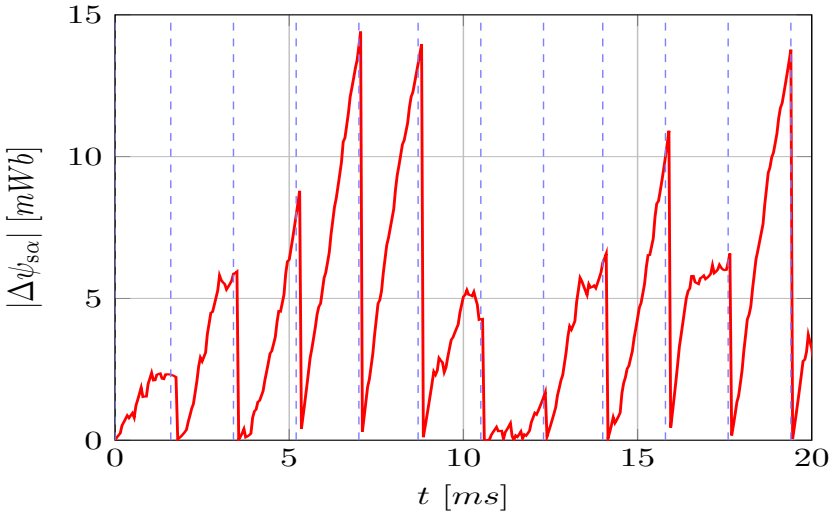

Figure 5.7: Stator flux error within each 30° interval

case). Therefore, only small corrections of the switching instants are required to remove the flux error over the horizon. As a result, optimized switching instances can be slightly shifted in time in order to compensate the steady-state error by moving around the precalculated optimal operating point.

5.2.1 Pulse modification

The objective of pulse modification is to adjust the switching angles in order to regulate the stator flux vector along its given reference trajectory. For example in phase a, shifting a switching instance by the time Δt_a changes the stator flux by the amount of

$$\Delta\boldsymbol{\psi}_{\mathrm{s,a}}\left(\Delta t_a\right) = -\frac{u_{\mathrm{dc}}}{2} s(i) \Delta t_a, \tag{5.19}$$

where $s(i)$ being 1 denotes a switching transition to an upper level, $s(i)$ being -1 denotes a switching transition to a lower level and $\Delta t_a = t_a - t_{a,\mathrm{opt}}$. t_a is the modified and $t_{a,\mathrm{opt}}$ the precalculated switching instances.

5.2.1.1 Flux trajectory error

Pulse modification is performed based on stator flux trajectory tracking. The stator flux error is introduced as

$$\boldsymbol{\psi}_{s,\mathrm{error}} = \boldsymbol{\psi}_s^* - \boldsymbol{\psi}_s, \tag{5.20}$$

where $\boldsymbol{\psi}_s^*$ is the stator flux reference and $\boldsymbol{\psi}_s$ is the estimated stator flux. The stator flux reference is generated by integrating the precalculated optimal pulse pattern

$$\boldsymbol{\psi}_s^* = \int_0^\theta \boldsymbol{u}_{\mathrm{opt}} \mathrm{d}\omega t + \boldsymbol{\psi}_s^*(0), \tag{5.21}$$

where $\boldsymbol{u}_{\mathrm{opt}}$ is the optimal voltage. According to equation (2.4), the reference displacement angle can be calculated based on the reference torque and stator flux as

$$\delta^* = \sin^{-1}\left(\mathrm{k}_\delta \frac{\mathrm{T}^*}{|\boldsymbol{\psi_r}||\boldsymbol{\psi_s}|}\right), \tag{5.22}$$

where $k_\delta = \frac{2}{3}\frac{\sigma L_\mathrm{s} L_\mathrm{r}}{P L_\mathrm{m}}$. Thus the stator flux reference angle $\measuredangle \boldsymbol{\psi}_s^*$ is

$$\measuredangle \boldsymbol{\psi}_s^* = \measuredangle \boldsymbol{\psi}_r + \delta^*. \tag{5.23}$$

The integral in (5.21) is calculated over the interval $[0; \theta]$. θ is set to the angle of the reference flux $\measuredangle \boldsymbol{\psi}_s^*$. The resulting instantaneous reference flux vector slightly differs in magnitude and angle from its respective value on the unitary circle. It is a reference flux trajectory obtained from the precalculated voltage waveforms and it has the exact value of volt-seconds corresponding to the reference torque. If the error between the reference flux trajectory, $\boldsymbol{\psi}_s^*$ and the estimated flux, $\boldsymbol{\psi}_s$ is zero, it means that the machine is tracking the optimal flux trajectory and generating the reference torque as well. Otherwise, there is an error that needs to be compensated. This error might be a transient error, which initiates from a change in the voltage vector sequences, or a quasi steady-state error as shown in Figure 5.7.

5.2.1.2 Stator flux error compensation

A deadbeat controller is used to minimize the error $\boldsymbol{\psi}_{s,\mathrm{error}}$ in real-time. It is based on the trajectory tracking approach used in Model Predictive Pulse Pattern Control (MP3C) [36, 37]. For this purpose, an objective function J_{ss} is introduced as

$$J_{\mathrm{ss}} = \left(\boldsymbol{\psi}_{s,\mathrm{error}} - \boldsymbol{\psi}_{s,\mathrm{corr}}(\Delta \boldsymbol{t})\right)^2, \tag{5.24}$$

where $\boldsymbol{\psi}_{s,\mathrm{error}}$ is the stator flux error vector, $\boldsymbol{\psi}_{s,\mathrm{corr}}$ the necessary correction for the stator flux and $\Delta \boldsymbol{t}$ defines the vector of switching instant corrections. The stator flux correction is calculated based on equation (5.19)

$$\boldsymbol{\psi}_{s,\mathrm{corr}}(\Delta \boldsymbol{t}) = -\frac{u_\mathrm{dc}}{2}\boldsymbol{P}\begin{bmatrix}\sum_i s_a(i)\Delta t_{ai}\\ \sum_i s_b(i)\Delta t_{bi}\\ \sum_i s_c(i)\Delta t_{ci}\end{bmatrix}, \tag{5.25}$$

where $\boldsymbol{P}$ is the Clarke transformation matrix (2.8). Matrix $\boldsymbol{\psi}_{s,\mathrm{corr}}$ provides the added volt-seconds to the stator flux trajectory by changing the switching instances. As a result, the remaining task is to find a correction time vector $\Delta \boldsymbol{t}$ that minimizes the objective function (5.24). To do so, the following steps shall be made [37]

1. Determine the two phases with the next switching transitions. For instance, if phase a and b have the next switching transitions, they would be the active phases.

2. Translate the flux error from $\alpha\beta$ to abc coordinates by mapping it into the two active phases. For the example given, the mapping is done as $\boldsymbol{\psi}_{s,abc,\mathrm{error}} = \boldsymbol{P}_{ab}^{-1}\boldsymbol{\psi}_{s,\mathrm{error}}$, where

$$\boldsymbol{P}_{ab}^{-1} = \begin{bmatrix} \frac{3}{2} & \frac{\sqrt{3}}{2} \\ 0 & \sqrt{3} \\ 0 & 0 \end{bmatrix}. \tag{5.26}$$

3. Compute the required modification of the switching instants in abc coordinates

$$\Delta\boldsymbol{t}_{\mathrm{req}} = \frac{2}{u_{\mathrm{dc}}}\boldsymbol{\psi}_{s,abc,\mathrm{error}}. \tag{5.27}$$

4. Go through all switching transitions of the first active phase. For the ith switching transition in phase x, $x \in \{a, b, c\}$, with the precalculated switching instance $t_{xi,\mathrm{opt}}$ and the switching transition $s_x(i)$, perform the following operations

   - Compute the desired modification in a deadbeat way: $\Delta t_{xi} = \Delta\boldsymbol{t}_{\mathrm{req}}/(-s_x(i))$.
   - Modify the switching instant: $t_{xi} = t_{xi,\mathrm{opt}} + \Delta t_{xi}$.
   - Impose the respective constraint on the switching instant. Consider that each switching instant is smaller than the next and bigger than the previous one.
   - Update the phase x component of the required switching instant modification by replacing $\Delta t_{x,\mathrm{req}}$ with $\Delta t_{x,\mathrm{req}} = (t_{xi} - t_{xi,\mathrm{opt}})(-s_x(i))$.

5. Repeat the above procedure for the second active phase.

The block diagram of the pulse modification is illustrated in Figure 5.8. It is worth mentioning that the pulse modification algorithm described above is, apart from a small modification, the same as the flux trajectory tracking algorithm presented in [36, 37]. The only difference lies in the calculation of equation (5.21). In [36, 37], flux trajectory tracking control is applied in order to operate offline calculated OPPs in a closed-loop control. As the switching angles were already available, the reference flux trajectory was calculated offline by integrating the respective OPPs over $90°$ of the fundamental voltage waveform. The result of this integration procedure was a set of corner points corresponding to a switching transition in the OPP. These corner points were stored in a look-up table along with the OPPs. Therefore, two look-up tables - one for switching instances and one for optimal flux trajectories - were needed for the closed-loop operation of OPPs. In contrary, online optimization does not have the information regarding switching instances in advance. As a result, the integration in (5.21) shall be calculated online as well.

The integration of the voltage waveform turns into the multiplication of voltage levels with their precalculated durations, which can be calculated very fast in real-time.

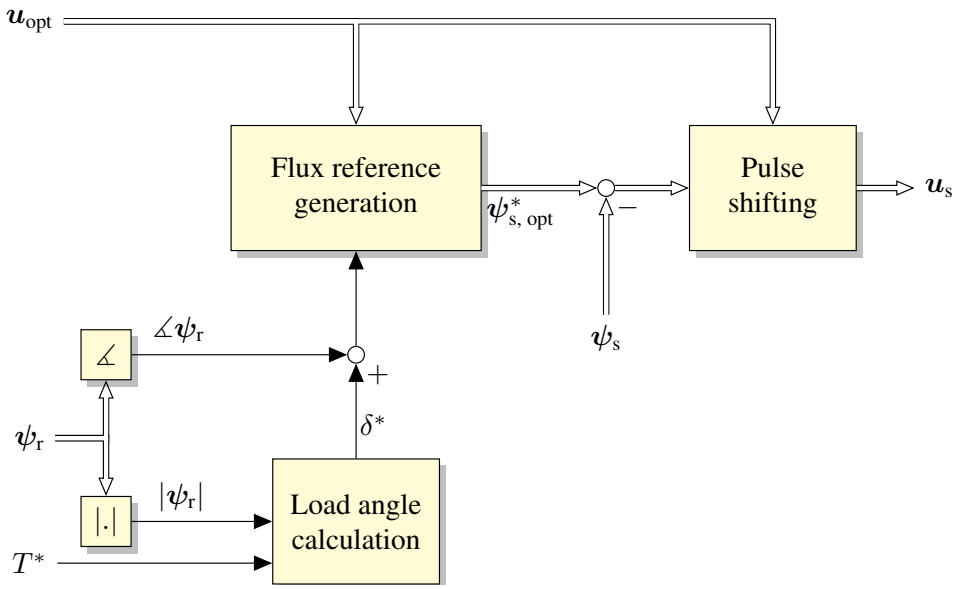

Figure 5.8: Block diagram of the pulse shifting algorithm

5.3 Measurement Results

Figure 5.9 shows the block diagram of online current distortion optimization scheme. At first, the stator and rotor fluxes are estimated. The rotor flux is used to calculated the reference synchronous speed ω_{s}^*, and the stator flux is used to generate the trigger signals whenever the voltage vector crosses the corner of a 30° sector. Online optimization is executed once after each trigger signal and the results are sent to the pulse modification block. Finally, the pulses are adjusted in real-time based on the stator flux trajectory control scheme, and the gate signals are applied to the converter.

The low-voltage AC-drive of the experimental setup is tested in various operating points in order to evaluate the closed-loop performance of the online optimization. The maximum device switching frequency is considered to be 200 Hz. The pulse number p at each operating point is calculated based on the equation (5.11). Therefore, pulse number $p = 4$ is applied at $w_{\text{m}} = 1450$ rpm, pulse number $p = 8$ is applied at $w_{\text{m}} = 750$ rpm and pulse number $p = 10$ is applied at $w_{\text{m}} = 600$ rpm.

A torque step is applied to the machine at $w_{\text{m}} = 1450$ rpm and at $w_{\text{m}} = 600$ rpm and the stator current trajectories during the transients are shown in Figures 5.10 and 5.11 respectively. The stator current trajectories in $\alpha\beta$ coordinates show that the controller exhibits a deadbeat behavior during the transients. Besides, torque responses are shown in Figures 5.12 and 5.13. The transient operation demonstrates that neither the operation at a very low device switching frequency of 200 Hz nor current distortion optimization has led to sacrifices on system dynamics.

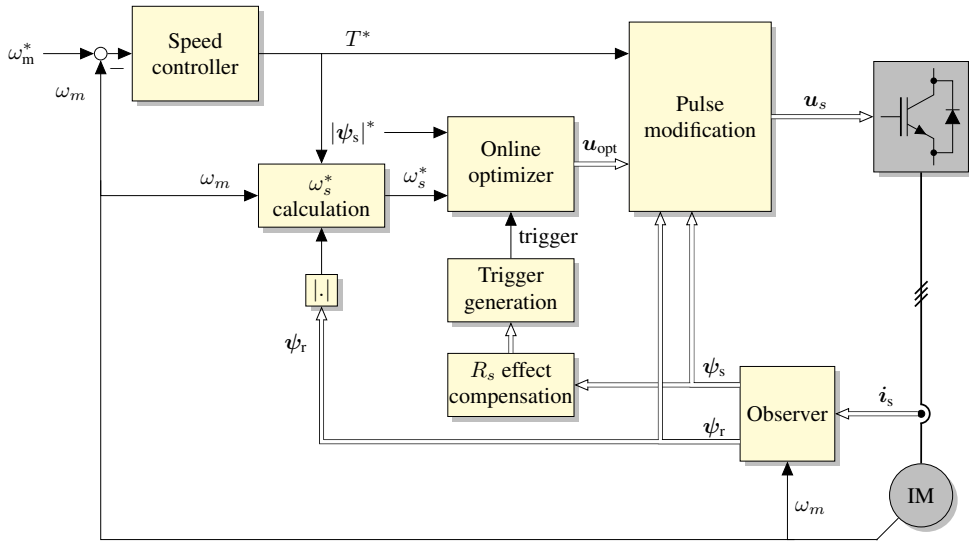

Figure 5.9: Block diagram of online current distortion optimization scheme

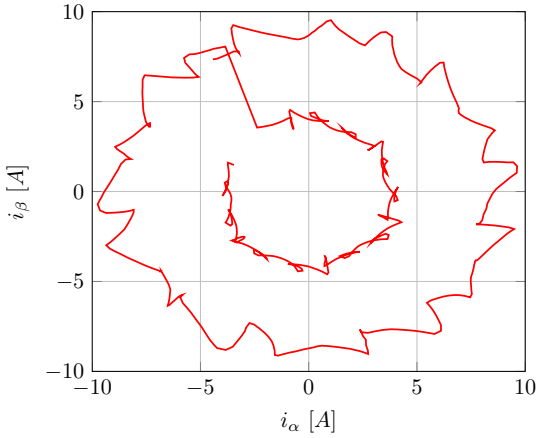

Figure 5.10: Stator current trajectory during a torque step change at $\omega_\mathrm{m} = 1450$ rpm

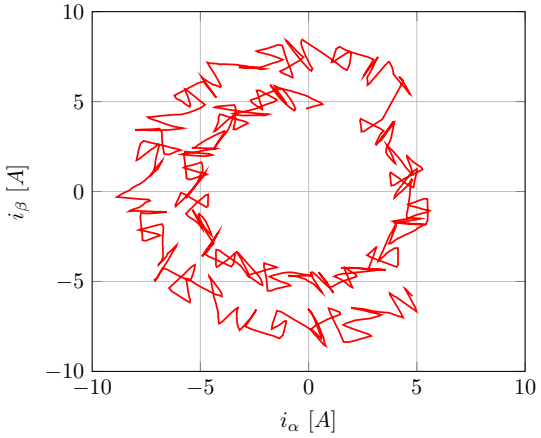

Figure 5.11: Stator current trajectory during a torque step change at $\omega_\mathrm{m} = 600$ rpm

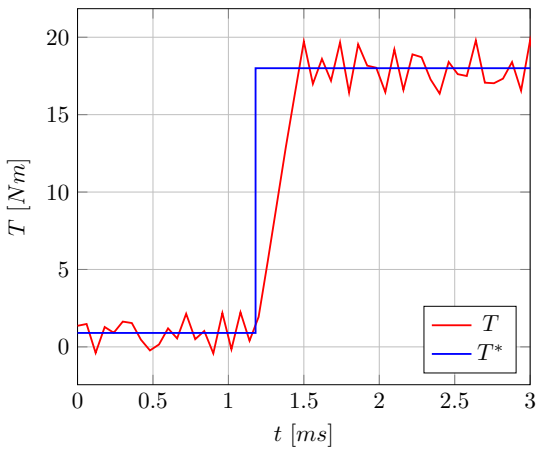

Figure 5.12: Electromagnetic torque response at $\omega_\mathrm{m} = 1450$ rpm

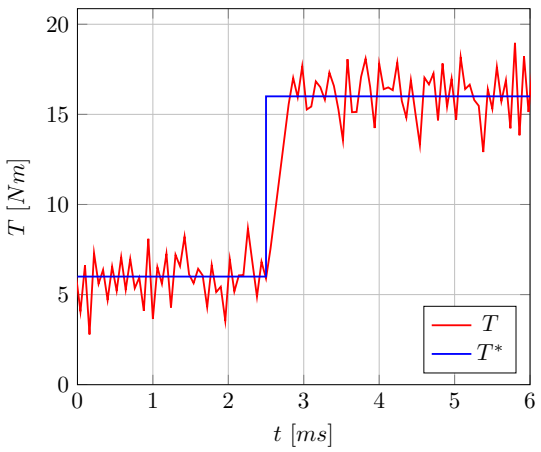

Figure 5.13: Electromagnetic torque response at $\omega_\mathrm{m} = 600$ rpm

Steady-state tests are performed at the three different speeds $\omega_{\mathrm{m}} = 1450$ rpm, $\omega_{\mathrm{m}} = 750$ rpm and $\omega_{\mathrm{m}} = 600$ rpm. The phase voltages are shown in Figures 5.15, 5.17 and 5.19. It can be seen that the voltage waveforms display half-wave and quarter-wave symmetries. This illustrates that the online optimized angles, which are calculated for each 30° sector, do not change in steady-state operation mode. A main concern about online calculation is to ensure that there is no oscillation on switching angles. This has been testified by operating the machine at various transient and steady-state conditions. The investigation does not show any problem in this regard. However, it must be noted that it is not mathematically proven that the distortion function at each voltage vector sequence is convex and stability is demonstrated via several experiments in the same way as for most available MPC schemes.

Figures 5.14, 5.16 and 5.18 display the steady-state stator current waveforms. They also show

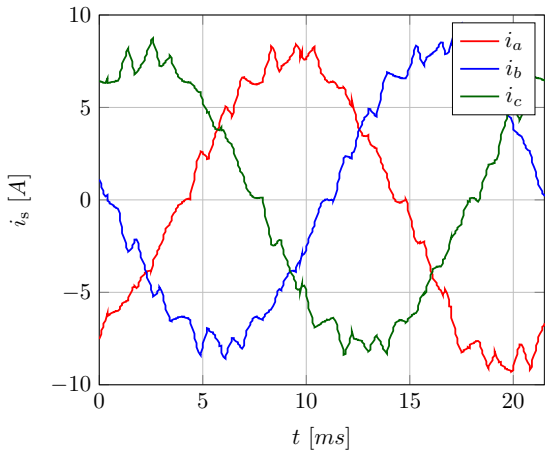

Figure 5.14: Steady-state stator currents at $\omega_{\mathrm{m}} = 1450$ rpm and $p = 4$

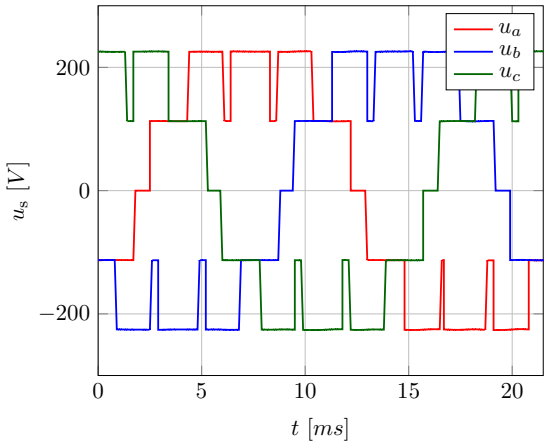

Figure 5.15: Steady-state phase voltages at $\omega_{\mathrm{m}} = 1450$ rpm and $p = 4$

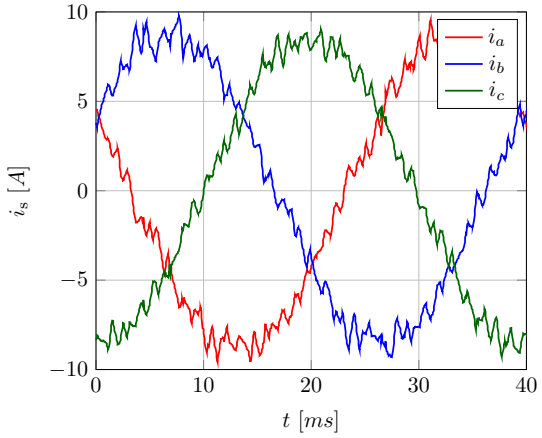

Figure 5.16: Steady-state stator currents at $\omega_{\mathrm{m}} = 750$ rpm and $p = 8$

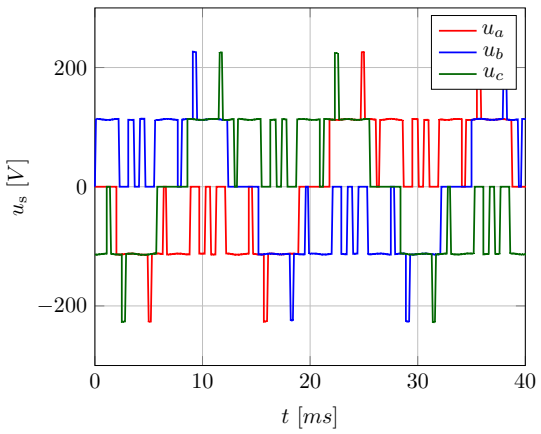

Figure 5.17: Steady-state phase voltages at $\omega_{\mathrm{m}} = 750$ rpm and $p = 8$

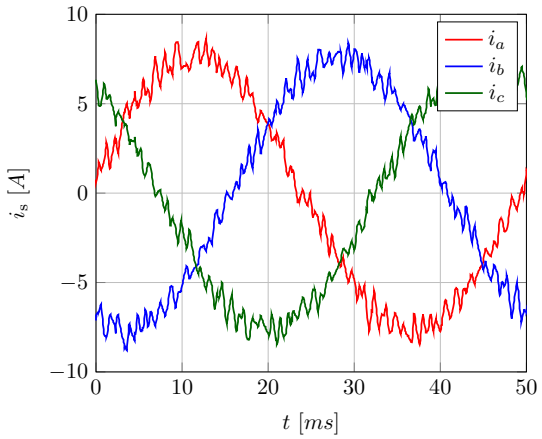

Figure 5.18: Steady-state stator currents at $\omega_{\mathrm{m}} = 600$ rpm and $p = 10$

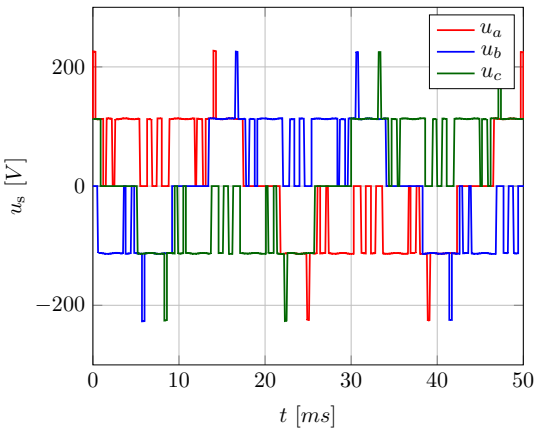

Figure 5.19: Steady-state phase voltages at $\omega_{\mathrm{m}} = 600$ rpm and $p = 10$

a very low distorted current despite the low switching frequency. Comparing the distortion of measured currents can be misleading. This originates from the fact that the current distortion does not only depend on the switching angles, but on the whole voltage waveform. The voltage waveform of a multilevel converter is constructed from the DC-link voltage and flying capacitors voltages. Considering the ripple on the flying capacitor and the DC-link voltage, the voltage vectors in the $\alpha\beta$ hexagon are not located exactly on the fixed points, but oscillate in a boundary. As a result, in some cases the actual applied voltage is located in a position that leads to a distortion that is slightly smaller than expected, and in most cases to a slightly bigger one.

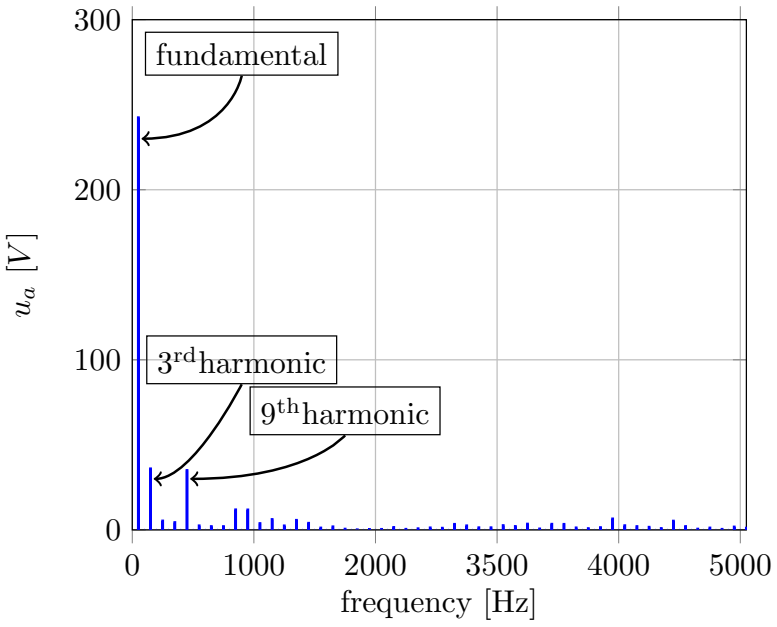

Figure 5.20: Harmonic spectrum of u_a at $p = 4$

Taking this into the account, it is more meaningful to compare the results where this uncertainty does not exists as in Tables (5.1) to (5.4).

Figure 5.20 illustrates the harmonic spectrum of the phase voltage with $p = 4$ - shown in Figure 5.15. As can be seen the 3rd and 9th harmonics have a relatively high value. Besides, some of the harmonics of high orders have a slightly higher values. These observations fit well with the fact that a good modulation scheme puts as much energy as possible on triplen harmonics and pushes the rest of the signal energy to higher harmonics. It is noteworthy that such a behavior is achieved in OPPs by omitting the triplen harmonics from $\boldsymbol{H}$ and weighting the harmonics in the distortion function. However, the harmonic spectrum is shaped in a predictive-based controller only by considering the stator flux trajectory error in the objective function with a long prediction horizon.

Remark: A flying capacitor converter gives a full degree of freedom to balance the flying capacitor voltages. As explained in Chapter 2, voltage balancing can be easily achieved by using per-phase redundancies. As a result, it is not necessary to include the capacitor voltage balancing in the problem formulation. The applied voltage balancing algorithm is explained in Appendix C. If an NPC or an ANPC converter is used, joint-phase redundancies have to be considered for voltage balancing. In this case, voltage balancing affects the optimization results and needs to be considered as in [102].

CHAPTER 6

Conclusion

This work shows that with a good problem formulation and by applying several ideas, some of which already known in optimal control theory contexts, one can immensely increase the speed of solving optimization problems for electrical drives.

The current distortion optimization problem was chosen to be studied for an induction motor drive. A 5-level inverter was chosen as the power converter due to the fact that distortion optimization gets more complicated and time consuming for multilevel inverters. Based on an extensive literature study, synchronous optimal modulation was chosen as a reference due to its superior performance at low switching frequencies. Then a step-by-step approach was followed to study the current distortion, define the criteria for its optimality, increase the speed of offline optimization and finally apply the ideas from predictive control theory in order to achieve an online optimization.

In the first place, the theoretical analysis of current distortion optimization in the $\alpha\beta$ coordinate system revealed the relationship between voltage vector sequences of a converter and its current distortion. Based on experimental results, it has been reported that by limiting the switchings to transitions between adjacent voltage vectors, the current distortion decreases [98]. This analysis provides an analytical proof for this statement. In addition, this piece of information made it possible to break down the complicated global current optimization problem to several simpler ones. As a result, a significant improvement was achieved in offline calculation speed.

In the next step, the current distortion was formulated as an objective function of a predictive controller. The prediction horizon was set to be equal to 30° of the fundamental waveform period. It was known from previous studies that certain voltage vector sequences cause less current distortion. So the objective function optimization became a continuous optimization of switching intervals rather than a successive search for voltage vectors that correspond to the minimum value of the objective function. The continuous optimization problem was finally solved by a modified Gauss-Newton algorithm.

Finally, based on measurements at different operating points it was shown that the results of

online and offline optimizations are comparable.

The results of this work and some other recent studies on fast optimization techniques [103] alongside the fact that calculation power is rapidly increasing imply that many optimal control strategies that were traditionally used for systems with slow dynamics can now, or very soon, be used for electrical drives in real-time.

After all, it should be noted that the word optimum must be used with extreme caution since it always implies a set of assumptions that are sometimes neglected. For example, in current distortion optimization, all switching instances are calculated assuming that an ideal converter with ideal switches and without any losses, dead-time effect, capacitor voltage ripple etc. is available. Besides, even harmonics are considered to be absent due to symmetries - which is not the case in practice. The question how the true optimum can be reached is still unanswered, which shows that much work, both practical and theoretical, remains to be done in this area.

APPENDIX A

List of symbols and abbreviations

A.1 List of symbols

Used symbols:
In the following the most important symbols are listed which are used within this work.

General symbols:

$\boldsymbol{x}$	State vector
$\boldsymbol{u}$	Input vector
$\boldsymbol{y}$	Output vector
t	Time (continuous)
k	Time (discrete, current sample)
$\frac{\mathrm{d}}{\mathrm{d}t}$	Time derivation
T_s	Sampling time
Δ	Difference
∇	Jacobian

General electrical variables:

a, b, c	Phases
α, β	Equivalent two-phase coordinates
j	$\sqrt{-1}$
u	Voltage
i	Current
R	Resistor
C	Capacitor
L	Inductor

Induction machine parameters:

$\boldsymbol{u}_\mathrm{s}$, $\boldsymbol{u}_\mathrm{r}$	Stator and rotor voltage vectors
$\boldsymbol{i}_\mathrm{s}$, $\boldsymbol{i}_\mathrm{r}$	Stator and rotor current vectors
$\boldsymbol{\psi}_\mathrm{s}$, $\boldsymbol{\psi}_\mathrm{r}$	Stator and rotor flux vectors
ω_m	Mechanical machine speed
ω_s	Synchronous speed
T	Mechanical torque
P	Number of pole pairs
R_s, R_r	Stator and rotor resistance
L_s, L_r	Stator and rotor inductance
L_m	Mutual inductance

A.2 List of abbreviations

AC	Alternating Current
A/D	Analog to Digital
AFE	Active Front End
ANPC	Active Neutral-Point Clamped
CHB	Connected H-Bridge
DC	Direct Current
DCC	Diode-Clamped Converter
DSC	Direct Self Control
DTC	Direct Torque Control
FC	Flying Capacitor
FCS-MPC	Finite Control Set Model Predictive Control
FOC	Field Oriented Control
HVDC	High Voltage Direct Current
IGBT	Insulated Gate Bipolar Transistor
IGCT	Integrated Gate-Commutated Thyristor
IM	Induction Machine, Induction Motor
LP	Linear Program
LTI	Linear Time-Invariant
LQR	Linear Quadratic Regulator
MIMO	Multi Input Multi Output
MLC	Multilevel Converter
MOSFET	Metal–Oxide–Semiconductor Field-Effect Transistor
MPC	Model Predictive Control
MV	Medium Voltage
NPC	Neutral-Point Clamped
OPP	Optimal Pulse Pattern
OSVM	Optimal Space Vector Modulation
PWM	Pulse Width Modulation
QP	Quadratic Program
REC	Receding Horizon Control
RMS	Root Mean Square
RPM	Revolutions Per Minute
SCHB	Series Connected H-Bridge
SHE	Selective Harmonic Elimination
SOM	Synchronous Optimal Modulation
SPWM	Sinusoidal Pulse Width Modulation
SVM	Space Vector Modulation
THD	Total Harmonic Distortion
VSI	Voltage Source Inverter
WTHD	Weighted Total Harmonic Distortion

APPENDIX B

Tables of Optimal Pulse Patterns

Table B.1: Optimization results for $p = 2$

m	0,50	0,55	0,60	0,65	0,70	0,75	0,80	0,85	0,90	0,95	1,00	1,05	1,10	1,15	1,20	1,25
$\boldsymbol{\alpha}$	0,820	0,778	0,275	0,757	0,747	0,712	0,647	0,528	0,415	0,353	0,301	0,244	0,178	0,132	0,134	0,127
	1,468	1,419	1,551	1,272	1,196	1,136	1,094	1,080	1,049	0,984	0,907	0,825	0,732	0,618	0,465	0,239
Structure	1	1	2	1	1	1	1	1	1	1	1	1	1	1	1	1
Vector sequence	B10	B10	B10	B10	B10	B10	B10	B10	B10	D19	D19	D19	D19	D19	D19	D19
	A6	A6	B11	C15	C15	C15	C15	C15	C15	C15	C15	C15	D20	D20	D20	D20
	B11	B11	A6	B11	B11	B11	B11	B11	C16	C16	C16	C16	C16	C16	D21	D21
d	0,192	0,169	0,128	0,158	0,154	0,163	0,203	0,234	0,144	0,120	0,206	0,267	0,227	0,150	0,136	0,529

Table B.2: Optimization results for $p = 3$

m	0,50	0,55	0,60	0,65	0,70	0,75	0,80	0,85	0,90	0,95	1,00	1,05	1,10	1,15	1,20	1,25
$\boldsymbol{\alpha}$	0,834	0,792	0,230	0,292	0,307	0,331	0,354	0,368	0,368	0,067	0,109	0,143	0,155	0,150	0,140	0,127
	1,398	1,362	0,350	1,167	1,162	1,141	1,110	1,073	1,032	0,352	0,320	0,315	0,343	0,389	0,418	0,238
	1,512	1,526	0,432	1,235	1,317	1,385	1,445	1,495	1,539	1,111	1,189	1,275	1,367	1,463	1,552	1,571
Structure	1	1	2	1	1	1	1	1	1	1	1	1	1	1	1	1
Vector	B10	B10	B10	B10	B10	B10	B10	B10	D19	D19	D19	D19	D19	D19	D19	D19
sequence	A6	A6	B11	C15	C15	C15	C15	C15	C15	C14	D20	D20	D20	D20	D20	D20
	B11	B11	B10	B10	B10	C16	C16	C16	C16	C15	C15	C15	C15	D21	D21	D21
	A6	A6	B11	B11	B11	B11	B11	B11	B11	C16	C16	C16	C16	C16	C16	C16
d	0,164	0,130	0,103	0,102	0,133	0,162	0,156	0,117	0,082	0,120	0,196	0,239	0,219	0,130	0,114	0,530

Table B.3: Optimization results for $p = 4$

m	0,50	0,55	0,60	0,65	0,70	0,75	0,80	0,85	0,90	0,95	1,00	1,05	1,10	1,15	1,20	1,25
$\boldsymbol{\alpha}$	0,342	0,312	0,197	0,118	0,738	0,627	0,075	0,357	0,050	0,351	0,297	0,098	0,109	0,154	0,141	0,089
	0,792	0,813	0,274	0,304	1,112	0,697	0,714	1,067	0,364	0,900	0,691	0,669	0,638	0,504	0,411	0,122
	0,901	0,864	0,355	0,912	1,184	0,781	0,998	1,434	1,062	0,940	0,761	1,159	1,182	0,592	0,487	0,160
	1,496	1,522	1,557	1,252	1,272	1,132	1,525	1,520	1,538	1,022	0,966	1,297	1,256	0,687	0,532	0,234
Structure	4	4	4	1	3	2	3	3	1	3	3	3	3	3	3	2
Vector sequence	B10	B10	B10	B10	B10	B10	B10	B10	D19	D19	D19	D19	D19	D19	D19	D19
	A6	A6	B11	B11	C15	C15	C14	C15	C14	C15	C15	D20	D20	D20	D20	D20
	B10	B10	B10	C15	B10	B11	C15	C16	C15	D19	D19	C15	C15	C16	D21	D19
	B11	B11	B11	B10	C15	C15	B11	B11	C16	C15	D20	D20	D20	D20	D20	D20
	A6	A6	A6	B11	B11	B11	C16	C16	B11	C16	C16	C16	C16	D21	C16	D21
d	0,120	0,109	0,081	0,097	0,098	0,128	0,117	0,093	0,074	0,099	0,115	0,106	0,108	0,096	0,113	0,529

Table B.4: Optimization results for $p = 5$

m	0,50	0,55	0,60	0,65	0,70	0,75	0,80	0,85	0,90	0,95	1,00	1,05	1,10	1,15	1,20	1,25
$\boldsymbol{\alpha}$	0,308	0,294	0,183	0,244	0,239	0,242	0,432	0,055	0,051	0,060	0,231	0,096	0,114	0,134	0,100	0,089
	0,843	0,848	0,245	0,313	0,686	0,632	0,668	0,698	0,360	0,376	0,367	0,382	0,396	0,406	0,139	0,122
	0,926	0,887	0,323	0,360	0,756	0,734	0,750	1,032	1,064	1,081	0,828	1,152	1,196	1,267	0,176	0,160
	1,416	1,448	0,435	1,161	1,116	1,105	1,096	1,451	1,494	1,256	0,982	1,280	1,280	1,305	0,415	0,234
	1,520	1,512	0,479	1,233	1,205	1,259	1,515	1,536	1,529	1,291	1,354	1,416	1,462	1,503	1,551	1,571
Structure	4	4	4	2	3	3	2	3	1	3	3	3	3	3	2	2
Vector	B10	B10	B10	B10	B10	B10	B10	B10	D19	D19	D19	D19	D19	D19	D19	D19
sequence	A6	A6	B11	C15	C15	C15	C15	C14	C14	C14	C15	D20	D20	D20	D20	D20
	B10	B10	B10	B10	B10	B10	B11	C15	C15	C15	D19	C15	C15	C15	D19	D19
	B11	B11	B11	B11	B11	B11	C15	B11	C16	D20	D20	D20	D20	D20	D20	D20
	A6	A6	B10	B10	C15	C15	C16	C16	B11	C15	C15	C15	D21	D21	D21	D21
	B11	B11	B11	B11	B11	B11	B11	B11	C16	C16	C16	C16	C16	C16	C16	C16
d	0,097	0,094	0,077	0,076	0,080	0,115	0,105	0,077	0,067	0,083	0,089	0,103	0,099	0,076	0,109	0,529

Table B.5: Optimization results for $p = 6$

m	0,50	0,55	0,60	0,65	0,70	0,75	0,80	0,85	0,90	0,95	1,00	1,05	1,10	1,15	1,20	1,25
$\boldsymbol{\alpha}$	0,296	0,257	0,205	0,215	0,662	0,219	0,077	0,057	0,055	0,286	0,179	0,159	0,118	0,136	0,100	0,071
	0,861	0,347	0,280	0,353	0,708	0,691	0,658	0,404	0,314	0,342	0,680	0,667	0,547	0,399	0,138	0,090
	0,936	0,657	0,356	0,772	0,781	0,795	0,745	0,694	0,360	0,406	0,894	0,923	0,597	1,259	0,176	0,122
	1,384	0,864	1,146	1,131	1,108	1,091	0,801	0,743	0,415	0,874	0,999	0,988	0,678	1,290	0,407	0,150
	1,460	0,900	1,157	1,179	1,182	1,209	1,010	1,035	1,061	0,917	1,268	1,256	1,193	1,464	0,485	0,174
	1,534	1,497	1,547	1,347	1,273	1,547	1,531	1,530	1,543	1,021	1,376	1,330	1,268	1,540	0,531	0,232
Structure	8	4	2	3	6	7	7	3	3	6	7	7	7	7	6	4
Vector	B10	B10	B10	B10	B10	B10	B10	B10	D19	D19	D19	D19	D19	D19	D19	D19
sequence	A6	A6	C15	C15	C15	C15	C14	C14	C14	C15	C15	C15	D20	D20	D20	D20
	B10	B10	B10	B10	B10	B10	C15	C15	C15	D19	D19	D19	C15	C15	D19	D19
	B11	B11	B11	B11	C15	B11	B11	B11	C16	C15	D20	D20	D20	D20	D20	D20
	A6	B10	B10	C15	B11	C15	C15	C15	C15	C16	C15	C15	C16	D21	D21	D19
	B11	A6	B11	B10	C15	B11	B11	C16	C16	C15	D20	D20	D20	C16	D20	D20
	A6	B11	A6	B11	B11	C16	C16	B11	B11	C16	C16	C16	C16	D21	C16	D21
d	0,088	0,078	0,064	0,062	0,072	0,084	0,086	0,065	0,053	0,072	0,077	0,075	0,082	0,061	0,107	0,528

Table B.6: Optimization results for $p = 7$

m	0,50	0,55	0,60	0,65	0,70	0,75	0,80	0,85	0,90	0,95	1,00	1,05	1,10	1,15	1,20	1,25
$\boldsymbol{\alpha}$	0,327	0,233	0,204	0,211	0,260	0,423	0,422	0,058	0,055	0,065	0,142	0,160	0,120	0,138	0,101	0,070
	0,774	0,301	0,275	0,314	0,665	0,671	0,670	0,388	0,318	0,338	0,370	0,380	0,460	0,448	0,142	0,088
	0,832	0,692	0,348	0,367	0,718	0,760	0,743	0,723	0,367	0,398	0,943	0,922	0,624	0,630	0,181	0,121
	0,926	0,883	1,151	0,773	1,087	1,082	1,061	0,761	0,633	0,440	1,014	0,987	0,686	0,674	0,377	0,149
	0,970	0,915	1,166	0,804	1,135	1,171	1,157	1,036	1,063	1,084	1,209	1,258	1,197	1,254	0,410	0,173
	1,444	1,442	1,489	1,123	1,206	1,240	1,202	1,484	1,476	1,259	1,309	1,333	1,275	1,280	0,451	0,232
	1,529	1,543	1,517	1,166	1,265	1,490	1,517	1,538	1,554	1,296	1,373	1,429	1,521	1,536	1,555	1,571
Structure	8	4	2	6	7	6	6	3	7	7	7	7	7	7	6	4
Vector	B10	B10	B10	B10	B10	B10	B10	B10	D19	D19	D19	D19	D19	D19	D19	D19
sequence	A6	A6	C15	C15	C15	C15	C15	C14	C14	C14	C15	C15	D20	D20	D20	D20
	B10	B10	B10	B10	B10	B10	B10	C15	C15	C15	D19	D19	C15	C15	D19	D19
	A6	B11	B11	B11	C15	C15	C15	B11	C16	D20	D20	D20	D20	D20	D20	D20
	B10	B10	B10	C15	B10	B11	B11	C15	C15	C15	C15	C15	C16	C16	D21	D19
	B11	A6	B11	B11	B11	C15	C15	C16	B11	C16	D20	D20	D20	D20	D20	D20
	A6	B11	A6	B10	C15	C16	C16	B11	C16	C15	C15	D21	D21	D21	D21	D21
	B11	A6	B11	B11	B11	B11	B11	C16	B11	C16	C16	C16	C16	C16	C16	C16
d	0,076	0,065	0,057	0,057	0,061	0,073	0,069	0,056	0,049	0,063	0,065	0,075	0,077	0,052	0,104	0,529

Table B.7: Optimization results for $p = 8$

m	0,50	0,55	0,60	0,65	0,70	0,75	0,80	0,85	0,90	0,95	1,00	1,05	1,10	1,15	1,20	1,25
$\boldsymbol{\alpha}$	0,229	0,225	0,169	0,194	0,659	0,261	0,400	0,060	0,309	0,270	0,129	0,165	0,153	0,138	0,099	0,068
	0,689	0,284	0,212	0,299	0,704	0,663	0,702	0,370	0,350	0,386	0,675	0,610	0,512	0,436	0,138	0,086
	0,741	0,704	0,280	0,365	0,780	0,731	0,758	0,414	0,404	0,753	0,960	0,648	0,565	0,647	0,179	0,118
	0,909	0,889	0,347	0,395	1,083	1,071	1,060	0,612	0,985	0,916	1,020	0,704	0,666	0,681	0,381	0,145
	0,965	0,919	0,391	0,818	1,125	1,141	1,155	0,727	1,049	0,956	1,187	0,922	0,937	1,254	0,415	0,166
	1,310	1,419	1,127	1,117	1,188	1,199	1,200	0,763	1,095	1,031	1,275	0,987	0,972	1,279	0,452	0,203
	1,449	1,492	1,137	1,158	1,239	1,289	1,471	1,036	1,501	1,367	1,324	1,261	1,268	1,506	1,540	0,214
	1,530	1,533	1,550	1,310	1,292	1,549	1,546	1,534	1,533	1,559	1,394	1,333	1,314	1,552	1,556	0,225
Structure	1	12	4	7	14	15	14	15	14	7	15	15	15	15	14	8
Vector	B10	B10	B10	B10	B10	B10	B10	B10	D19	D19	D19	D19	D19	D19	D19	D19
sequence	A6	A6	C15	C15	C15	C15	C15	C14	C14	C15	C15	C15	C15	D20	D20	D20
	B10	B10	B10	B10	B10	B10	B10	C15	D19	D19	D19	D19	D19	C15	D19	D19
	B11	B11	B11	B11	C15	C15	C15	B11	C15	C15	D20	D20	D20	D20	D20	D20
	A6	B10	B10	C15	B10	B10	B11	C15	C16	C16	C15	C15	C15	C16	D21	D19
	B10	A6	B11	B10	C15	B11	C15	C16	C15	D20	D20	D20	D20	D20	D20	D20
	A6	B11	B10	B11	B11	C15	C16	C15	C16	C15	C15	C16	C16	D21	D21	D19
	B11	A6	B11	B10	C15	B11	B11	B11	B11	C16	D20	D20	D20	C16	C16	D20
	A6	B11	A6	B11	B11	C16	C16	C16	C16	B11	C16	C16	D21	D21	D21	D21
d	0,069	0,059	0,047	0,049	0,059	0,062	0,061	0,053	0,044	0,057	0,060	0,058	0,060	0,049	0,103	0,528

Table B.8: Optimization results for $p = 9$

m	0,50	0,55	0,60	0,65	0,70	0,75	0,80	0,85	0,90	0,95	1,00	1,05	1,10	1,15	1,20	1,25
$\boldsymbol{\alpha}$	0,281	0,139	0,170	0,175	0,250	0,261	0,047	0,061	0,087	0,109	0,123	0,164	0,156	0,096	0,088	0,068
	0,328	0,255	0,212	0,356	0,627	0,670	0,660	0,354	0,306	0,331	0,373	0,437	0,456	0,129	0,113	0,086
	0,685	0,308	0,277	0,392	0,654	0,736	0,728	0,383	0,348	0,393	0,969	0,651	0,624	0,168	0,144	0,118
	0,801	0,692	0,338	0,757	0,721	1,071	0,776	0,635	0,403	0,438	1,023	0,705	0,685	0,446	0,176	0,145
	0,853	0,858	0,381	0,841	0,759	1,139	1,032	0,736	0,994	0,979	1,174	0,924	0,935	0,634	0,198	0,166
	0,944	1,203	1,129	1,111	1,084	1,197	1,162	0,768	1,045	1,036	1,247	0,988	0,971	0,679	0,375	0,202
	0,983	1,430	1,142	1,147	1,128	1,284	1,200	1,036	1,114	1,149	1,285	1,259	1,272	1,256	0,407	0,214
	1,470	1,498	1,496	1,274	1,193	1,501	1,485	1,494	1,498	1,272	1,346	1,330	1,317	1,280	0,450	0,225
	1,537	1,536	1,520	1,320	1,246	1,527	1,534	1,547	1,531	1,301	1,390	1,483	1,523	1,535	1,555	1,571
Structure	8	3	4	6	15	15	11	15	7	15	15	15	15	14	12	8
Vector	B10	B10	B10	B10	B10	B10	B10	B10	D19	D19	D19	D19	D19	D19	D19	D19
sequence	A6	B11	C15	C15	C15	C15	C14	C14	C15	C15	C15	C15	C15	D20	D20	D20
	B10	A6	B10	B10	B10	B10	C15	C15	D19	D19	D19	D19	D19	D19	D19	D19
	A6	B10	B11	B11	C15	C15	B10	B11	C14	C14	D20	D20	D20	D20	D20	D20
	B10	B11	B10	C15	B10	B10	C15	C15	C15	C15	C15	C15	C15	C15	D19	D19
	B11	B10	B11	B10	B11	B11	B11	C16	C16	D20	D20	D20	D20	D20	D20	D20
	B10	A6	B10	C15	C15	C15	C15	C15	C15	C15	C15	C16	C16	C16	D21	D19
	A6	B11	B11	B11	B11	B11	B11	B11	C16	C16	D20	D20	D20	D20	D20	D20
	B11	A6	A6	B10	C15	C16	C16	C16	B11	C15	C15	C15	D21	D21	D21	D21
	A6	B11	B11	B11	B11	B11	B11	B11	C16	C16	C16	C16	C16	C16	C16	C16
d	0,060	0,055	0,041	0,045	0,053	0,058	0,053	0,049	0,040	0,049	0,056	0,058	0,051	0,041	0,102	0,529

Table B.9: Optimization results for $p = 10$

m	0,50	0,55	0,60	0,65	0,70	0,75	0,80	0,85	0,90	0,95	1,00	1,05	1,10	1,15	1,20	1,25
$\boldsymbol{\alpha}$	0,269	0,198	0,160	0,210	0,223	0,230	0,048	0,049	0,085	0,112	0,138	0,141	0,156	0,099	0,087	0,068
	0,667	0,306	0,194	0,312	0,260	0,634	0,436	0,359	0,297	0,328	0,325	0,602	0,435	0,133	0,113	0,086
	0,704	0,361	0,256	0,375	0,627	0,674	0,633	0,408	0,330	0,379	0,364	0,638	0,652	0,171	0,144	0,120
	0,823	0,658	0,305	0,402	0,656	0,733	0,689	0,742	0,380	0,420	0,635	0,695	0,696	0,433	0,176	0,129
	0,866	0,792	0,347	0,794	0,726	0,793	0,751	1,045	0,432	0,975	0,954	0,957	0,937	0,654	0,197	0,131
	0,949	0,925	0,421	1,090	1,081	1,064	0,789	1,170	0,597	1,035	1,018	1,003	0,972	0,688	0,375	0,144
	0,985	0,945	0,609	1,113	1,125	1,123	1,032	1,186	0,998	1,154	1,196	1,210	1,270	1,256	0,407	0,166
	1,360	1,282	1,129	1,184	1,191	1,175	1,163	1,384	1,045	1,282	1,282	1,262	1,314	1,279	0,450	0,205
	1,467	1,471	1,141	1,211	1,243	1,247	1,199	1,489	1,111	1,314	1,331	1,314	1,488	1,504	1,558	0,220
	1,536	1,550	1,507	1,325	1,332	1,552	1,529	1,540	1,527	1,564	1,436	1,357	1,556	1,551	1,568	0,221
Structure	1	3	24	15	28	31	7	26	31	15	31	31	31	30	12	18
Vector sequence	B10	B10	B10	B10	B10	B10	B10	B10	D19	D19	D19	D19	D19	D19	D19	D19
	A6	A6	C15	C15	C15	C15	C14	C14	C15	C15	C15	C15	C15	D20	D20	D20
	B10	B10	B10	B10	B10	B10	C15	C15	D19	D19	D19	D19	D19	D19	D19	D19
	A6	B11	B11	C15	C15	C15	B10	B10	C14	C14	D20	D20	D20	D20	D20	D20
	B10	A6	B10	B10	B10	B10	C15	C15	C15	C15	C15	C15	C15	C15	D19	D21
	B11	B10	B11	B11	B11	B11	B11	B11	C16	D20	D20	D20	D20	D20	D20	D20
	A6	B11	B10	C15	B10	C15	C15	C16	C15	C15	C15	C15	C16	C16	D21	D19
	B10	B10	B11	B10	C15	B11	B11	C15	C16	C16	C16	D20	D20	D20	D20	D20
	A6	A6	B10	B11	B11	C15	C15	C16	C15	C15	C15	C16	D21	D21	D21	D19
	B11	B11	A6	B10	C15	B11	C16	B11	B11	C16	D20	D20	C16	C16	C16	D20
	A6	A6	B11	B11	B11	C16	B11	C16	C16	B11	C16	C16	D21	D21	B11	D21
d	0,054	0,047	0,037	0,041	0,046	0,050	0,049	0,045	0,037	0,044	0,048	0,046	0,048	0,037	0,102	0,528

APPENDIX C

Capacitor voltage balancing

The 5L-FC converter has nine flying capacitors. The voltage across each flying capacitor has to be controlled. A full degree of per-phase redundancy permits the voltage balancing algorithm to be considered independently for each phase and in a separate layer from the main controller.

Flying capacitor voltages of the phase $x \in \{a, b, c\}$ can be predicted based on the equations (2.11).

$$u_{Cx1}(k+1) = u_{Cx1}(k) + T_{\mathrm{s}} \cdot (s_{x3} - s_{x4}) \frac{i_x}{C_{\mathrm{FC}}}, \tag{C.1a}$$

$$u_{Cx2}(k+1) = u_{Cx2}(k) + T_{\mathrm{s}} \cdot (s_{x2} - s_{x3}) \frac{i_x}{C_{\mathrm{FC}}}, \tag{C.1b}$$

$$u_{Cx3}(k+1) = u_{Cx3}(k) + T_{\mathrm{s}} \cdot (s_{x1} - s_{x2}) \frac{i_x}{C_{\mathrm{FC}}}. \tag{C.1c}$$

The phase voltage level is defined by the main controller. Afterwards, capacitor voltages are precalculated for each redundant states of the predefined voltage level based on Table (2.5). For instance, the four states $\{0001\}$, $\{0010\}$, $\{0100\}$ and $\{1000\}$ that result in the voltage level -1 in the phase x are the redundant states of this voltage level.

The precalculated voltages of each phase are used to form an objective function:

$$J_{\mathrm{FC,x}} = (u_{Cx1}(k+1) - u^*_{Cx1})^2 + (u_{Cx2}(k+1) - u^*_{Cx2})^2 + (u_{Cx3}(k+1) - u^*_{Cx3})^2. \tag{C.2}$$

Finally the redundant state which minimizes the objective function is chosen to be applied for the phase x.

List of Figures

List of Tables

Bibliography

[1] D. G. Holmes and T. A. Lipo, *Pulse Width Modulation for Power Converters: Principles and Practice*. John Wiley and Sons, 2003.

[2] J. Holtz and X. Qi, "Optimal control of medium-voltage drives-an overview," *Industrial Electronics, IEEE Transactions on*, vol. 60, no. 12, pp. 5472–5481, Dec 2013.

[3] A. Edpuganti and A. Rathore, "A survey of low switching frequency modulation techniques for medium-voltage multilevel converters," *Industry Applications, IEEE Transactions on*, vol. 51, no. 5, pp. 4212–4228, Sept 2015.

[4] H. Abu-Rub, J. Holtz, J. Rodriguez, and G. Baoming, "Medium-voltage multilevel converters - state of the art, challenges, and requirements in industrial applications," *Industrial Electronics, IEEE Transactions on*, vol. 57, no. 8, pp. 2581–2596, Aug 2010.

[5] A. Nabae, I. Takahashi, and H. Akagi, "A new neutral-point-clamped pwm inverter," *Industry Applications, IEEE Transactions on*, vol. IA-17, no. 5, pp. 518–523, Sept 1981.

[6] J. Rodriguez, S. Bernet, B. Wu, J. Pontt, and S. Kouro, "Multilevel voltage-source-converter topologies for industrial medium-voltage drives," *Industrial Electronics, IEEE Transactions on*, vol. 54, no. 6, pp. 2930–2945, Dec 2007.

[7] P. Barbosa, P. Steimer, J. Steinke, L. Meysenc, M. Winkelnkemper, and N. Celanovic, "Active neutral-point-clamped multilevel converters," in *Power Electronics Specialists Conference, 2005. PESC '05. IEEE 36th*, June 2005, pp. 2296–2301.

[8] P. Hammond, "A new approach to enhance power quality for medium voltage ac drives," *Industry Applications, IEEE Transactions on*, vol. 33, no. 1, pp. 202–208, Jan 1997.

[9] J. Dickerson and G. Ottaway, "Transformerless power supply with line to load isolation," in *U.S. Patent 3596369*, Aug. 1971.

[10] T. Meynard and H. Foch, "Multi-level conversion: high voltage choppers and voltage-source inverters," in *Power Electronics Specialists Conference, 1992. PESC '92 Record., 23rd Annual IEEE*, Jun 1992, pp. 397–403 vol.1.

[11] X. Kou, K. Corzine, and Y. Familiant, "Full binary combination schema for floating voltage source multilevel inverters," *Power Electronics, IEEE Transactions on*, vol. 17, no. 6, pp. 891–897, Nov 2002.

[12] J. Huang and K. Corzine, "Extended operation of flying capacitor multilevel inverters," *Power Electronics, IEEE Transactions on*, vol. 21, no. 1, pp. 140–147, Jan 2006.

[13] A. Volke and M. Hornkamp, *IGBT modules technologies, driver and application*. Munich: Infineon Technologies AG., 2011.

[14] Infineon, "Technische information / technical information," *FF75R12YT3 datasheet*, 2013.

[15] F. Turnbull, "Selected harmonic reduction in static d-c - a-c inverters," *Communication and Electronics, IEEE Transactions on*, vol. 83, no. 73, pp. 374–378, July 1964.

[16] H. S. Patel and R. Hoft, "Generalized techniques of harmonic elimination and voltage control in thyristor inverters: Part i–harmonic elimination," *Industry Applications, IEEE Transactions on*, vol. IA-9, no. 3, pp. 310–317, May 1973.

[17] L. Li, D. Czarkowski, Y. Liu, and P. Pillay, "Multilevel selective harmonic elimination pwm technique in series-connected voltage inverters," *Industry Applications, IEEE Transactions on*, vol. 36, no. 1, pp. 160–170, Jan 2000.

[18] M. Dahidah, V. Agelidis, and M. Rao, "On abolishing symmetry requirements in the formulation of a five-level selective harmonic elimination pulse-width modulation technique," *Power Electronics, IEEE Transactions on*, vol. 21, no. 6, pp. 1833–1837, Nov 2006.

[19] M. Dahidah, G. Konstantinou, and V. Agelidis, "A review of multilevel selective harmonic elimination pwm: Formulations, solving algorithms, implementation and applications," *Power Electronics, IEEE Transactions on*, vol. 30, no. 8, pp. 4091–4106, Aug 2015.

[20] Z. Du, L. Tolbert, and J. Chiasson, "Active harmonic elimination for multilevel converters," *Power Electronics, IEEE Transactions on*, vol. 21, no. 2, pp. 459–469, March 2006.

[21] S. Pulikanti and V. Agelidis, "Control of neutral point and flying capacitor voltages in five-level she-pwm controlled anpc converter," in *Industrial Electronics and Applications, 2009. ICIEA 2009. 4th IEEE Conference on*, May 2009, pp. 172–177.

[22] M. Dahidah and V. Agelidis, "A hybrid genetic algorithm for selective harmonic elimination control of a multilevel inverter with non-equal dc sources," in *Power Electronics and Drives Systems, 2005. PEDS 2005. International Conference on*, vol. 2, 2005, pp. 1205–1210.

[23] H. Taghizadeh and M. Hagh, "Harmonic elimination of cascade multilevel inverters with nonequal dc sources using particle swarm optimization," *Industrial Electronics, IEEE Transactions on*, vol. 57, no. 11, pp. 3678–3684, Nov 2010.

[24] A. Kavousi, B. Vahidi, R. Salehi, M. Bakhshizadeh, N. Farokhnia, and S. Fathi, "Application of the bee algorithm for selective harmonic elimination strategy in multilevel inverters," *Power Electronics, IEEE Transactions on*, vol. 27, no. 4, pp. 1689–1696, April 2012.

[25] F. Filho, L. Tolbert, Y. Cao, and B. Ozpineci, "Real-time selective harmonic minimization for multilevel inverters connected to solar panels using artificial neural network angle generation," *Industry Applications, IEEE Transactions on*, vol. 47, no. 5, pp. 2117–2124, Sept 2011.

[26] S. Kouro, B. La Rocca, P. Cortes, S. Alepuz, B. Wu, and J. Rodriguez, "Predictive control based selective harmonic elimination with low switching frequency for multilevel converters," in *Energy Conversion Congress and Exposition, 2009. ECCE 2009. IEEE*, Sept 2009, pp. 3130–3136.

[27] F. C. Zach and H. Ertl, "Efficiency optimal control for ac drives with pwm inverters," *Industry Applications, IEEE Transactions on*, vol. IA-21, no. 4, pp. 987–1000, July 1985.

[28] J. Holtz and B. Beyer, "Optimal pulsewidth modulation for ac servos and low-cost industrial drives," *Industry Applications, IEEE Transactions on*, vol. 30, no. 4, pp. 1039–1047, Jul 1994.

[29] G. S. Buja and G. B. Indri, "Optimal pulsewidth modulation for feeding ac motors," *Industry Applications, IEEE Transactions on*, vol. IA-13, no. 1, pp. 38–44, Jan 1977.

[30] ——, "Optimal pulsewidth modulation for feeding ac motors," *Industry Applications, IEEE Transactions on*, vol. IA-13, no. 1, pp. 38–44, Jan 1977.

[31] N. Oikonomou, *Control of medium voltage drives at very low switching frequency*. Berlin: Logos Verlag, 2008.

[32] A. Rathore, J. Holtz, and T. Boller, "Synchronous optimal pulsewidth modulation for low-switching-frequency control of medium-voltage multilevel inverters," *Industrial Electronics, IEEE Transactions on*, vol. 57, no. 7, pp. 2374–2381, July 2010.

[33] J. Holtz and B. Beyer, "Fast current trajectory tracking control based on synchronous optimal pulsewidth modulation," *Industry Applications, IEEE Transactions on*, vol. 31, no. 5, pp. 1110–1120, Sep 1995.

[34] N. Oikonomou and J. Holtz, "Closed-loop control of medium-voltage drives operated with synchronous optimal pulsewidth modulation," *Industry Applications, IEEE Transactions on*, vol. 44, no. 1, pp. 115–123, Jan 2008.

[35] J. Holtz and N. Oikonomou, "Synchronous optimal pulsewidth modulation and stator flux trajectory control for medium-voltage drives," *Industry Applications, IEEE Transactions on*, vol. 43, no. 2, pp. 600–608, March 2007.

[36] T. Geyer, N. Oikonomou, G. Papafotiou, and F. Kieferndorf, "Model predictive pulse pattern control," *Industry Applications, IEEE Transactions on*, vol. 48, no. 2, pp. 663–676, March 2012.

[37] N. Oikonomou, C. Gutscher, P. Karamanakos, F. Kieferndorf, and T. Geyer, "Model predictive pulse pattern control for the five-level active neutral-point-clamped inverter," *Industry Applications, IEEE Transactions on*, vol. 49, no. 6, pp. 2583–2592, Nov 2013.

[38] T. Geyer and N. Oikonomou, "Model predictive pulse pattern control with very fast transient responses," in *Energy Conversion Congress and Exposition (ECCE), 2014 IEEE*, Sept 2014, pp. 5518–5524.

[39] D. Casadei, F. Profumo, G. Serra, and A. Tani, "Foc and dtc: two viable schemes for induction motors torque control," *Power Electronics, IEEE Transactions on*, vol. 17, no. 5, pp. 779–787, Sep 2002.

[40] M. Depenbrock, "Direct self-control (dsc) of inverter-fed induction machine," *Power Electronics, IEEE Transactions on*, vol. 3, no. 4, pp. 420–429, Oct 1988.

[41] J. Holtz, "Pulsewidth modulation for electronic power conversion," *Proceedings of the IEEE*, vol. 82, no. 8, pp. 1194–1214, Aug 1994.

[42] ——, "Pulsewidth modulation-a survey," *Industrial Electronics, IEEE Transactions on*, vol. 39, no. 5, pp. 410–420, 1992.

[43] H. S. Patel and R. Hoft, "Generalized Techniques of Harmonic Elimination and Voltage Control in Thyristor Inverters: Part I–Harmonic Elimination," *Industry Applications, IEEE Transactions on*, vol. 9, no. 3, pp. 310–317, 1973.

[44] ——, "Generalized Techniques of Harmonic Elimination and Voltage Control in Thyristor Inverters: Part II — Voltage Control Techniques," *Industry Applications, IEEE Transactions on*, vol. 10, no. 5, pp. 666–673, 1974.

[45] Z. Du, B. Ozpineci, L. Tolbert, and J. Chiasson, "Dc - ac cascaded h-bridge multilevel boost inverter with no inductors for electric/hybrid electric vehicle applications," *Industry Applications, IEEE Transactions on*, vol. 45, no. 3, pp. 963–970, May 2009.

[46] J. Pontt, J. Rodriguez, and R. Huerta, "Mitigation of noneliminated harmonics of shepwm three-level multipulse three-phase active front end converters with low switching frequency for meeting standard ieee-519-92," *Power Electronics, IEEE Transactions on*, vol. 19, no. 6, pp. 1594–1600, Nov 2004.

[47] A. Watson, P. Wheeler, and J. Clare, "A complete harmonic elimination approach to dc link voltage balancing for a cascaded multilevel rectifier," *Industrial Electronics, IEEE Transactions on*, vol. 54, no. 6, pp. 2946–2953, Dec 2007.

[48] B. Gultekin and M. Ermis, "Cascaded multilevel converter-based transmission statcom: System design methodology and development of a 12 kv -12 mvar power stage," *Power Electronics, IEEE Transactions on*, vol. 28, no. 11, pp. 4930–4950, Nov 2013.

[49] E. Ozdemir, S. Ozdemir, and L. Tolbert, "Fundamental-frequency-modulated six-level diode-clamped multilevel inverter for three-phase stand-alone photovoltaic system," *Industrial Electronics, IEEE Transactions on*, vol. 56, no. 11, pp. 4407–4415, Nov 2009.

[50] K. Ilves, A. Antonopoulos, S. Norrga, and H.-P. Nee, "A new modulation method for the modular multilevel converter allowing fundamental switching frequency," *Power Electronics, IEEE Transactions on*, vol. 27, no. 8, pp. 3482–3494, Aug 2012.

[51] K. Ilves, A. Antonopoulos, L. Harnefors, S. Norrga, and H.-P. Nee, "Circulating current control in modular multilevel converters with fundamental switching frequency," in *Power Electronics and Motion Control Conference (IPEMC), 2012 7th International*, vol. 1, June 2012, pp. 249–256.

[52] J. Holtz and B. Beyer, "Fast current trajectory tracking control based on synchronous optimal pulsewidth modulation," *Industry Applications, IEEE Transactions on*, vol. 31, no. 5, pp. 1110–1120, Sep 1995.

[53] G. Heinle, "The structure of optimized pulse patterns," in *Power Electronics and Applications, 1993., Fifth European Conference on*, 1993, pp. 378–383.

[54] J. Pontt, J. Rodriguez, A. Liendo, P. Newman, J. Holtz, and J. San Martin, "Network-friendly low-switching-frequency multipulse high-power three-level pwm rectifier," *Industrial Electronics, IEEE Transactions on*, vol. 56, no. 4, pp. 1254–1262, April 2009.

[55] P. Cortes, A. Wilson, S. Kouro, J. Rodriguez, and H. Abu-Rub, "Model predictive control of multilevel cascaded h-bridge inverters," *Industrial Electronics, IEEE Transactions on*, vol. 57, no. 8, pp. 2691–2699, Aug 2010.

[56] B. Riar, T. Geyer, and U. Madawala, "Model predictive direct current control of modular multilevel converters: Modeling, analysis, and experimental evaluation," *Power Electronics, IEEE Transactions on*, vol. 30, no. 1, pp. 431–439, Jan 2015.

[57] R. Vargas, P. Cortes, U. Ammann, J. Rodriguez, and J. Pontt, "Predictive control of a three-phase neutral-point-clamped inverter," *Industrial Electronics, IEEE Transactions on*, vol. 54, no. 5, pp. 2697–2705, Oct 2007.

[58] A. Khambadkone and J. Holtz, "Low switching frequency and high dynamic pulsewidth modulation based on field-orientation for high-power inverter drive," *Power Electronics, IEEE Transactions on*, vol. 7, no. 4, pp. 627–632, Oct 1992.

[59] T. Geyer, "Model predictive direct current control: Formulation of the stator current bounds and the concept of the switching horizon," *Industry Applications Magazine, IEEE*, vol. 18, no. 2, pp. 47–59, March 2012.

[60] T. Geyer and D. Quevedo, "Multistep direct model predictive control for power electronics - part 1: Algorithm," in *Energy Conversion Congress and Exposition (ECCE), 2013 IEEE*, Sept 2013, pp. 1154–1161.

[61] ——, "Multistep direct model predictive control for power electronics - part 2: Analysis," in *Energy Conversion Congress and Exposition (ECCE), 2013 IEEE*, Sept 2013, pp. 1162–1169.

[62] ——, "Performance of multistep finite control set model predictive control for power electronics," *Power Electronics, IEEE Transactions on*, vol. 30, no. 3, pp. 1633–1644, March 2015.

[63] G. Papafotiou, J. Kley, K. Papadopoulos, P. Bohren, and M. Morari, "Model predictive direct torque control - implementation and experimental evaluation," *Industrial Electronics, IEEE Transactions on*, vol. 56, no. 6, pp. 1906–1915, June 2009.

[64] T. Geyer and S. Mastellone, "Model predictive direct torque control of a five-level anpc converter drive system," *Industry Applications, IEEE Transactions on*, vol. 48, no. 5, pp. 1565–1575, Sept 2012.

[65] P. Zanchetta, D. Gerry, V. Monopoli, J. Clare, and P. Wheeler, "Predictive current control for multilevel active rectifiers with reduced switching frequency," *Industrial Electronics, IEEE Transactions on*, vol. 55, no. 1, pp. 163–172, Jan 2008.

[66] J. Scoltock, T. Geyer, and U. Madawala, "Model predictive direct power control for grid-connected npc converters," *Industrial Electronics, IEEE Transactions on*, vol. 62, no. 9, pp. 5319–5328, Sept 2015.

[67] V. Yaramasu, B. Wu, M. Rivera, and J. Rodriguez, "A new power conversion system for megawatt pmsg wind turbines using four-level converters and a simple control scheme based on two-step model predictive strategy - part i: Modeling and theoretical analysis," *Emerging and Selected Topics in Power Electronics, IEEE Journal of*, vol. 2, no. 1, pp. 3–13, March 2014.

[68] V. Yaramasu, B. Wu, and J. Chen, "Model-predictive control of grid-tied four-level diode-clamped inverters for high-power wind energy conversion systems," *Power Electronics, IEEE Transactions on*, vol. 29, no. 6, pp. 2861–2873, June 2014.

[69] V. Yaramasu and B. Wu, "Predictive control of a three-level boost converter and an npc inverter for high-power pmsg-based medium voltage wind energy conversion systems," *Power Electronics, IEEE Transactions on*, vol. 29, no. 10, pp. 5308–5322, Oct 2014.

[70] A. Calle-Prado, S. Alepuz, J. Bordonau, J. Nicolas-Apruzzese, P. Cortes, and J. Rodriguez, "Model predictive current control of grid-connected neutral-point-clamped converters to meet low-voltage ride-through requirements," *Industrial Electronics, IEEE Transactions on*, vol. 62, no. 3, pp. 1503–1514, March 2015.

[71] C. Townsend, T. Summers, J. Vodden, A. Watson, R. Betz, and J. Clare, "Optimization of switching losses and capacitor voltage ripple using model predictive control of a cascaded h-bridge multilevel statcom," *Power Electronics, IEEE Transactions on*, vol. 28, no. 7, pp. 3077–3087, July 2013.

[72] B. Wu, *High-Power Converters and AC Drives*. Wiley-IEEE Press, 2006.

[73] M. E. S. Graham C. Goodwin, Stefan F. Graebe, *Control System Design*. Prentice Hall, 2000.

[74] M. Morari and J. H. Lee, "Model predictive control: past, present and future," *Computers and Chemical Engineering*, vol. 23, no. 4–5, pp. 667 – 682, 1999.

[75] J. S. S. Holtz, "A predictive controller for the stator current vector of ac machines fed from a switched voltage source," *Industry Applications, IEEE Transactions on*, pp. 1665–1675, 1983.

[76] R. Kennel and D. Schröder, "Predictive control strategy for converters," in *Control in Power Electronics and Electrical Drives 1983*, ser. IFAC Symposia Series, R. ZWICKY, Ed. Oxford: Pergamon, 1983, pp. 415 – 422.

[77] A. Propoi, "Use of linear programming methods for synthesizing sampled-data automatic systems," in *Automation and Remote Control*, 1963, p. 837–844.

[78] J. L. T. J. Richalet, A. Rault and J. Papon, "Algorithmic control of industrial processes," in *Fourth IFAC symposium on identixcation and system parameter estimation*, vol. WP5-B, 1976, pp. 1119–1167.

[79] ——, "Model predictive heuristic control-application to industrial processes," in *Automatica*, vol. 14, 1978, p. 413–428.

[80] B. De Schutter and B. De Moor, "The extended linear complementarity problem and the modeling and analysis of hybrid systems," in *Hybrid Systems V*, ser. Lecture Notes in Computer Science, P. Antsaklis, M. Lemmon, W. Kohn, A. Nerode, and S. Sastry, Eds. Springer Berlin Heidelberg, 1999, vol. 1567, pp. 70–85.

[81] M. Morari and L. Thiele, Eds., *Hybrid systems: Computation and Control*, ser. LNCS, Proceedings of the 8th International Workshop, HSCC 2005. ETH Zurich, Switzerland: Springer Verlag, Mar. 2005, vol. 3414.

[82] R. K. P. S. A. Linder, R. Kanchan, Ed., *Model-Based Predictive Control of Electrical Drives*. Göttingen: Cuvillier Verlag, 2010.

[83] J. Rodriguez, J. Pontt, C. Silva, P. Cortes, U. Amman, and S. Rees, "Predictive current control of a voltage source inverter," in *Power Electronics Specialists Conference, 2004. PESC 04. 2004 IEEE 35th Annual*, vol. 3, June 2004, pp. 2192–2196 Vol.3.

[84] J. Nocedal and S. J. Wright, *Numerical Optimization*. Springer-Verlag, 2006.

[85] MathWorks, "Linear programming," *http://uk.mathworks.com/discovery/linear-programming.html*, 2015.

[86] ——, "Quadratic programming," *http://uk.mathworks.com/discovery/quadratic-programming.html*, 2015.

[87] V. D. A. Bemporad, M. Morari and E. N. Pistikopoulos, "The explicit linear quadratic regulator for constrained systems," in *Automatica*, vol. 38, 2002, pp. 3 –20.

[88] T. A. J. P. Tndel and A. Bemporad, "An algorithm for multi-parametric quadratic programming and explicit mfc solutions," in *Proc. IEEE Conf. Dec. Control*, 2001, pp. 1199 –1204.

[89] S. Boyd and L. Vandenberghe, *Convex Optimization*. Cambridge University Press, 2009.

[90] P. D.W.Clarke, C.Mohtadi, "Generalized predictive control - part i," in *Automatica*, vol. 23, 1987, p. 137–148.

[91] ——, "Generalized predictive control - part ii," in *Automatica*, vol. 23, 1987, p. 149–160.

[92] P. Cortes, S. Kouro, B. La Rocca, R. Vargas, J. Rodriguez, J. Leon, S. Vazquez, and L. Franquelo, "Guidelines for weighting factors design in model predictive control of power converters and drives," in *Industrial Technology, 2009. ICIT 2009. IEEE International Conference on*, Feb 2009, pp. 1–7.

[93] T. Geyer, G. Papafotiou, and M. Morari, "Model predictive direct torque control - concept, algorithm, and analysis," *Industrial Electronics, IEEE Transactions on*, vol. 56, no. 6, pp. 1894–1905, June 2009.

[94] J. C. Ramirez Martinez, R. Kennel, and T. Geyer, "Model predictive direct current control," in *Industrial Technology (ICIT), 2010 IEEE International Conference on*, March 2010, pp. 1808–1813.

[95] T. Geyer, "Model predictive direct current control: Formulation of the stator current bounds and the concept of the switching horizon," *Industry Applications Magazine, IEEE*, vol. 18, no. 2, pp. 47–59, March 2012.

[96] J. Scoltock, T. Geyer, and U. Madawala, "Model predictive direct power control for a grid-connected converter with an lcl-filter," in *Industrial Technology (ICIT), 2013 IEEE International Conference on*, Feb 2013, pp. 588–593.

[97] F. Kieferndorf, P. Karamanakos, P. Bader, N. Oikonomou, and T. Geyer, "Model predictive control of the internal voltages of a five-level active neutral point clamped converter," in *Energy Conversion Congress and Exposition (ECCE), 2012 IEEE*, Sept 2012, pp. 1676–1683.

[98] P. Stolze, M. Tomlinson, R. Kennel, and T. Mouton, "Heuristic finite-set model predictive current control for induction machines," in *ECCE Asia Downunder (ECCE Asia), 2013 IEEE*, June 2013, pp. 1221–1226.

[99] J. Holtz, "Pulsewidth modulation for electronic power conversion," *Proceedings of the IEEE*, vol. 82, no. 8, pp. 1194–1214, Aug 1994.

[100] ——, "Advanced pulsewidth modulation and predictive control - an overview," *Industrial Electronics, IEEE Transactions on*, vol. PP, no. 99, pp. 1–1, 2015.

[101] T. Geyer, "A comparison of control and modulation schemes for medium-voltage drives: Emerging predictive control concepts versus pwm-based schemes," *Industry Applications, IEEE Transactions on*, vol. 47, no. 3, pp. 1380–1389, May 2011.

[102] T. Boller, J. Holtz, and A. Rathore, "Neutral-point potential balancing using synchronous optimal pulsewidth modulation of multilevel inverters in medium-voltage high-power ac drives," *Industry Applications, IEEE Transactions on*, vol. 50, no. 1, pp. 549–557, Jan 2014.

[103] Y. Wang and S. Boyd, "Fast model predictive control using online optimization," *Control Systems Technology, IEEE Transactions on*, vol. 18, no. 2, pp. 267–278, March 2010.